ABSTRACT

Title of Dissertation: EXPERIMENTS AND ANALYSIS OF HYBRID-ELECTRIC POWER FOR MULTI-ROTOR UNMANNED AIR VEHICLES

Matthew Arace
Doctor of Philosophy, 2026

Dissertation Directed by: Professor Anubhav Datta
Department of Aerospace Engineering

This research developed a fundamental understanding of a hybrid-electric powerplant for an unmanned rotorcraft powered by proprotors through model testing and comprehensive analysis. The key questions answered were by how much should the rotor tip speed be reduced in forward flight and by what mechanism? The correct answers were shown to be crucial to establish the payload, range, and gross weight of such aircraft. These answers could not be found without detailed engine-generator fuel consumption data, and without its inclusion in a detailed comprehensive analysis of such aircraft. This dissertation filled these gaps — in a small scale within the resources available.

A 3.43 kW 4-stroke piston engine was coupled to a generator and rectifier to acquire basic data on power generation and engine specific fuel consumption. The isolated engine, generator, and coupled engine-generator efficiencies were characterized. A powertrain efficiency model was synthesized and validated, and partly calibrated, from the data. The model predicted engine specific fuel consumption as a function of engine torque and speed in a non-dimensional form. Thus, the model was rubberized for quantifying variations in engine efficiency with operating torque and speed in a scale-invariant manner. The model captures sensitivities to the engine operating conditions.

An in-house comprehensive analysis University of Maryland Advanced Rotorcraft Code II, UMARC-II, was significantly expanded to support the analysis of unique design elements of hybrid-electric aircraft. These refinements were validated with data from several wind tunnel test campaigns of the full-scale 26-ft diameter Boeing proprotor (M222), and the model-scale 4.75-ft diameter Maryland Tiltrotor Rig (MTR). UMARC-II was then used to understand rotor-wing dynamic and aerodynamic interactions, and was used to predict the power, L/D, and rotor torque and speed of a 50 lb quadrotor biplane. It was found that for a rotor mounted on a fixed wing generating lift, the oscillatory blade bending moments and the mean hub moments were amplified compared to an isolated rotor. The increase was proportional to how much lift the wing generated. Additionally, the wing aerodynamics were found to interact with the rotor aerodynamics in a way that accelerated the onset of stall at low speed for the quad biplane.

These quantities were coupled to the engine model through a rotorcraft sizing code. A rotorcraft sizing code was developed expressly to design electric and hybrid-electric VTOL. The aircraft was sized and a sensitivity analysis conducted to quantify the impact of engine specific fuel consumption assumptions. Once verified it was used to find the answer to the key question: by how much should the rotor tip speed be reduced? Next, several methods of engine speed control to meet the rotor operating torque and speed combinations were explored, compared to one another in complexity and value, and the best mechanism to reduce the rotor tip speed proposed. Thus, the key questions were answered.

The principal conclusions follow. For correct prediction of the optimal rotor tip speed reduction in cruise — a key attribute and benefit of distributed propulsion — a detailed engine specific fuel consumption model that captures the variation in speed and torque separately is required. Whereas aerodynamics alone suggest an optimal tip speed reduction to 40% of hover, the correction reduction to minimize gross weight is much higher around 60%-70% of hover. Reduction in rotor tip speed

should not be carried out by the electric motors alone. The engine should be controlled independently to minimize the fuel consumed at the desired power output. Based on the resulting bus voltage, the motors then control the rotors to achieve the desired tip speed reduction. Complexity is added to the control scheme, but significant operational gains are attained.

EXPERIMENTS AND ANALYSIS OF HYBRID-ELECTRIC POWER FOR MULTI-ROTOR UNMANNED AIR VEHICLES

by

Matthew Arace

Dissertation submitted to the Faculty of the Graduate School of the
University of Maryland, College Park in partial fulfillment
of the requirements for the degree of
Doctor of Philosophy
2026

Advisory Committee:
Professor Anubhav Datta, Chair/Advisor
Professor Inderjit Chopra
Professor James Baeder
Professor Huan Xu
Professor Chloe Johnson
Professor Maria Cameron

© Copyright by
Matthew Arace
2026

Dedicated to my family and loved ones,

without whom this would not be possible.

Acknowledgments

This work was only made possible by the Army/Navy/NASA Vertical Lift Research Center of Excellence (VLRCOE) program. I am grateful for the guidance and funding to pursue my passion and higher education. I would like to give a special thanks to Dr. Mahendra Bhagwat, Dr. Michael Vegh, and Mr. David Friedmann for their guidance over the years and for providing such a positive atmosphere to learn and grow.

My advisor, Dr. Anubhav Datta, deserves his own paragraph here. The wisdom and knowledge he has shared with me is beyond comprehension. He started simply as my academic advisor, overseeing my research and scribbling red ink all over my homework. He quickly became my mentor, someone I could rely on in personal and academic life, and eventually, my friend. Had he not taken me under his wing, I'm not sure I would have ever realized my potential. I believe he genuinely cares for all of his students as if they are his own children; a truly rare and admirable trait among advisors these days. I am deeply grateful for his unwavering support, and I will die happy if I can become even half the man he is one day.

My mother Kathleen deserves all of the acknowledgement in the world and then some. She sacrificed so much to raise me and my brothers all on her own since my father passed in 2004. Without her constant love and support, I would not be the man I am today. She has taught me to be good, just, selfless, and curious, and words alone cannot thank her enough. Thank you to her, my brothers, Rob and Anthony, my sisters in law, Erika and Martha, and my nieces, Blake, Blaire, Vallie, and Natalie for filling my life with so much joy and sharing in my grief over these years.

My partner Kelsey has been my rock. She has been my biggest advocate for balance and patiently listened to me yap about things that likely made no sense. Still, she nodded and asked questions, doing her best to follow my chaotic train of thought, and I even realized some major breakthroughs by

simply trying to explain things to her in a way that made sense. She was always understanding with how demanding this endeavor was, and always found ways for us to maintain a healthy lifestyle. We cooked, lifted weights, hiked, camped, backpacked, snowboarded, and more, and after each of our excursions I felt more focused and disciplined than ever. With her came my dog Milo, who has been my best friend every single day. While Kelsey was at work, he was sitting right next to my chair or right behind me snoring while I was clicking away. I love these two dearly, even if they fall asleep as I am teaching them structural dynamics, and plan to give back to them as much as they have given me.

I would like to acknowledge all of my friends and colleagues who have shared in my successes, listened to my complaints, and supported me in sorrow. They have all inspired me in some way over the years, whether it is helping me zoom out from my hole to see the bigger picture again, or simply listening while I got something off my chest. I had a difficult time transitioning to graduate school after working as a Systems Engineer for several years. I was worried my hands-on engineering knowledge had faded. My first two years of experimentation on my own were difficult, but Brent, Emily, and Brandyn helped me get back to my roots, which lead to the test rig and results in this dissertation. Eric, Akinola, Nathan, and Xavier were there from the start, and I am thankful we all got to learn and grow together. A special thank you to another mentor of mine, Seyhan Gul, who introduced me to comprehensive analysis and taught me nearly everything I know, which lead to most of the analytical work in this dissertation. He was also my mentor during my internship with the Army at NASA Ames in 2024, a formative experience for me. Thank you to my friends and colleagues Batin, Michael, Paulo, John, Ravi, Mrinal, Shashank, Abhishek, James, Fred, Lex, Logan, Vivek, Sridatta, Visesh, Kumardip, Radu, Howard, Yuval, Willi, Remi, Jacob, my professors, and everyone else at the Alfred Gessow Rotorcraft Center. Finally, thank you to my friends and family August, Dave, Janette, Brianna, Skylar, Mark, Brian, Justin, Derek, Sam, Malcolm, and the entire Deighan and Ruggia clans.

Table of Contents

Dedication ii

Acknowledgements iii

Table of Contents v

List of Tables vii

List of Figures viii

Chapter 1: Introduction 1
- 1.1 Distributed Propulsion . . . 1
- 1.2 Why Hybrid-Electric? . . . 7
- 1.3 Motivation . . . 8
- 1.4 Definition of hybrid-electric power . . . 12
- 1.5 Technical Approach . . . 13
- 1.6 Outline of dissertation . . . 13

Chapter 2: Experiments on Hybrid-Electric Power Generation 15
- 2.1 Test Setup . . . 15
- 2.2 Components of the powertrain . . . 16
- 2.3 Instrumentation . . . 19
- 2.4 Test Procedure . . . 20
- 2.5 Experimental Results . . . 22
- 2.6 Summary and Conclusions . . . 33

Chapter 3: Modeling of Hybrid-Electric Power Generation 36
- 3.1 Mathematical Model . . . 36
- 3.2 Linear Model . . . 40
- 3.3 Nonlinear Model . . . 40
- 3.4 Nonlinear Model with Pumping . . . 42
- 3.5 Summary and Conclusions . . . 52

Chapter 4: Rotorcraft Comprehensive Analysis 53
- 4.1 Simple Rigid Blade Analysis . . . 53
- 4.2 Comprehensive Analysis . . . 59
  - 4.2.1 Structural Model . . . 60
  - 4.2.2 Aerodynamic Model . . . 61
  - 4.2.3 Trim Solution . . . 62
- 4.3 Validation . . . 65
  - 4.3.1 Hover Power . . . 66
  - 4.3.2 Cruise Power . . . 71

4.3.3 Structural Loads . . . 74
4.4 Rotors on wings . . . 83
4.5 Multiple rotors and multiple wings . . . 94
4.6 Chapter summary and conclusions . . . 101

Chapter 5: Integrated power-platform 103
5.1 Rotorcraft sizing . . . 103
5.2 Breakdown of Sizing Framework . . . 105
5.3 Validation with XV-15 Weights . . . 108
5.4 Verification of Electric Weights . . . 110
5.5 Sizing a Hybrid-Electric Quad-Biplane . . . 112
5.6 Modes of RPM Reduction . . . 118
5.7 Chapter Summary and Conclusions . . . 123

Chapter 6: Summary and Conclusions 126
6.1 Conclusions . . . 127
6.2 Contributions of Presented Research . . . 130
6.3 Future Work . . . 132

Bibliography 152

List of Tables

2.1 Experimental data collected from piston-electric test rig with simulated load. 23

3.1 Calibrated model constants of scalable engine SFC model. 45

4.1 First five frequencies of the M222 wing in /rev. Rotor 551 RPM. 83

5.1 Group structures in rotorcraft sizing analysis. 105
5.2 Group weight calculations in rotorcraft sizing analysis. Formulae given in Appendix A. 108
5.3 Percent comparison of predicted weight groups relative to actual weight groups of the XV-15. 109
5.4 Fixed aircraft parameters of the quadrotor biplane sizing study. 113
5.5 Summary of engine operating modes to reduce rotor tip speed in cruise. 123

1 Rotor parameters 134
2 Empennage parameters 135
3 Fuselage parameters 135
4 Boom parameters 136
5 Alighting parameters 137
6 Mission fuel parameters 137
7 Drive system parameters 138
8 Engine parameters 139
9 Generator/Electric motor parameters 140
10 Inverter parameters 140
11 Battery parameters 140
12 Fixed wing parameters 141
13 Tiltrotor/Tiltwing wing parameters - primary 143
14 Tiltrotor/Tiltwing wing parameters - intermediate calculations 146
15 Nacelle & air induction parameters 147
16 Flight controls parameters 149
17 Hydraulics parameters 150
18 Anti-icing parameters 150
19 Fuel system parameters 151

List of Figures

1.1 Curtiss-Wright X-19 experimental tiltrotor with four rotors. . . . 2
1.2 Bell X-22 experimental tiltrotor with four ducted fans. . . . 2
1.3 Ling-Temco-Vought XC-142A experimental tilt-wing with four rotors. . . . 3
1.4 Drivetrain schematic of the XV-15. . . . 4
1.5 Simple schematic of an all-electric transmission. . . . 5
1.6 Energy density of tested Li-ion and Li-S cells relative to combustion based fuels. . . . 6
1.7 A collage of eVTOL concepts ranging from personal air vehicles to passenger transport. 7
1.8 Workhorse Surefly two-seat hybrid-electric demonstrator. . . . 9
1.9 Conceptual 50 lb QBiT designed in 2020. . . . 9
1.10 Piston-electric research rig with a 2-stroke engine at UMD and tested at Army Research Laboratory, Aberdeen during 2019-2022. . . . 10
1.11 Hybrid-electric multi-rotor UAV demonstrator developed by LaunchPoint EPS. . . . 10
1.12 Timeline of comprehensive analyses developed over the last 60 years.. . . . 12
1.13 Block diagram of a distributed hybrid-electric powerplant with four rotors. G: Generator, M: Motor, R: Rotor. . . . 13

2.1 The 4-stroke piston-electric test rig. . . . 16
2.2 Block diagram of hardware and instrumentation. I: current, V: voltage, Ω: engine speed, Q: engine torque, $\dot{m}_f$: fuel mass flow from tank . . . 17
2.3 Front of the test stand to break-in the engine. . . . 18
2.4 Rear of the test stand to break-in the engine. . . . 18
2.5 Test points collected. . . . 22
2.6 Engine SFC (kg/kW-hr) raw data contour . . . 24
2.7 Engine fuel mass flow rate versus RPM at 2.0 N-m torque . . . 25
2.8 Engine fuel mass flow rate versus Torque at 3500 RPM. . . . 26
2.9 Measured engine SFC curve fit data contour in kg/kW-hr. . . . 26
2.10 Measured engine SFC curve fit extrapolated data contour in kg/kW-hr. . . . 27
2.11 Engine SFC versus engine power with constant RPM lines (solid) and constant torque lines (dashed). . . . 27
2.12 Generator efficiency curve fit extrapolated data contour. . . . 28
2.13 Generator efficiency contour versus voltage and current . . . 30
2.14 Generator efficiency contour versus RPM and torque . . . 30
2.15 Generator efficiency versus power. Constant voltage lines. . . . 31
2.16 Generator efficiency versus power. Constant RPM lines. . . . 32
2.17 SFC/η_G versus RPM and torque . . . 33
2.18 SFC/η_G versus voltage and current . . . 34

3.1 Incorrect model. Constant thermal efficiency. Pumping power neglected. Data (lines) versus prediction (dashed). . . . 41
3.2 Refined model 1. Nonlinear thermal efficiency. Pumping power neglected. Data (lines) versus predictions (dashed). . . . 42

3.3 Refined model 2. Nonlinear thermal efficiency. Pumping Power included. Data (lines) versus predictions (dashed). . . . 43
3.4 Final model. Contour of fuel mass flow rate. Agreement between predictions (dashed) and experiment (solid). . . . 46
3.5 Final model. Contour of specific fuel consumption (SFC). Agreement between predictions (dashed) and experiment (solid). . . . 47
3.6 Final model. Contour of brake thermal efficiency η_B. Agreement between predictions (dashed) and experiment (solid). . . . 48
3.7 Final model. Engine SFC versus engine power. . . . 49
3.8 Contour of predicted indicated thermal efficiency η_T. . . . 50
3.9 Contour of predicted mechanical efficiency η_M. . . . 51

4.1 Prediction of L/D for the XV-15 (lines) versus measured (markers). . . . 56
4.2 Prediction of XV-15 trim pitch attitude (lines) versus measured (markers) at 91% NR. Positive nose-up. . . . 56
4.3 Impact of RPM reduction in axial flight on airfoil section c_l/c_d. . . . 57
4.4 Predicted lift-to-drag ratio of QBiT relative to the XV-15. . . . 58
4.5 Baseline: a single rotor with one free wake tip trailer per blade . . . 62
4.6 Refinement 1: One rotor with nearwake trailers, one tip trailer per blade, and one wing with one tip trailer. . . . 63
4.7 Refinement 2: Two rotors with nearwake trailers and one tip trailer per blade, and two wings with one tip trailer each. . . . 63
4.8 Refinement 3 (final): Four rotors with nearwake trailers, a tip trailer and root trailer per blade, and four wings with nearwake trailers and one tip trailer each. . . . 64
4.9 The MTR in the Glenn L. Martin wind tunnel. . . . 66
4.10 Wake geometry in hover with a tip trailer and root trailer. Wind tunnel test flight condition with tunnel recirculation. . . . 68
4.11 Wake geometry in pure hover with a tip trailer and root trailer. . . . 68
4.12 Measured thrust (markers) compared with UMARC-II predictions (lines). . . . 69
4.13 Measured power (markers) compared with UMARC-II predictions (lines). . . . 70
4.14 Two load cell measurements - thrust and power. Measured (markers) compared with UMARC-II predictions (lines). . . . 70
4.15 Measured (markers) compared with UMARC-II predictions (lines). . . . 71
4.16 M222 measured thrust coefficient (markers) compared with UMARC-II predictions (lines) versus non-dimensional tunnel speed λ_c. . . . 73
4.17 M222 measured power coefficient (markers) compared with UMARC-II predictions (lines) versus non-dimensional tunnel speed λ_c. . . . 73
4.18 Fanplot of the M222 rotor. Measured (markers) compared with UMARC-II predictions (lines). . . . 75
4.19 M222 half peak-to-peak flap bending moment in low speed flight (45 knots). Measured (markers) compared with UMARC-II predictions (lines). . . . 77
4.20 M222 half peak-to-peak chord bending moment in low speed flight (45 knots). Measured (markers) compared with UMARC-II predictions (lines). . . . 78
4.21 M222 mean hub moments in low speed flight (45 knots). Measured (markers) compared with UMARC-II predictions (lines). . . . 79

4.22 M222 non-dimensionalized mean hub moments in low speed flight (45 knots). Measured (markers) compared with UMARC-II predictions (lines). 80
4.23 M222 half peak-to-peak flap bending moment in high speed flight (105 knots). Measured (markers) compared with UMARC-II predictions (lines). 81
4.24 M222 half peak-to-peak chord bending moment in high speed flight (105 knots). Measured (markers) compared with UMARC-II predictions (lines). 81
4.25 M222 mean hub moments in high speed flight (105 knots). Measured (markers) compared with UMARC-II predictions (lines). 82
4.26 M222 non-dimensionalized mean hub moments in high speed flight (105 knots). Measured (markers) compared with UMARC-II predictions (lines). 82
4.27 Finite element model of a single rotor mounted on a wing tip. 84
4.28 M222 half peak-to-peak flap bending moment in high speed flight (105 knots). No wing (solid), wing at $\alpha = 4^\circ$ (dashed), wing at $\alpha = 12^\circ$ (dot-dashed). 85
4.29 M222 half peak-to-peak flap bending moment in high speed flight (105 knots). Wing at $\alpha = 12^\circ$ (dot-dashed). 86
4.30 M222 half peak-to-peak chord bending moment in high speed flight (105 knots). No wing (solid), wing at $\alpha = 4^\circ$ (dashed), wing at $\alpha = 12^\circ$ (dot-dashed). 87
4.31 M222 mean hub moments in high speed flight (105 knots). No wing (solid), wing at $\alpha = 4^\circ$ (dashed), wing at $\alpha = 12^\circ$ (dot-dashed). 87
4.32 Finite element model of the M222 rotor on a horizontal boom, like a wing. 88
4.33 Finite element model of the M222 rotor on a vertical boom, protruding into the airflow. 89
4.34 M222 half peak-to-peak flap bending moment in high speed flight (105 knots). No wing (solid), horizontal boom (dashed), vertical boom (dot-dashed). 89
4.35 M222 half peak-to-peak chord bending moment in high speed flight (105 knots). No wing (solid), horizontal boom (dashed), vertical boom (dot-dashed). 90
4.36 M222 mean hub moments in high speed flight (105 knots). No wing (solid), horizontal boom (dashed), vertical boom (dot-dashed). 91
4.37 Finite element model of the M222 rotor and wing. Wing on retreating side of the rotor. 92
4.38 Rotary-wing normal force coefficient at 90% R versus azimuth. No wing (solid), wing at $\alpha = 4^\circ$ (dashed), wing at $\alpha = 12^\circ$ (dot-dashed). 93
4.39 Blade tip deflection divided by radius versus azimuth. No wing (solid), wing at $\alpha = 4^\circ$ (dashed), wing at $\alpha = 12^\circ$ (dot-dashed). 93
4.40 Rotor direction of rotation for quad biplane. 94
4.41 Visualization of rotor tip vortex contact with wings. Counter-clockwise rotor bottom, clockwise rotor top. 96
4.42 Hooper plot of wing angle of attack. Peaks from blade tip vortex passage. 97
4.43 Diagram of rotor and wing bound circulation interaction. 98
4.44 Wing angle of attack at 48.9% span. No wing (solid), wing at $\alpha = 4^\circ$ (dashed), wing at $\alpha = 12^\circ$ (dot-dashed). 99
4.45 L/D prediction of quadrotor biplane aircraft. UMARC-II 1 rotor-wing CCW, 2 rotor-wing CCW+CW. 100

5.1 Flowchart of sizing methodology. 104
5.2 Engine weight model. 107
5.3 Electric motor weight model. 107

5.4 Inverter weight model. 108
5.5 Gross weight prediction of NASA electric quadrotor. 111
5.6 Hover power prediction of NASA electric quadrotor. 111
5.7 Sizing Mission; payload 5 lb, range falls out. 112
5.8 Quad biplane L/D versus tip speed reduction in cruise. 114
5.9 Engine SFC contour with constant power lines marked. 114
5.10 Cruise RPM = 100% NR. 115
5.11 Cruise RPM = 40% NR. 116
5.12 Gross weight versus tip speed reduction. 117
5.13 Weight versus range using best tip speed reduction. 118
5.14 Simple schematic of power flow; G = generator, M = Motor, R = Rotor. 119
5.15 H: Hover; Case 1, 2, and 3, cruise conditions. 120
5.16 Impact of tip speed reduction on take-off weight. 121
5.17 Sized vehicle take-off weight for different powertrain operating modes. 122

Chapter 1: Introduction

This chapter introduces the topic of this dissertation. It provides an overview of the motivation behind this research, a description of the problem, and a survey of past work to bring the reader up to the state of the art.

1.1 Distributed Propulsion

There is ever increasing interest in distributed propulsion for multi-rotor aircraft, specifically Vertical and/or Short Takeoff and Landing (V/STOL) aircraft. Distributed propulsion means multiple rotors provide lift and/or thrust collectively at various locations distributed over an aircraft. It is a separate configuration paradigm from a single main rotor (SMR), coaxial, tandem or side-by-side, tilt-wing or tilt-rotor, or even compound. The perceived benefits of this type of power architecture are primarily in agility and maneuverability by harnessing electric power and the high bandwidth rotor speed variation it enables. Power via multiple rotors also eliminates the need for a swashplate, reducing weight, drag, and complexity of each hub. There is an overall increase in aircraft weight and complexity, but the presence of multiple rotors enables unprecedented agility and handling, especially in gusty conditions, and opens the door toward full autonomy. Additionally, distribution of thrust may provide inherent redundancy to withstand single points of failure — a useful attribute especially for electric motors that are still orders of magnitude away from the reliability of mechanical transmission..

Large scale multi-rotor concepts have been prototyped in the past, primarily in the 1960s, but this was pre-electric era, and all suffered from severe issues stemming from both weight, such as the X-19 [1] shown in Fig. 1.1 and the X-22 [2] shown in Fig. 1.2, and complexities that arose from the complications of the mechanical transmission, such as the XC-142A [3] shown in Fig. 1.3. None of these aircraft were carried through to production. All of them crashed.

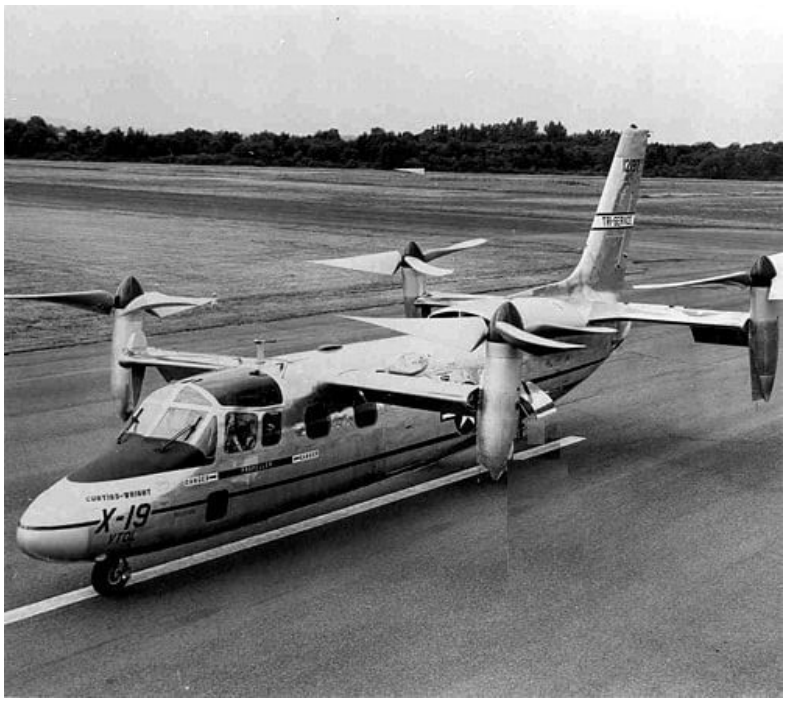


Figure 1.1: Curtiss-Wright X-19 experimental tiltrotor with four rotors.



Figure 1.2: Bell X-22 experimental tiltrotor with four ducted fans.



Figure 1.3: Ling-Temco-Vought XC-142A experimental tilt-wing with four rotors.

Typically, larger scale aircraft have multiple engines to provide redundancy in the power supply, requiring combining transmissions/coupling gearboxes to drive one rotor. As more rotors are added, naturally, the complexity of the drivetrain increases. Consider just the XV-15 drivetrain schematic in Fig. 1.4 from Ref. [4]. This aircraft has only two engines and two rotors, not four, one in each pylon at the wing tips. In addition to the gearboxes required to drive the individual rotors directly from the engines, cross shafting is needed to connect the rotors mechanically to each other, along with a center gearbox, to ensure rotor synchronization and redundancy to sustain the loss of one engine. One can imagine, as more rotors are added, additional cross shafting and gearboxes are required to mechanically link the rotors to each other and to the main drivetrain. As a result, the weight of the drivetrain balloons. Not only that, but the transient dynamics of the drivetrain itself become increasingly complex. The Curtiss-Wright X-19, shown earlier, had eight gearboxes that routed power from two Lycoming engines to the four rotors. It suffered a catastrophic gearbox failure during flight testing in 1965 that destroyed the prototype and subsequently ended the program.

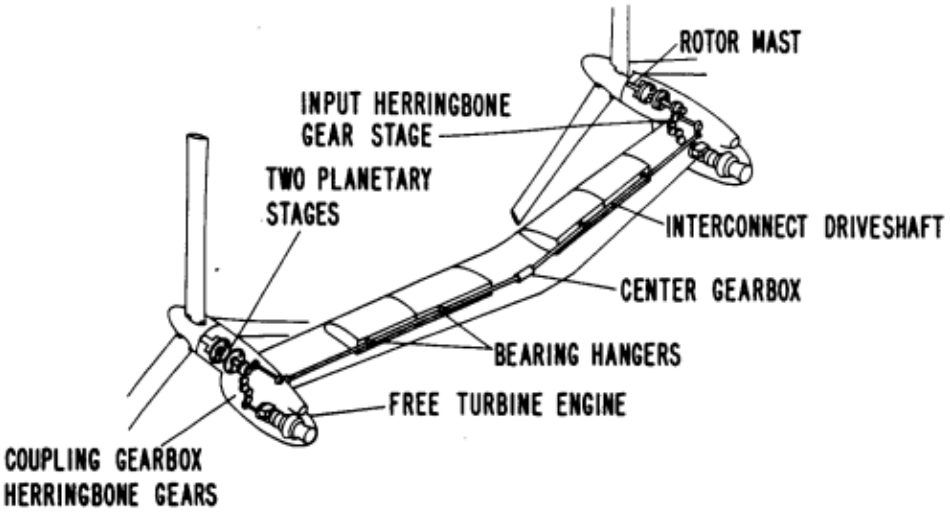


Figure 1.4: Drivetrain schematic of the XV-15.

Then came the advent of microelectronics. The exponential reduction in size has resulted in batteries, electric motors, inverters, and more that could enable power distribution through an electric transmission rather than mechanical. Consider a schematic of an all-electric transmission in Fig. 1.5. Batteries supply power as direct current (DC). Multiple loads can draw DC power from the same source. Multiple energy sources are retained for redundancy, connected by a DC bus. The controllers draw DC power, transmitted via wiring rather than shafting, based on their needs to drive their rotors individually. Thus, for configurations with multiple rotors/propulsors/thrusters, the mechanism to deliver power from source to load is greatly simplifed, at least in principle, notwithstanding the challenges of reliability.

Significant investments have been made in the last 20 years to design distributed electric propulsion (DEP) vehicles. Distributed electric propulsion started at small-scale due to advances in batteries and rapid prototyping that allowed electric motors, and power electronics enthusiasts to concoct hobby grade concepts [5]. But scaling these configurations up is a different matter altogether. Imagining manned aircraft is an even more serious and solemn task, by orders of magnitude, that requires more

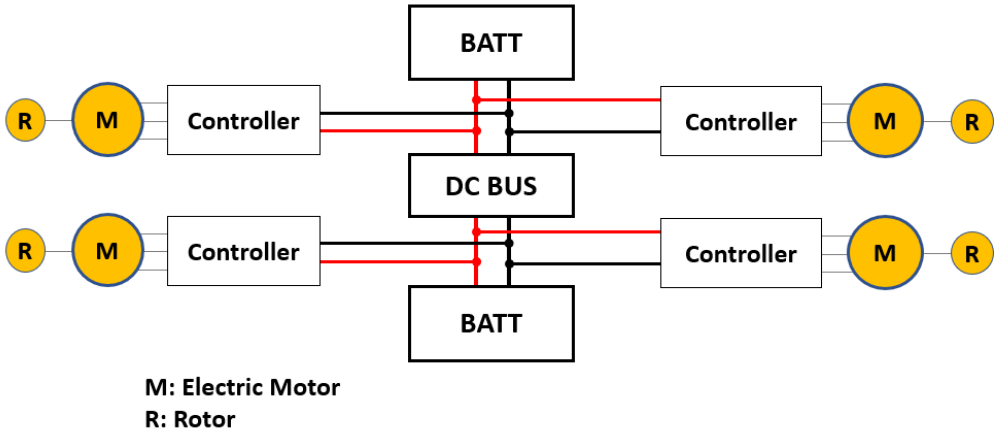


Figure 1.5: Simple schematic of an all-electric transmission.

than a clever concoction of electrical parts.

In DEP aircraft, the loads are rotors, fans, or propellers driven by individual electric motors. These motors are typically alternating current (AC) permanent-magnet synchronous (PMS), commonly brushless DC (BLDC) machines driven by inverters/motor controllers. The inverters draw DC power from the energy source and convert to AC to drive the motors. BLDC motors themselves have been designed to have high specific power and scale in weight with torque. Batteries, on the other hand, continue to have abysmal specific energy, and are the principal barrier to meaningful mission capability. The specific energy of batteries compared to hydrocarbon fuel is shown in the Ragone plot in Fig. 1.6. The battery data points are from actual cell fabrication and testing at the University of Maryland [6, 7] using advanced Nickel Cobalt Aluminum Oxide (NCA) and Lithum Sulfur (Li-S) chemistries. A nominal data point for hydrocarbon fuel is added from the following calculation. Consider gasoline; typical energy density is 12 kW-hr/kg $\times$ a conservative thermal efficiency of 0.2, resulting in a useful energy density of 2,400 W-hr/kg. Typical power density of an aviation grade engine is 5,000 W/kg. The specific energy of batteries is an order of magnitude lower than gasoline and diesel based fuels. VTOL aircraft require very high power to hover. High specific power comes

at a cost for batteries — lower specific energy, further limiting mission capability. The electric transmission appears to easily scale up, but with subpar energy availability, long range and/or high payload is out of the question. There are now worldwide efforts ongoing to scale up the all-electric concept, termed electric vertical takeoff and landing (eVTOL). The Vertical Flight Society (VFS) actively maintains a database of 1,000+ eVTOL concepts, manned and unmanned. A collage of concepts is shown in Fig. 1.7.

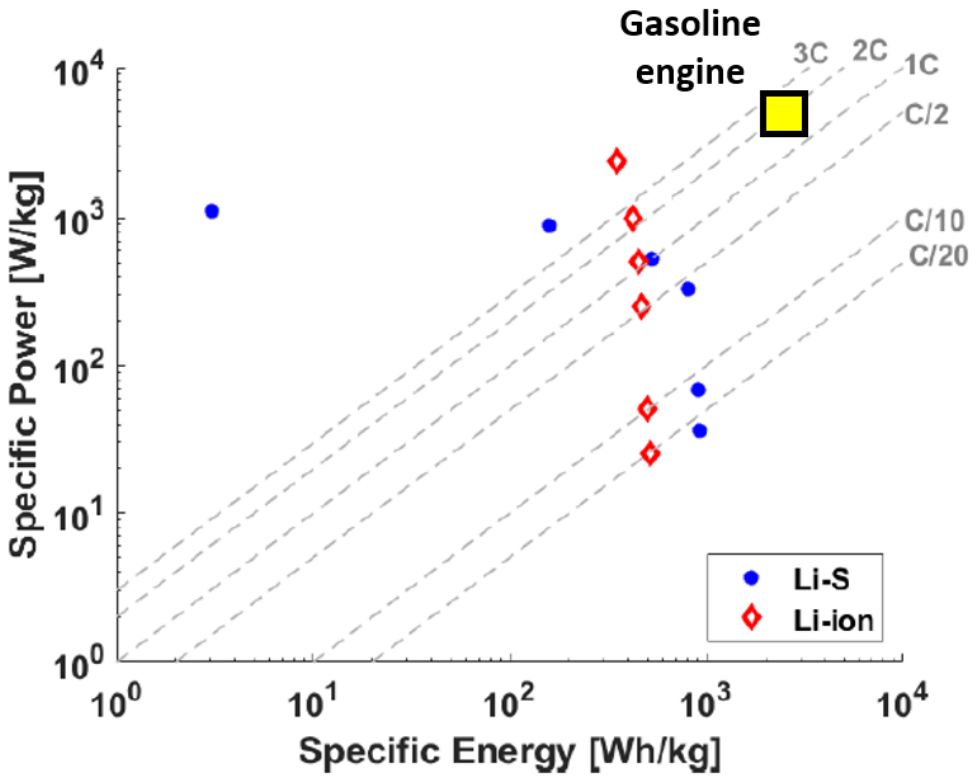


Figure 1.6: Energy density of tested Li-ion and Li-S cells relative to combustion based fuels.



Figure 1.7: A collage of eVTOL concepts ranging from personal air vehicles to passenger transport.

1.2 Why Hybrid-Electric?

A hybrid-electric power source retains the weight benefits of hydrocarbon fuel and combustion engine while still enabling the distributed propulsion architecture. It could be the key enabler to implementing distributed propulsion at larger scale. However, knowledge on hybrid-electric cannot simply be borrowed from ground vehicles, despite the success of and vast literature on hybrid-electric power for automobiles (see textbooks such as Refs. 8, 9). The mode of operation, guiding principles, and perceived/target benefits are fundamentally different. On the ground, the wheels turn faster with speed and their relative speeds are, by nature of ground contact, constrained to each other. In the air, the rotors must turn slower with speed and their speeds must be independent of each other. Indeed, the maximum speed is in hover when the aircraft is stationary. On the ground, the governing philosophy is regenerative braking. In the air, there is no such option; falling in a wind mill state at a high speed may be controllable, but is not a practical mode of flight.

The target benefit of long range, however, is common to both domains. In the air though, hybrid-electric is less an agent for better range and more an enabler of unmanned air vehicles that aspire

unprecedented agility and maneuverability. Often using four or more rotors, these configurations are prohibitive for mechanical transmissions, which do not enable independent rotor speed variation, but is easily done by hybrid-electric because of its electric transmission. The relatively poor reliability of electrical systems compared to mechanical systems is the only barrier that restricts the viability to unmanned air vehicles. Nevertheless, even if restricted to unmanned aircraft, such power systems may open up new missions and air mobility applications in commerce and defense.

1.3 Motivation

Compared to all-electric concepts, there is a significant lack of investment and buy-in around hybrid-electric. Literature on hybrid-electric fixed-wing aircraft has been emerging in the last decade [10–12] but most, if not all, are conceptual explorations. There is a scarcity of publicly available test data to reliably assess the concept. Literature and test data on hybrid-electric rotorcraft have been steadily emerging. In 2018, the company Workhorse developed the Surefly, shown in Fig. 1.8, a two seat hybrid-electric VTOL aircraft. The aircraft was flight tested, proving feasibility of hybrid-electric distributed propulsion, but no test data was ever published or released. In 2020, a study was carried out to design a conceptual 50 lb quadrotor biplane tailsitter (QBiT) [13], shown in Fig. 1.9. The study showed the advantages of a piston-electric hybrid for significant range extension over batteries. They recommended a 2-stroke engine (EL-005 Lycoming) with a weight budget of 9.89 kg and maximum continous power of 2.46 kW. This is a configuration similar to the 55 lb Bell APT 20. Subsequent work at the University of Maryland focused on a 2-stroke engine rig (DLE 40cc instead of Lycoming due to resource constraints) [14], shown in Fig. 1.10, which could be fabricated within 5.50 kg with a maximum continuous power of 3.10 kW. In 2022, Ricci, Varahamurthy, and Hicks [15] demonstrated

such systems can indeed be used to fly multi-rotor UAV, shown in Fig. 1.11. They also demonstrated how batteries can be strategically used to load-share and optimize the powerplant weight. The data and understanding acquired from these efforts provide the foundation of this dissertation, but much more data and understanding are required to reliably design an aircraft.



Figure 1.8: Workhorse Surefly two-seat hybrid-electric demonstrator.

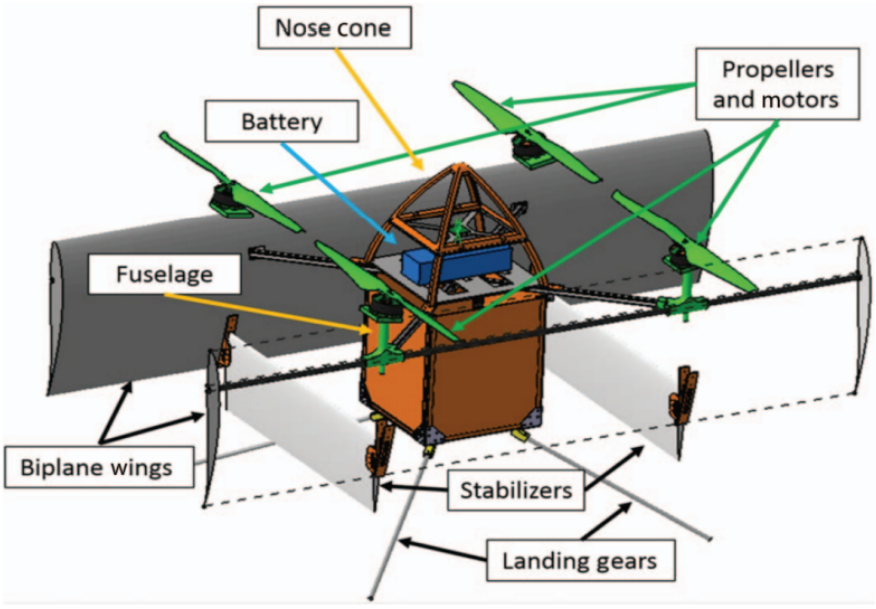


Figure 1.9: Conceptual 50 lb QBiT designed in 2020.

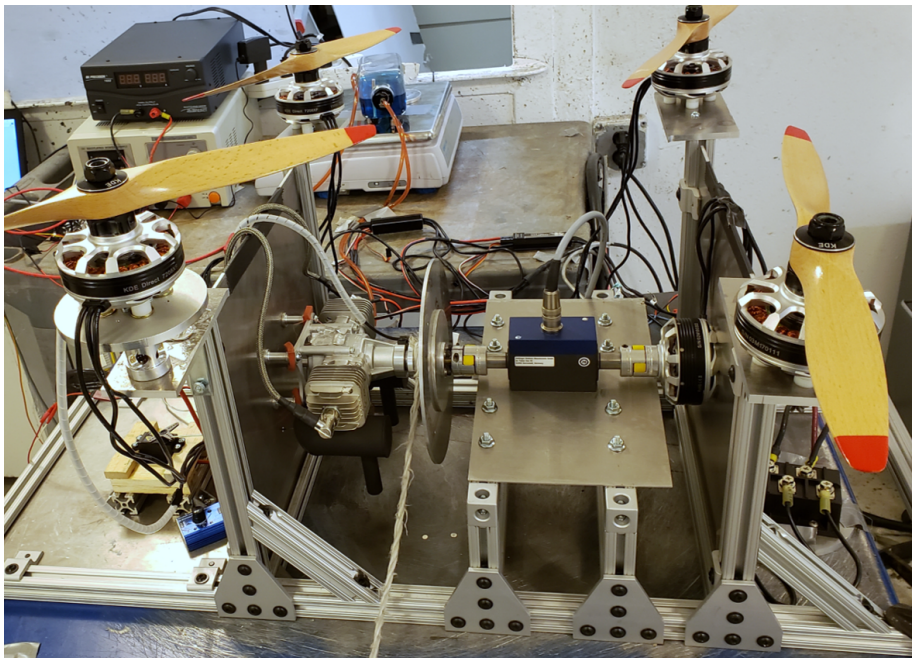


Figure 1.10: Piston-electric research rig with a 2-stroke engine at UMD and tested at Army Research Laboratory, Aberdeen during 2019-2022.



Figure 1.11: Hybrid-electric multi-rotor UAV demonstrator developed by LaunchPoint EPS.

In addition to the dearth of experimental data, existing analytical tools lack the functionality to assess the aeromechanics of hybrid-electric rotorcraft. Comprehensive analysis is a multi-disciplinary computational tool that integrates rotor aerodynamics, structural dynamics, and flight dynamics to predict rotorcraft behavior in any flight condition. It is the state-of-the-art in rotor aeromechanics analysis. The comprehensive analysis codes that exist today, shown in Fig. 1.12, have mostly been developed, validated, and fine-tuned for conventional rotorcraft configurations [16, 17]. For multi-rotor electric aircraft, many concepts have been designed using comprehensive analysis [18] but all lack rigorous validation. No test data exists at all to provide insights on aerodynamics or structural dynamics for rotors mounted on fixed, non-lifting structures (booms), or fixed, lifting structures (wings). Efforts to improve aerodynamic models to accommodate multi-rotor configurations are ongoing [19–21], but there is a lack of focus on structural dynamics, loads, and vibration. Therefore, there is a pressing need to further advance and validate comprehensive analyses to reliably predict the aeromechanics of these configurations.

It was stated that a hybrid-electric engine opens an opportunity for rotor speed variation during flight while retaining the benefits of a combustion engine. But, by how much should the speed be varied? Rotor aeromechanics benefits from as much speed reduction as possible to minimize power, whereas engines typically have a sweet spot elsewhere. What is the right trade off? Additionally, how should the speed be reduced – by the motors that directly turn the rotors, from the engine, or a combination of both? These are the questions that must be answered.

To convert the hybrid-electric concepts and demonstrations to a viable and practically beneficial aircraft, more test data is needed to understand the nature of hybrid-electric power generation, advanced analysis is needed to reliably assess the performance and structure of the aircraft, and a robust sizing analysis is needed to integrate power and platform. These, then, are the core objectives of this

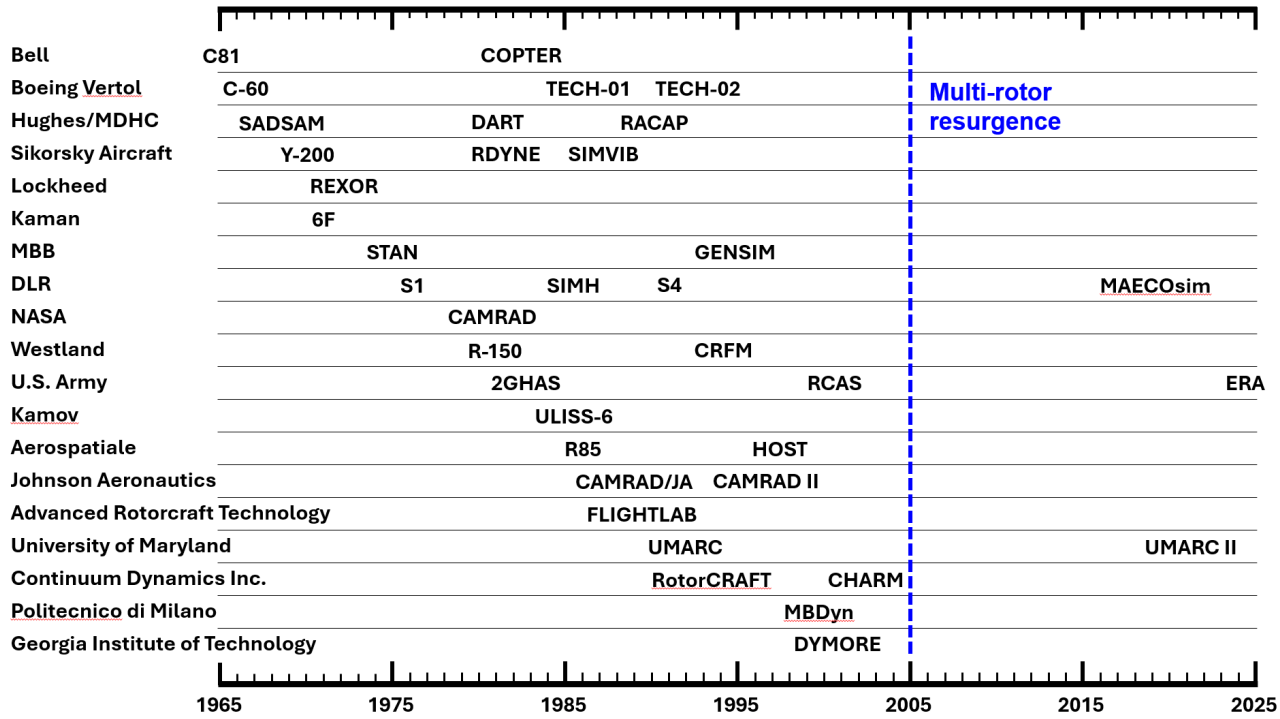


Figure 1.12: Timeline of comprehensive analyses developed over the last 60 years..

dissertation.

1.4 Definition of hybrid-electric power

In this dissertation, hybrid-electric is defined as a powerplant where a combustion engine is the primary power source and a generator converts the mechanical power to electrical for transmission and delivery to the electric motors that drive the rotors. A rectifier is used to convert the AC output of the generator to DC. This allows for independent control of each rotor and for the power to be supplemented by a battery downstream if desired. The fuel efficiency of the powerplant is characterized by the overall specific fuel consumption (SFC). A block diagram of a distributed power hybrid-electric architecture is shown in Fig. 1.13.

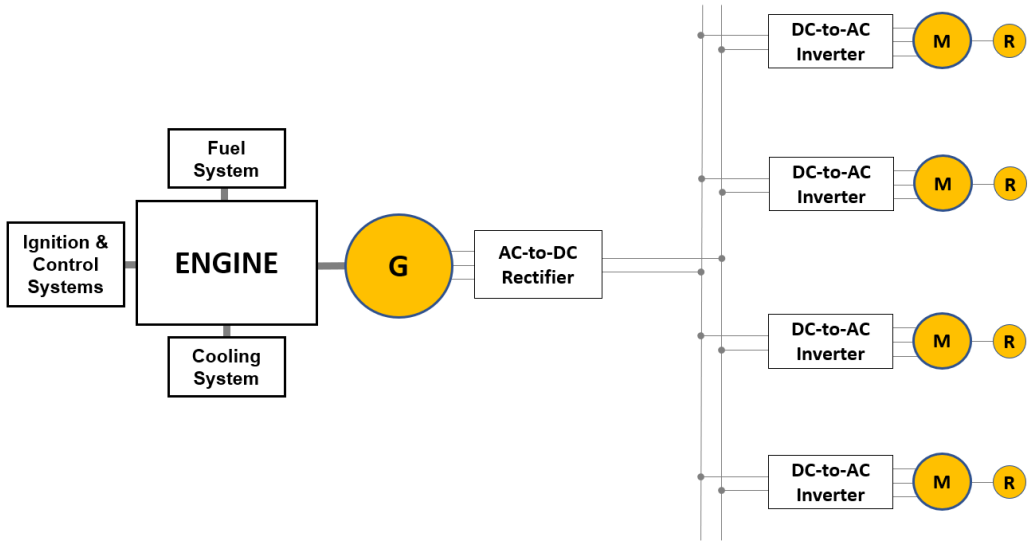


Figure 1.13: Block diagram of a distributed hybrid-electric powerplant with four rotors. G: Generator, M: Motor, R: Rotor.

1.5 Technical Approach

The principal barriers to answering the questions posed earlier are lack of test data and validated tools of analysis. Therefore, the technical approach of this dissertation is to combine experiments with modeling, first by fabricating and conducting fundamental studies on a small-scale hybrid-electric test rig, systematically building up the analysis to assess the performance and aeromechanics of a hybrid-electric configuration, and applying the understanding gained from both to size an example 50 lb hybrid-electric quadrotor biplane that seeks to take best advantage of such a powerplant.

1.6 Outline of dissertation

This dissertation is organized into four main chapters. Following the introduction, Chapter 2 details the experimental endeavor and discussion of the results. A 3.43 kW 4-stroke piston engine is coupled to a generator and rectifier to gain fundamental understanding of hybrid-electric power

generation on a small-scale. Isolated engine-generator tests are carried out using an electrical load bank to allow for mapping of the entire engine space. The SFC of the isolated engine, electrical efficiency, and overall SFC of the engine-generator set are characterized and understood.

In Chapter 3, in order to apply the basic knowledge gained in Chapter 2, a phenomenological model is developed from first principles and calibrated with the experimental data. This model predicts the fuel consumption of an isolated engine as a function of engine speed and torque. The model is rubberized for quantifying variations in engine efficiency with operating torque and RPM in a scale-invariant manner.

In Chapter 4, a comprehensive analysis of a quadrotor biplane is developed. This configuration is selected deliberately as it embodies the many key attributes of a hybrid-electric rotorcraft while offering many performance gains under rotor speed variation. A simple analysis is used to predict the L/D of the aircraft. The launch point for comprehensive analysis is UMARC-II, which is refined considerably to analyze multi-rotor, multi-wing configurations. There is no test data on such aircraft either, so the analysis is validated in pieces using the best available data from model to full-scale rotors.

Finally, in Chapter 5, the power and platform are brought together to answer the key questions. A 50 lb quadrotor biplane is sized using the engine model developed and calibrated with the experimental data, and using the performance predictions from the comprehensive analysis. A sensitivity study is conducted to understand the impact of including the detailed engine model versus assuming the SFC of the engine. Various modes of engine operation are explored to determine what combination of engine control and rotor tip speed reduction in cruise results in the maximum range 50 lb aircraft.

Chapter 6 summarizes the research, itemizes the key conclusions and contributions, and briefly discusses avenues of future work.

Chapter 2: Experiments on Hybrid-Electric Power Generation

This chapter details the experimental endeavor to understand the nature of hybrid-electric power generation using a 4-stroke engine. The test setup, data acquisition procedure, test data, and results are covered.

In this chapter, the engine is rigidly coupled to a generator and tests are carried out using an electrical load bank to allow for mapping of the entire engine space. The objectives of the engine-generator tests are to understand hybrid-electric power generation, component efficiencies, and overall efficiency of the powertrain across full operating range. Key measurements include the specific fuel consumption (SFC) of the engine and the power conversion efficiency of the generator and the rectifier at various torques and engine speeds in revolutions per minute (RPM).

2.1 Test Setup

Figure 2.1 shows the fabricated powertrain. The engine is connected to a shaft-to-shaft torque transducer. The other end of the transducer is connected to a generator. The three-phase AC output from the generator is connected to an AC-DC rectifier which is then directly connected to a constant current electrical load bank. The engine is mounted on a 3/4 inch thick plywood firewall for vibration damping and the system is mounted to a 6115 aluminum test frame.

A block diagram of the hardware and instrumentation is shown in Fig. 2.2. The rectangles in the

block diagram represent hardware components and the ellipses represent instrumentation.

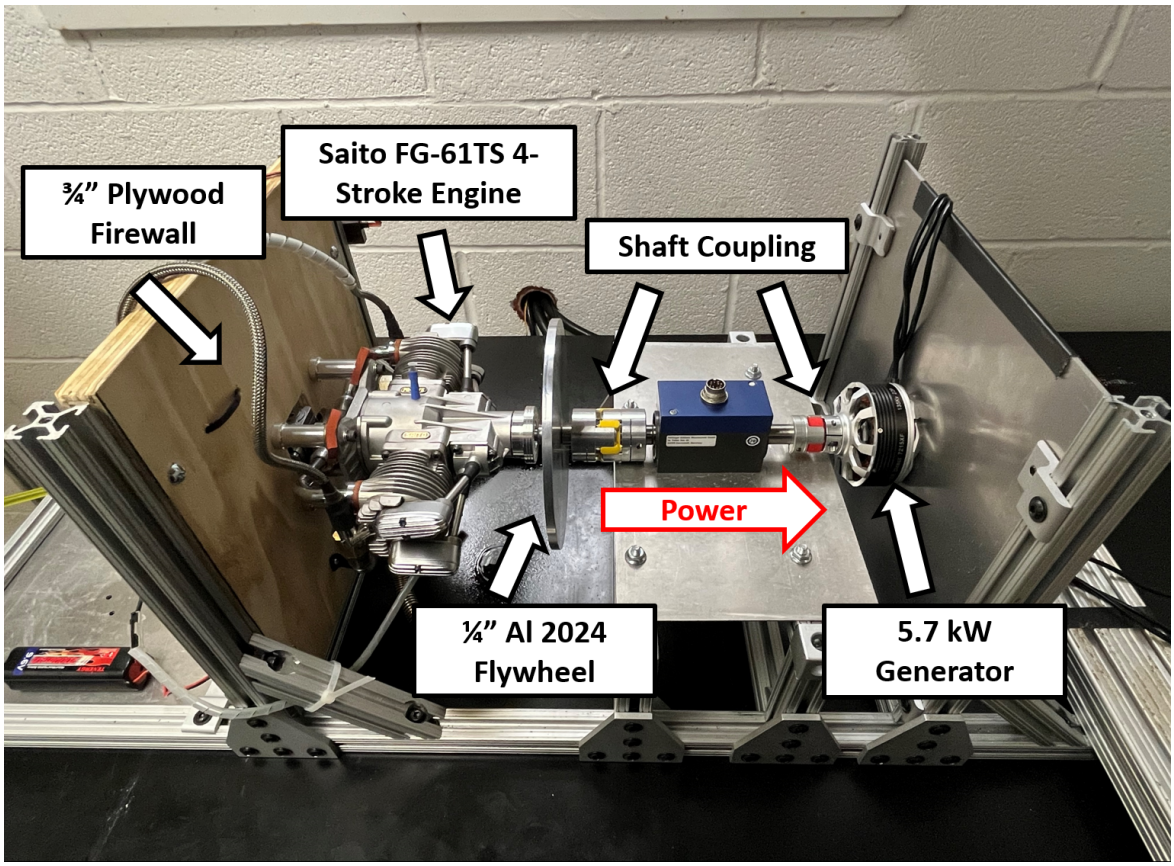


Figure 2.1: The 4-stroke piston-electric test rig.

2.2 Components of the powertrain

The engine is a Saito FG-61TS. It is a 4-stroke, 61cc engine that fits within the power and weight budget of the conceptual quadrotor biplane aircraft described in the introduction. It is an opposing twin cylinder internal combustion engine (ICE) weighing 2.26 kg with a maximum continuous power of 3.43 kW. The engine uses an Otto cycle with a fuel-oil mixture and therefore does not require separate lubrication. It is a 15-20:1 mixture of gasoline:engine oil. The components were acquired from a local hardware store and mixed by hand in the lab.

The engine was broken in and tuned by acquiring the manufacturer recommended propeller,

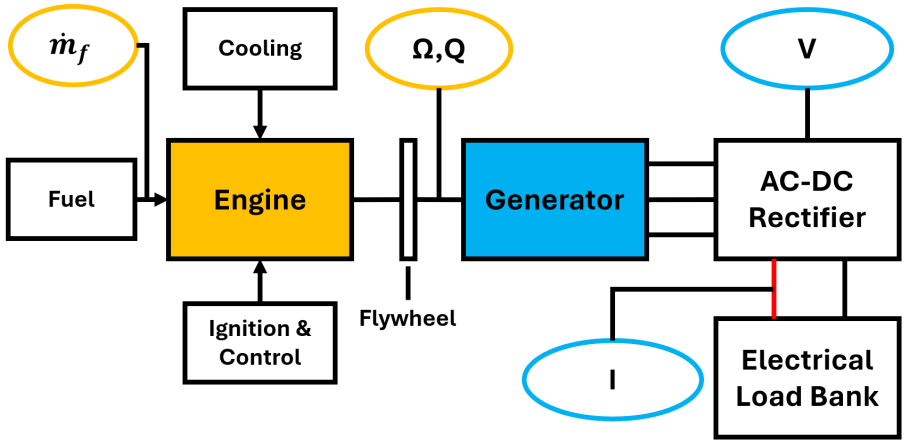


Figure 2.2: Block diagram of hardware and instrumentation. I: current, V: voltage, Ω: engine speed, Q: engine torque, $\dot{m}_f$: fuel mass flow from tank

mounting it on a mobile test stand, shown in Figs. 2.3 and 2.4, and relocating outside. Tuning inside was avoided because of the downwash from the propeller, despite the lab facility having a hood exhaust vent. Throttle was controlled using a Pulse Width Modulation (PWM) controller, a rotary servo, and throttle arm attached to the throttle lever on the carburetor. Two manually adjusted needles within the carburetor dictate the fuel-air mixture during engine operation. These can not be adjusted while the engine is mounted on the hybrid-electric test rig. The needles were set to achieve a maximum rotational speed of 7000 RPM. An ignition module and shaft-mounted Hall-effect sensor powered by an external battery control the firing of the spark plugs. Outside, air cooling is provided to the engine directly by the downwash from the propeller.

In the lab, air cooling is external and provided by an industrial fan pointed directly at the engine. To start the engine on the test rig, two additional components were required. Typically, a propeller mounted to the shaft of the engine provides enough rotational inertia to complete the compression stroke in each cycle. In the test setup, the shaft is rigidly connected to the generator and therefore lacks the necessary inertia to sustain operation, so a flywheel is machined and attached inline to the



Figure 2.3: Front of the test stand to break-in the engine.

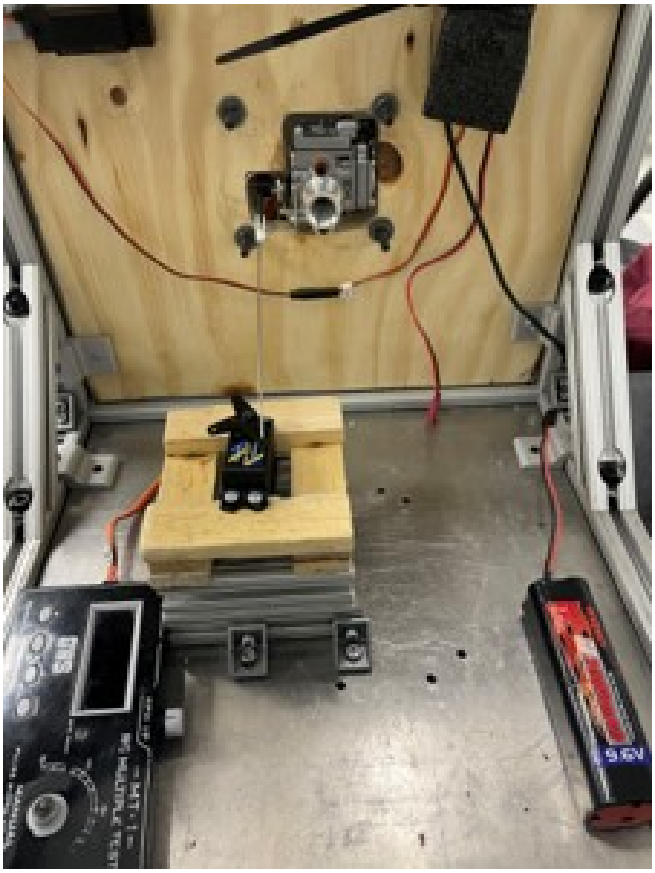


Figure 2.4: Rear of the test stand to break-in the engine.

shaft. Engines of this class rely on hand starting by flipping the propeller. This is not possible in the test setup as the end of the engine shaft is not free. Therefore, a pull-start mechanism is incorporated by wrapping a rope around the shaft and pulling it through several revolutions. When primed correctly, the cylinders will fire and the engine will start.

The generator, a KDE8218XF-120, is a brushless DC (BLDC) permanent magnet motor with trapezoidal signals configured to absorb torque and output current. The generator is rated for a maximum continuous power of 5.7 kW at 110 A and has a motor velocity constant of 120 RPM/V and a motor torque constant of 0.0796 N-m/A.

The AC-DC rectifier is a three-phase, six diode bridge rectifier. It converts the incoming three-phase AC from the generator to DC output. The rectifier is rated for 200 A DC and a maximum root-mean-square (RMS) voltage of 1600 V_{RMS}.

The load bank is a Eagle Eye LB-48-200-CC. It is a constant current electrical load bank used to consume the power output from the powertrain. The load bank is what allows us to precisely simulate load profiles to map the entire engine operating range.

2.3 Instrumentation

A National Instruments Data Acquisition System (DAQ) was used with LabVIEW as the software. A scale with ± 1 gram precision is used to measure fuel consumed during each test. Engine rotational speed Ω_E is measured using a Hall-effect sensor mounted to the engine shaft. The Hall-effect sensor is connected to a tachometer to display RPM during operation. Engine torque Q_E is measured using a HBM T21WN transducer powered by a 10V DC power supply. The DC Voltage, V, and current, I, are measured post-rectification. An 11:1 voltage divider is fabricated to reduce the

voltage signal to the acceptable range of the DAQ. The current is measured from the positive lead of the load bank using an Allegro ACS-700LCB-100U-PFF-T Hall effect sensor powered by a 5V DC power supply. The current passed through the sensor generates a magnetic field and the sensor outputs a constant square wave voltage based on the strength of the magnetic field. The current sensor is attached inline with the positive lead of the load bank. The output signal from the current sensor is configured to pass through a second-order RC filter, or a low pass filter, to convert the digital signal to a constant analog voltage value prior to passing to the DAQ. Data is collected at a rate of 2 kHz. The engine RPM and current drawn are independent and can be specified at will. This setup is open-loop with manual throttle control as conducive to parametric studies. The RPM is held constant for each test point manually through a throttle.

The true RPM is extracted from the frequency content of the torque signal. In the cylinder of a 4-stroke engine, there is a power stroke every other revolution of the crankshaft. In an opposing twin cylinder engine, the cycle of each cylinder is staggered, meaning there is a power stroke every revolution of the crankshaft. The power strokes are seen in the torque signal as peaks. Because there is one peak per revolution, the frequency of the torque signal is the rotational speed of the engine. The engine power is subsequently obtained as $P_E = Q_E \Omega_E$ and generator power is obtained from $P_G = VI$. The specific fuel consumption is $SFC = \dot{m}_f / P_E$ in $\frac{kg}{kW-hr}$ and the generator efficiency is $\eta_G = P_G / P_E$.

2.4 Test Procedure

Data is collected for the test cases shown in Fig. 2.5. Control of the system is open-loop. The engine speed is controlled using a PWM controller and rotary servo. The current drawn is set using the

load bank. The original test plan was to collect data up to 7000 RPM and up to 60 A. The engine was limited at high speeds due to vibrations that physically damaged the test rig. The engine was limited at low speed and high current due to the richness of the fuel-air ratio. Unburnt fuel and oil would build up in the engine leading to clogs and shutdown. It is suspected the engine was limited at high current in general due to the nature of passive rectification and quality control of the components themselves. Despite attempts to increase the current drawn, the torque output of the engine reached plateau around 54 A. That thread, however, is outside the scope of this work.

The following sequence is executed for each case.

1. The engine is started using the external pull-start and allowed to warm for one minute.

2. The RPM is adjusted to high idle, about 2,500 RPM, and the current load is set using the load bank. For the higher current cases, the current must be drawn gradually to allow the engine to react and supply the required torque. If too much torque is required instantaneously, the engine or powertrain components could be damaged. Therefore, the current drawn is increased in steps of 10 A up to the desired value.

3. The engine RPM is specified to the desired set point.

4. The fuel weight is recorded and data acquisition is initiated.

5. Data is collected until 20 g of fuel is consumed. Then the engine is shut down and allowed to cool.

6. The instantaneous data collected is averaged to return a single value of RPM, torque, current, and voltage. The efficiency metrics are then calculated.

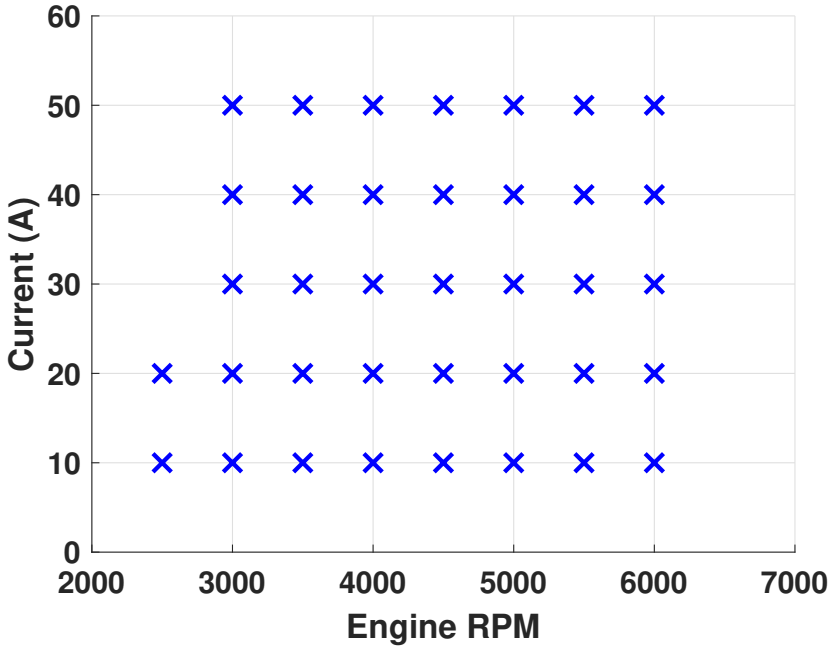


Figure 2.5: Test points collected.

2.5 Experimental Results

The measured data is tabulated in Table 2.1. The mechanical power, electrical power, generator efficiency and SFC can be calculated from this data.

The SFC is plotted with respect to engine RPM and torque in Fig. 2.6. The SFC of the isolated engine is inversely proportional to the thermal efficiency, which we will see mathematically in the following section. The efficiency islands appear clearly. Parametric curves are used to close the islands. To find the curves, the data is analyzed for two cases: constant torque and constant RPM. At a constant torque, the engine fuel mass flow $\dot{m}_f$ follows a cubic variation in RPM. An example is shown in Fig. 2.7. Similarly, at a constant engine speed, $\dot{m}_f$ follows a cubic variation in torque An example is shown in Fig. 2.8. The SFC is re-plotted in Fig. 2.9. The variation is now smooth and the islands close. Next, based on the clear trends, the RPM range is extended to 2000-7400 RPM and the

Table 2.1: Experimental data collected from piston-electric test rig with simulated load.

Engine Speed RPM	Current A	Voltage V	Torque N-m	Fuel Mass Flow Rate kg/hr
2530	10.08	16.48	0.784	0.474
2537	20.55	15.55	1.453	0.474
3030	10.09	19.91	0.786	0.518
3010	20.09	18.19	1.426	0.522
3030	30.55	16.91	2.015	0.426
3073	41.69	15.70	2.603	0.466
3093	50.22	14.37	3.008	0.507
3423	10.07	22.74	0.794	0.563
3454	20.44	21.15	1.427	0.581
3432	30.25	19.53	1.987	0.456
3673	40.67	19.44	2.532	0.467
3681	51.17	17.83	3.003	0.571
3997	10.12	26.65	0.797	0.580
3963	20.66	24.05	1.455	0.573
4078	30.43	23.66	2.040	0.504
4046	40.68	21.86	2.553	0.490
3969	50.12	19.64	2.990	0.589
4441	10.16	29.71	0.829	0.590
4501	20.25	28.11	1.439	0.590
4505	30.42	26.43	2.050	0.507
4569	40.45	25.22	2.568	0.554
4534	50.10	22.86	2.991	0.643
4997	10.18	34.50	0.843	0.645
4995	20.34	32.04	1.450	0.611
4998	30.21	29.76	2.021	0.525
4998	40.34	27.88	2.622	0.643
4996	50.06	26.97	2.990	0.790
5579	10.18	38.44	0.848	0.655
5508	20.43	35.01	1.465	0.621
5563	30.53	33.26	2.061	0.655
5568	40.94	31.46	2.643	0.776
5440	50.77	27.80	3.016	0.969
6000	10.17	40.72	0.855	0.655
6025	22.06	39.08	1.508	0.600
6018	31.07	36.42	2.066	0.762
6004	41.70	34.18	2.640	0.919
6014	50.50	31.82	3.012	1.161

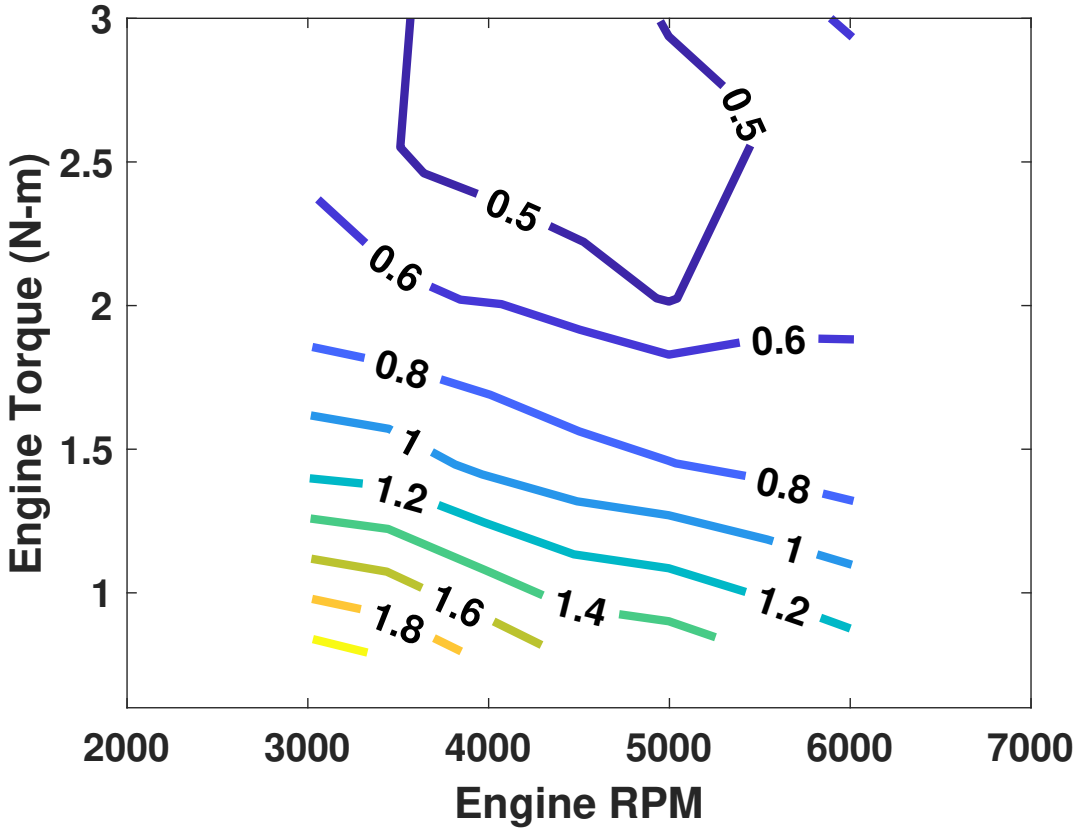


Figure 2.6: Engine SFC (kg/kW-hr) raw data contour

torque range to 0.8-4.4 N-m to cover the entire range of engine operation, beyond what the equipment used could measure. These extreme regions minimally impact the calibration of the model later. The extrapolated contour is shown in Fig. 2.10. Minimum SFC is observed around 4500 RPM and 2.6 N-m of torque.

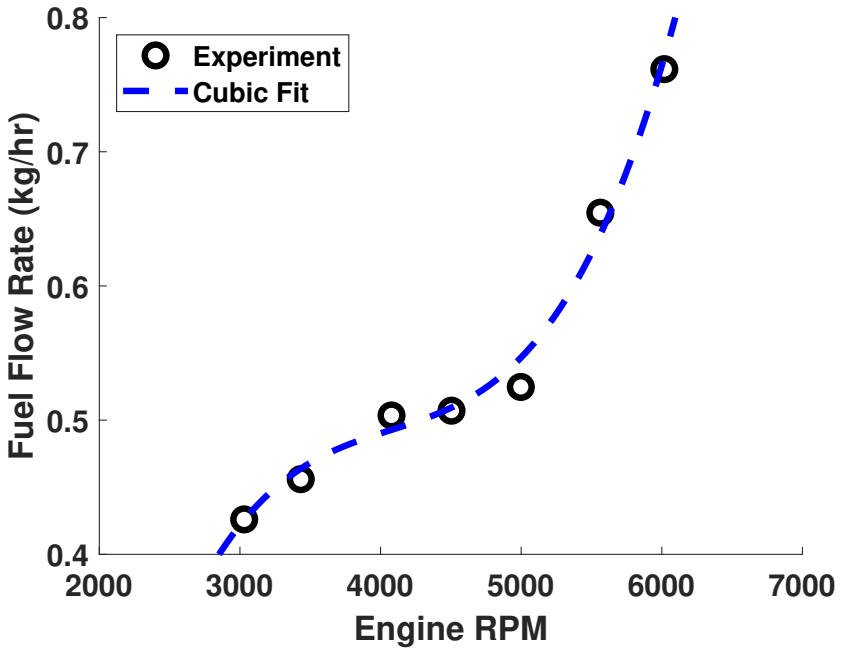


Figure 2.7: Engine fuel mass flow rate versus RPM at 2.0 N-m torque

The same data is plotted in Figure 2.11 now with engine power on the x-axis and engine SFC on the y-axis for constant RPM and constant torque. The constant RPM lines are solid and the constant torque lines are dashed. Along each RPM curve, the torque is increasing. The dashed line connecting the minimums of each RPM curve represents a torque of 2.66 N-m. While SFC is grossly a function of power, it is clear that SFC is more appropriately a function of both RPM and torque. At a desired RPM, there exists an engine power and torque where the SFC is minimized. At a desired engine power, it is generally more efficient to operate at lower RPM and higher torque. Below 1.5 kW, this holds true until the engine torque required exceeds 2.66 N-m. Then, it becomes more efficient to increase

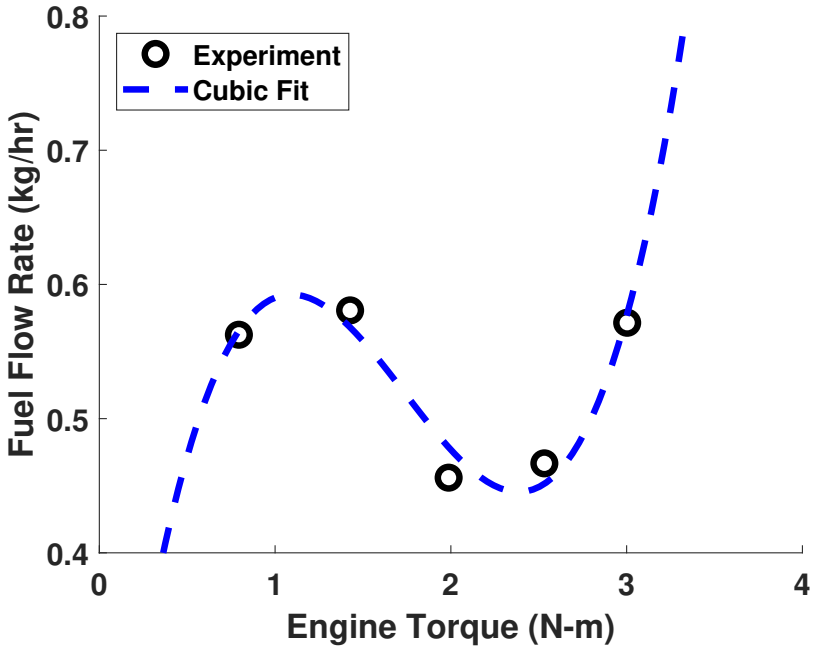


Figure 2.8: Engine fuel mass flow rate versus Torque at 3500 RPM.

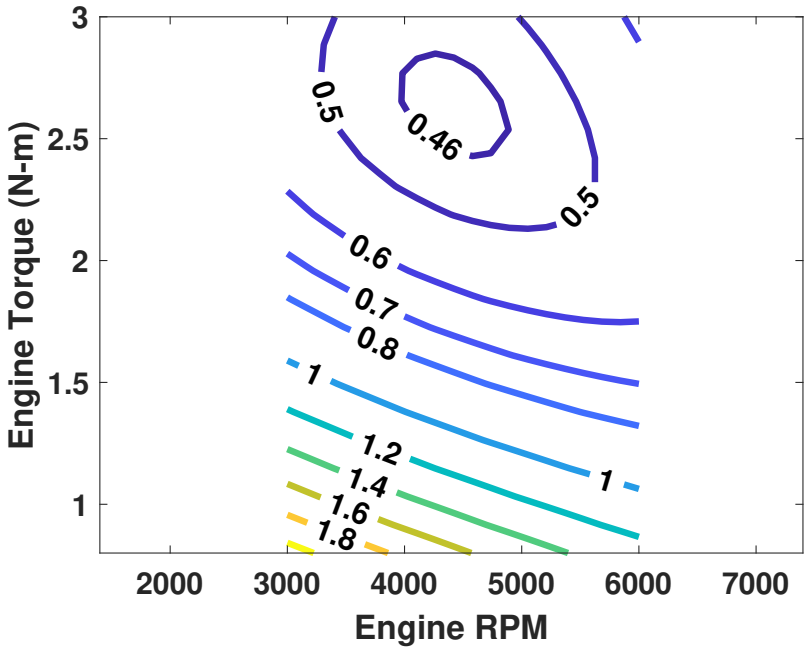


Figure 2.9: Measured engine SFC curve fit data contour in kg/kW-hr.

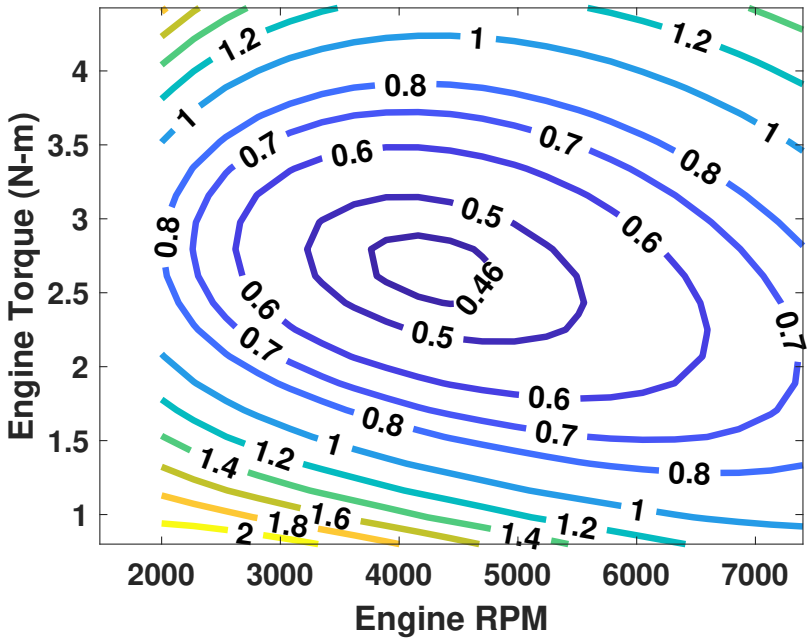


Figure 2.10: Measured engine SFC curve fit extrapolated data contour in kg/kW-hr.

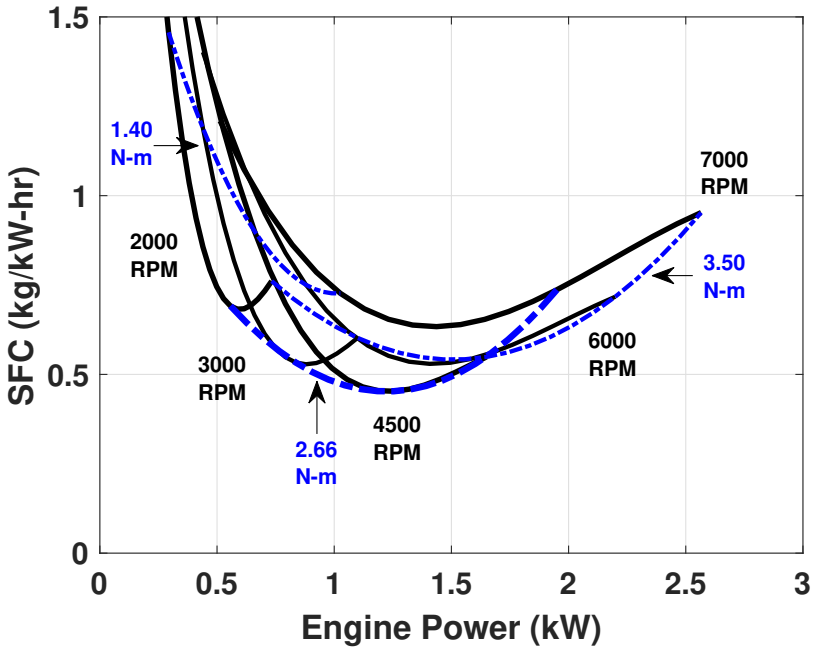


Figure 2.11: Engine SFC versus engine power with constant RPM lines (solid) and constant torque lines (dashed).

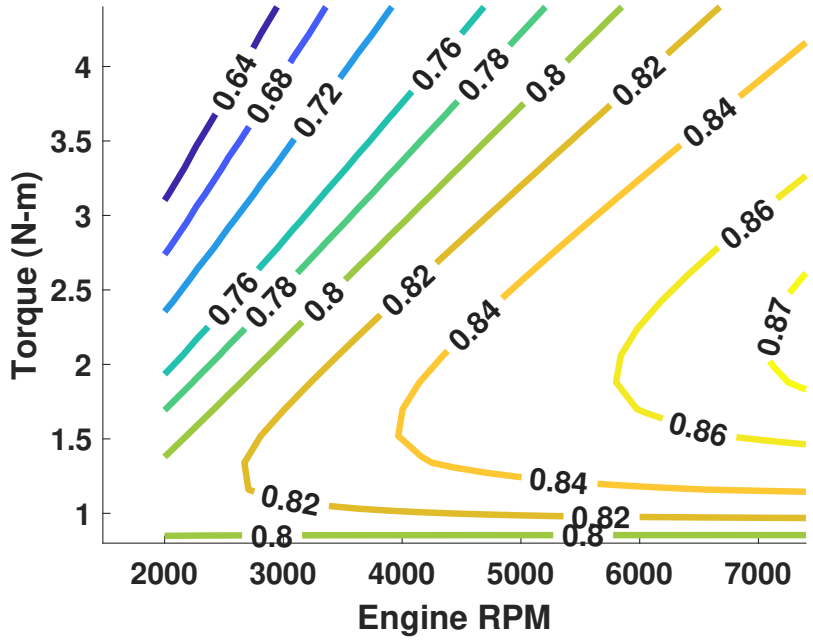


Figure 2.12: Generator efficiency curve fit extrapolated data contour.

RPM and reduce torque to below this limit. Above 1.5 kW, it is always more efficient to operate at lower RPM and higher torque. There is a specific RPM and torque where the engine SFC comes to an absolute minimum: 4500 RPM and 2.66 N-m. Based on this data it is optimal to operate this engine at 4500 RPM and 2.66 N-m, yielding 1.25 kW.

A similar exercise is conducted for the generator efficiency. A nonlinear surface is fit to the power lost from conversion. The generator efficiency plot for the same torque and RPM range is shown in Fig. 2.12. The generator efficiency islands are different than the SFC islands. The combination of these islands represent the efficiency of the power source. These SFC and generator efficiency maps are used for aircraft sizing in Chapter 5.

The electrical efficiency of the generator and rectifier combined is shown with constant power lines plotted. Figure 2.13 shows the electrical efficiency against voltage and current and Figure 2.14 shows the same efficiency against engine RPM and torque. The best efficiency is seen at high voltage

(or RPM) and moderate current (or torque). The optimal current and torque tends to increase as RPM and voltage are increased. If operating at a specific power, the generator is generally more efficient at higher RPM and lower torque. This is true except for low power/high RPM conditions. This trend is opposite that of engine SFC. Recall that in general the engine prefers a moderate RPM and higher torque. RPM is a proxy for voltage, based on the principle of Faraday's Law, and current is a proxy for torque, based on the principle of Ampere's Law, as are well-known for permanent magnet machines. However, the electrical efficiency island orientations change slightly between Figure 2.13 and 2.14. Analyzing the raw data in Table 2.1, at a constant RPM the voltage conversion is close to ideal at low current based on the velocity constant of the generator of 120 RPM/V. However, the voltage begins to drop as more current is drawn. This is due to increased ohmic losses from increasing current by $P = I^2R$. The current-torque relationship is relatively steady and linear as expected. Not much variation is observed between current and torque with varying RPM. Therefore, the voltage and current necessary to drive the rotors can be controlled through the RPM and torque provided by the engine with a caveat that the current drawn from the system also impacts the voltage supplied.

Generator efficiencies are plotted versus power. Figure 2.15 uses generator output power with constant voltage lines and Figure 2.16 uses generator input power with constant RPM lines. The generator output power is the electrical power post-rectification and the generator input power is identical to the engine shaft power output. Engine power increases as torque increases at a constant RPM. Likewise, the output power increases as current increases at a constant voltage. The trends are identical. Generator efficiency reaches a maximum at high RPM and moderate torque, or high voltage and moderate current. If operating at a desired power, it is generally more efficient to choose higher RPM, or voltage, and lower torque, or current. However, this does not hold true in lower power conditions. In the power range below 0.75 kW, the optimal operating condition shifts to a moderate-to-low RPM,

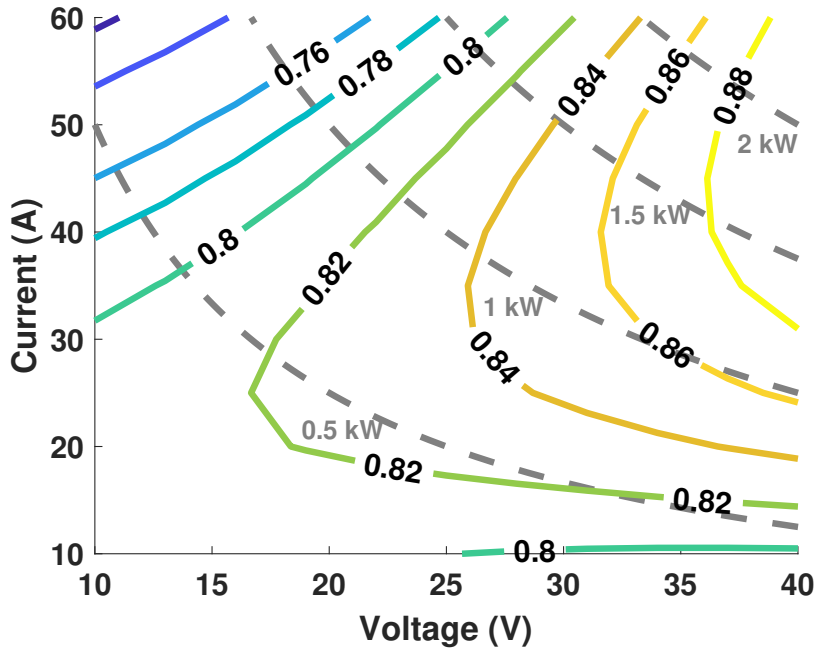


Figure 2.13: Generator efficiency contour versus voltage and current

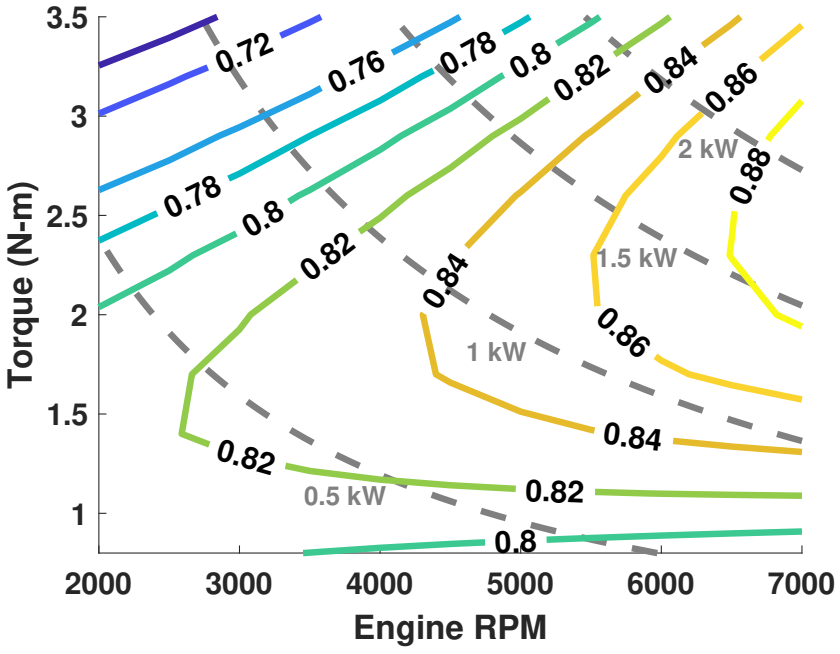


Figure 2.14: Generator efficiency contour versus RPM and torque

or voltage, and higher current, or torque, depending on the power required. Comparing Figure 2.15 and 2.16, it is important to note the difference in crossings of the curves. This is again due to the reduction in voltage output from increased ohmic losses showing that RPM and voltage output are not one-to-one. Therefore, current can be considered a proxy for torque and RPM may be considered a proxy for voltage but only as long as the impact on voltage output due to ohmic losses are low.

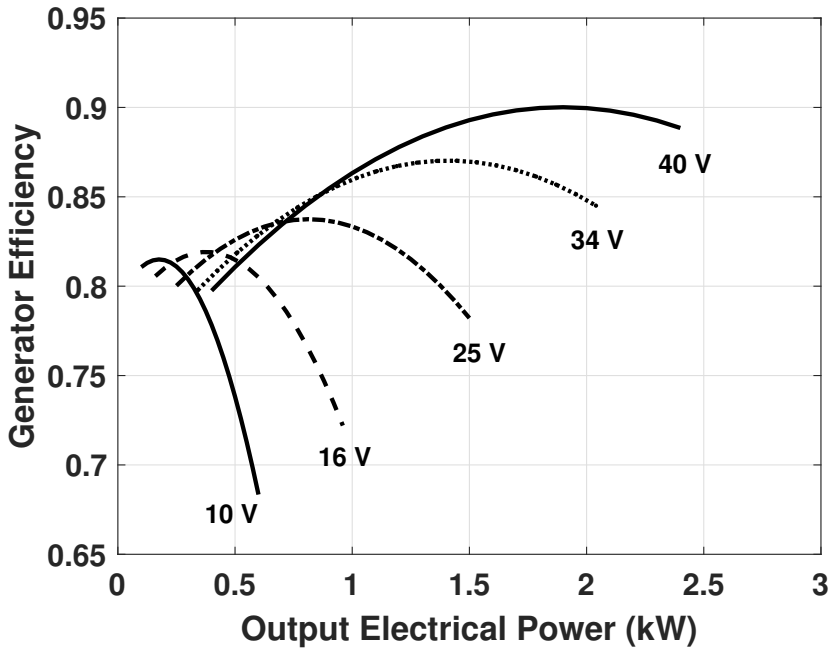


Figure 2.15: Generator efficiency versus power. Constant voltage lines.

Finally, the SFC of the coupled engine-generator is plotted in Figures 2.17 and 2.18 with constant power lines. This is calculated by SFC/η_G and thus represents the behavior of the integrated system. It can clearly be seen that the system as a whole operates most efficiently at moderate RPM and high torque. Recall the isolated engine preferred moderate RPM and high torque up to 2.66 N-m while the generator preferred high RPM and moderate torque. Therefore the engine is the primary driver of system efficiency. In Fig 2.17, the efficiency islands follow similar trends to the isolated engine although the introduction of the generator has a negative impact on SFC as the best SFC is now 0.56

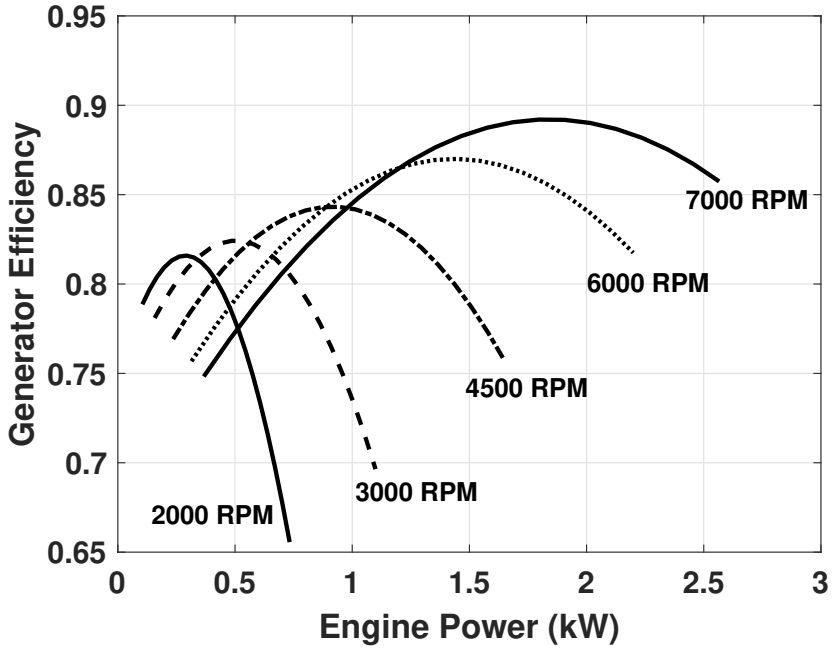


Figure 2.16: Generator efficiency versus power. Constant RPM lines.

compared to 0.46. Additional variation is introduced from the generator across the operating range with respect to RPM and torque, especially at higher torques compared to Fig. 2.6. However, it is still optimal to operate this engine at around 4500 RPM and 2.66 N-m.

Slightly different behavior is seen in Fig. 2.18. This is now the SFC of the coupled engine-generator system against voltage and current. This contour map of SFC is important as it gives the full picture of the powerplant from the perspective of the designer. The designer would specify the voltage and current requirements of the powerplant in conjunction with rotor design. The engine design point in RPM and torque would then be deduced from the voltage and current required. The efficiency islands are elongated at higher voltage. This behaviour is a result of the high generator efficiency at high voltage and moderate current. Higher order variations are observed due to the losses in power conversion. At a constant power however, it is still more efficient to operate at lower voltage and high current except within the most efficient operating range of the engine-generator set. A specific

operating condition in voltage and current exists to achieve an absolute minimum SFC. The optimal electrical conditions are found at 25 V and 40 A, yielding 1 kW of output power. These contours show that isolated engine SFC and generator efficiency are not adequate efficiency metrics on their own. The designer must understand the impact from the presence of the generator to account for reductions in efficiency and island shifting.

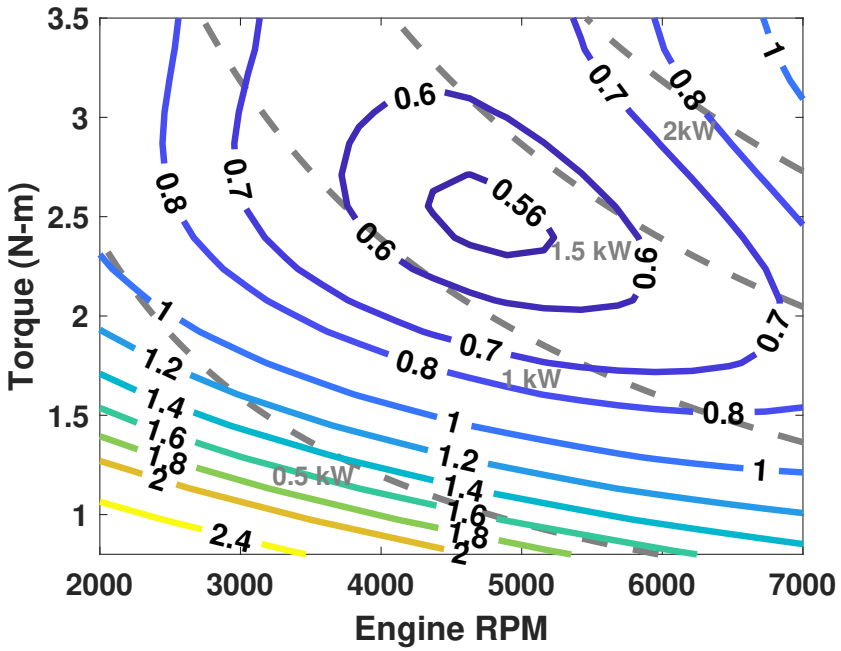


Figure 2.17: SFC/η_G versus RPM and torque

2.6 Summary and Conclusions

This chapter detailed the experimental endeavor to understand the nature of hybrid-electric power generation using a 4-stroke engine. The test setup, data acquisition procedure, test data, and results were covered.

A 3.43 kW 4-stroke piston engine was coupled to a generator and rectifier to acquire basic data on power generation. The isolated engine, generator, and coupled engine-generator efficiencies were

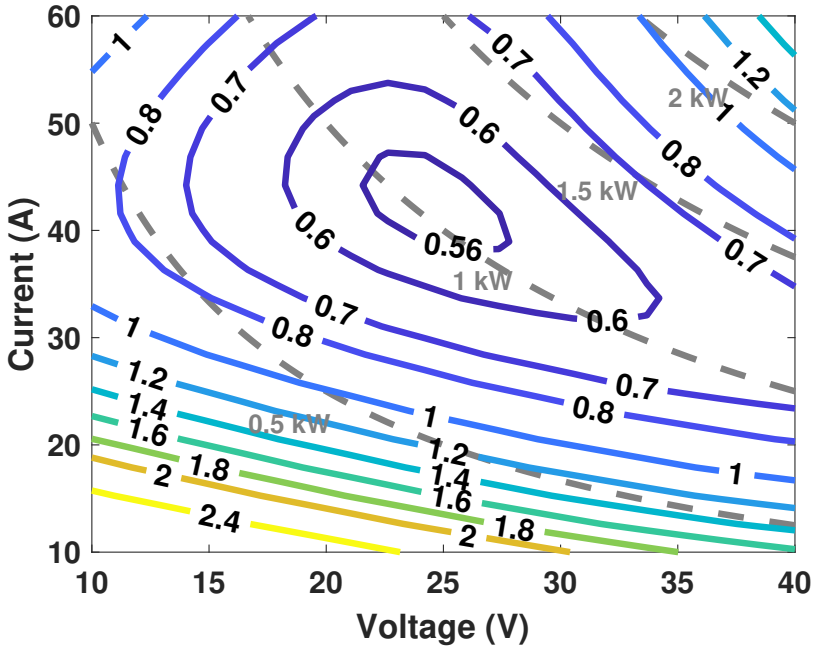


Figure 2.18: SFC/η_G versus voltage and current

characterized. Based on this work, several key conclusions are drawn.

1. Isolated engine SFC and generator efficiencies are not adequate efficiency metrics on their own; the coupled engine-generator efficiency is required to accurately represent the behavior of the system and its impact on aircraft design.

2. The specific fuel consumption (SFC) is a strong function of both voltage and current, not just power. At a desired power output there can be a large number of feasible engine operating conditions. The designer must understand what combinations of voltage and current result in the lowest fuel consumption. At least for the present engine, at a desired power it is more efficient to operate at high current (high torque) and moderate voltage (moderate RPM).

3. An operating condition can be found to achieve a minimum SFC. For the current rig, that condition is 1 kW of output electrical power at 25 V and 40 A.

4. Current may be considered a proxy for torque and voltage may be considered a proxy for RPM for permanent magnet generators but only as long as the impact on voltage output due to ohmic losses is well understood. The RPM to voltage conversion of the generator should not be assumed as ideal, especially at high current.

The experimental data can now be used to develop, validate, and calibrate an engine model to predict the engine efficiency based on operating condition.

Chapter 3: Modeling of Hybrid-Electric Power Generation

This chapter details the mathematical model developed to predict the fuel consumed of a 4-stroke engine.

In this chapter, a physics-based, semi-empirical model is developed to predict the fuel consumption of a 4-stroke engine based on operating engine speed and torque. The model is non-dimensionalized to quantify variations in engine efficiency with operating torque and speed in a scale-invariant manner.

3.1 Mathematical Model

Although table look-up could be used for sizing, a mathematical model is desired for scaling. Generator and motor models are well-developed in literature. See for example Ref. [22], so attention is devoted here on the engine SFC map.

The derivation of the model begins from the power balance. The power input by the fuel is fuel mass flow rate, $\dot{m}_f$ (kg/s), multiplied by the Net Calorific Value (NCV) (J/kg). The indicated thermal efficiency η_T converts power input by the fuel to useful power called indicated power via combustion, $P_I = \eta_T \dot{m}_f NCV$. The indicated power consists of power output of the engine called brake power P_B, friction loss, P_F, and pumping loss, P_P. The pumping loss P_P is specific to a $4-$stroke engine; there is no pumping loss on a 2-stroke engine. Thus the power balance is,

$$P_I = P_B + P_F + P_P \tag{3.1}$$

where,

$$\eta_T \dot{m}_f NCV = P_I. \tag{3.2}$$

The brake power is output torque times shaft speed $P_B = Q_E\,\Omega_E$. Another efficiency, the brake thermal efficiency η_B, converts the power input by the fuel directly to this power.

$$\eta_B \dot{m}_f NCV = P_B. \tag{3.3}$$

Dividing Eq. 3.3 by Eq. 3.2 gives

$$\eta_B = \eta_T \left(\frac{P_B}{P_B + P_F + P_P} \right) = \eta_T\,\eta_M. \tag{3.4}$$

The mechanical efficiency, η_M, converts indicated power to brake power. From Eq. 3.2, the fuel mass flow rate can be written as,

$$\dot{m}_f = \frac{P_B}{\eta_T NCV} \left(1 + \frac{P_F + P_P}{P_B} \right). \tag{3.5}$$

The brake power P_B is related to the mean effective pressure inside the cylinder, $bmep$. If the cylinder volume is V_S the work done in one cycle is $bmep\,V_S$. If the engine speed is Ω_E in rad/s, $\Omega_E/(2\,\pi)$ is the number of revolutions per second, then $\Omega_E/(2\,\pi\,n_c)$ is the number of cycles per second ($n_c = 2$ for a $4-$stroke engine). The work done per cycle times cycles per second is power,

$P_B = bmep\, V_S\, \Omega_E/(2\,\pi\, n_c)$. Because $P_B = Q_E\, \Omega_E$, it follows $bmep = 2\,\pi\, n_c\, Q_E/V_S$. The ratio of powers can be redefined as the ratio of equivalent mean effective pressures. Thus,

$$\dot{m}_f = \frac{Q_E\, \Omega_E}{\eta_T NCV}\left(1 + \frac{fmep + pmep}{bmep}\right) \tag{3.6}$$

$$bmep = \frac{2\,\pi\, n_c\, Q_E}{V_S}. \tag{3.7}$$

In non-dimensional form,

$$\overline{\dot{m}}_f = \frac{\dot{m}_f\, NCV}{Q_{E_{max}}\, \Omega_{E_{max}}} = \frac{\overline{Q}_E\, \overline{\Omega}_E}{\eta_T}\left(1 + \frac{fmep + pmep}{bmep}\right) \tag{3.8}$$

$$\overline{bmep} = \frac{bmep\, V_S}{Q_{E_{max}}} = 2\pi n_c \overline{Q}_E, \tag{3.9}$$

where the nondimensional engine torque is $\overline{Q}_E = Q_E/Q_{E_{max}}$ and nondimensional engine RPM is $\overline{\Omega}_E = \Omega_E/\Omega_{E_{max}}$. The variables $\dot{m}_f$, Q_E, and Ω_E are measured. NCV is known from the fuel used and the swept cylinder volume V_S is known from the engine geometry. Thus η_B is known at each test point. The goal is to find a functional representation of η_B in terms of Q_E and Ω_E.

We have from Eq. 3.3 and 3.6,

$$\frac{1}{\eta_B} = \frac{1}{\eta_T}\left(1 + \frac{fmep + pmep}{bmep}\right) \tag{3.10}$$

The brake mean effective pressure is known in terms of Q_E but η_T and the losses $fmep + pmep$ are not. These are very difficult to predict and where empirical data enters the model. It was found

that $pmep$ is best approximated by a 3^{rd} order function of engine speed. This result was obtained by progressively refining the model from linear, to nonlinear, to nonlinear with pumping losses. Data from other $4-$stroke engine tests also suggest that $(fmep+pmep)/bmep$ varies by 3^{rd} order in engine speed and inversely with engine torque ([23, 24]). Since $bmep$ is already a function of torque, we propose $fmep + pmep$ to have the following form.

$$fmep + pmep = A_0 + A_1\,\overline{\Omega}_E + A_2\,\overline{\Omega}_E^2 + A_3\,\overline{\Omega}_E^3. \tag{3.11}$$

The problem now lies with η_T. The indicated thermal efficiency is normally a very complicated higher order function of Q_E and Ω_E and can vary from engine to engine. For 2-stroke engines Goering and Cho (1988) [25] proposed

$$\eta_T = \frac{\eta_{T0}}{1 + Q_E^n\, g(\Omega_E^4)}. \tag{3.12}$$

They found for a $2-$stroke engine at low torque $\eta_T \approx \eta_{T0}$ where η_{T0} is a constant and f is a fourth order polynomial in Ω_E. This was used to calibrate $fmep$. A $2-$stroke engine does not have $pmep$.

Mills proposed η_T is best described by a mean efficiency divided by a torque and angular velocity variation functions [26], similar to Goering and Cho.

$$\eta_T = \frac{\eta_{T0}}{1 + f(Q_E^2)\, g(\Omega_E^4)}. \tag{3.13}$$

The model calibration is systematically built up with these former models in mind.

3.2 Linear Model

An initial attempt to model the fuel consumed assumed, first, $pmep$ is negligible compared to $fmep$ and second, there is no variation in the thermal efficiency η_T. This would be the simplest linear model.

$$\frac{1}{\eta_B} == \frac{1}{\eta_{T0}} \left(1 + \frac{fmep}{bmep}\right) \tag{3.14}$$

$$fmep = A_0 + A_1 \overline{\Omega}_E + A_2 \overline{\Omega}_E^2 \tag{3.15}$$

These results are shown in the SFC contour in Figure 3.1. In this model, only four constants need to be calibrated with the experimental data: η_{T0}, A_0, A_1, and A_2 requiring a minimum of only four test points. The solid lines plot the contour of the experimental data and the dashed lines represent the model approximation. The trends across the engine operating range are wrong. Clearly, this is an incorrect model of the engine behavior.

3.3 Nonlinear Model

The next refinement re-introduced the nonlinear variation in engine speed and torque for thermal efficiency. The only assumption is that $pmep$ is negligible relative to $fmep$ making this model phenomenologically the exact same as that developed to predict 2-stroke engine performance [27], only the constants are different. The nonlinear contribution is,

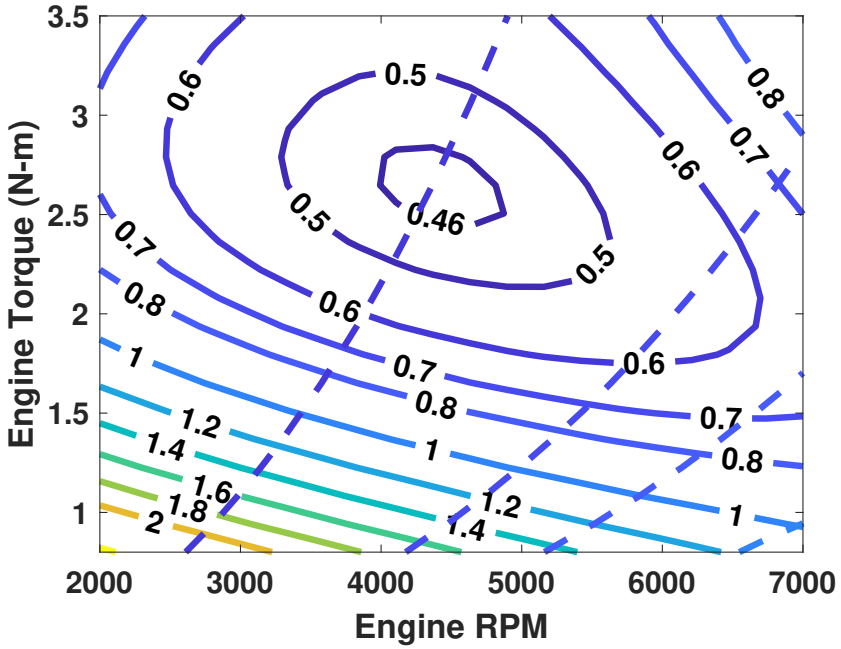


Figure 3.1: Incorrect model. Constant thermal efficiency. Pumping power neglected. Data (lines) versus prediction (dashed).

$$\frac{1}{\eta_B} = \frac{1}{\eta_{T0}} \left(1 + \frac{fmep}{bmep}\right) (1 + fg) \tag{3.16}$$

$$1 + fg = B_0 + B_1\,\overline{\Omega}_E + B_2\,\overline{Q}_E + B_3\,\overline{\Omega}_E^2 + B_4\,\overline{\Omega}_E\,\overline{Q}_E +$$

$$B_5\,\overline{Q}_E^2 + B_6\,\overline{\Omega}_E^3 + B_7\,\overline{\Omega}_E^2\,\overline{Q}_E + B_8\,\overline{\Omega}_E\,\overline{Q}_E^2 + B_9\,\overline{\Omega}_E^4 + B_{10}\,\overline{\Omega}_E^3\,\overline{Q}_E +$$

$$B_{11}\,\overline{\Omega}_E^2\,\overline{Q}_E^2 + B_{12}\,\overline{\Omega}_E^3\,\overline{Q}_E^2 + B_{13}\,\overline{\Omega}_E^4\,\overline{Q}_E + B_{14}\,\overline{\Omega}_{E_m}^4\,\overline{Q}_E^2$$

In this model, 15 constants, B_0-B_{14}, are required in addition to η_{T0}, A_0, A_1, and A_2 to calibrate the nonlinear terms in fg bringing the total number of unknowns to 19. These results are shown in Figure 3.2. The solid lines once again represent the experimental data and dashed represent the model.

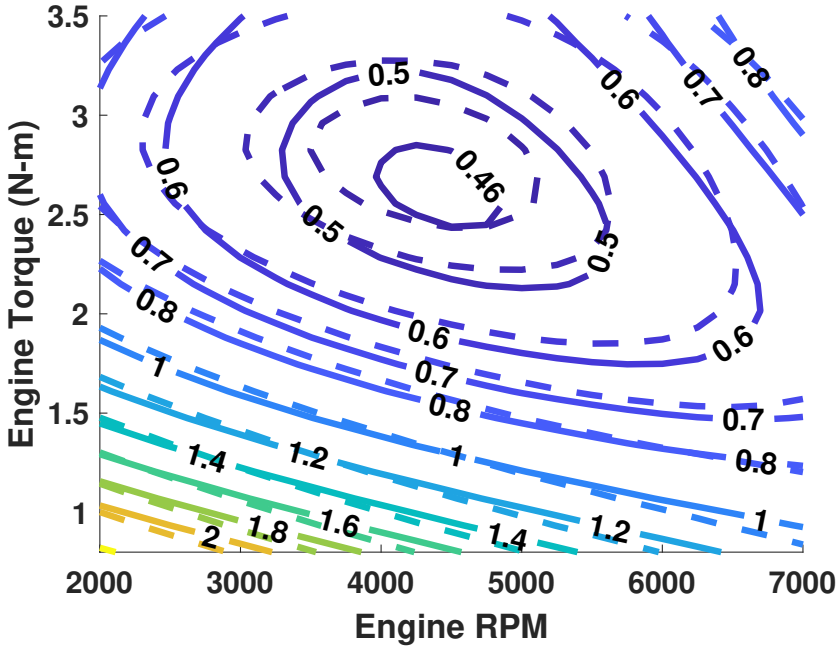


Figure 3.2: Refined model 1. Nonlinear thermal efficiency. Pumping power neglected. Data (lines) versus predictions (dashed).

In this model the trends are at least captured even though the magnitudes are incorrect. The reduction in SFC is predicted at low torque with increasing engine speed. It is clear then the nonlinear variation in thermal efficiency is extremely important to model the behavior. However, this approximation does not adequately capture the SFC at higher torque and engine speed indicating the presence of additional losses that are not accounted for in the model. The behavior of SFC at higher engine speed indicates the fuel flow rate is a higher order function in engine speed compared to the 2-stroke engine. The maximum error in this model is 7.41% with an average error across the data range of 3.21%.

3.4 Nonlinear Model with Pumping

In the next refinement of the engine model, based on a study of the data it is conjectured that $pmep$ can be approximated by a 3^{rd} order function in engine speed.

$$fmep + pmep = A_0 + A_1\overline{\Omega}_E + A_2\overline{\Omega}_E^2 + A_3\overline{\Omega}_E^3 \tag{3.17}$$

This introduces one additional constant bringing the total number of unknowns to 20. These results are shown in Figure 3.3.

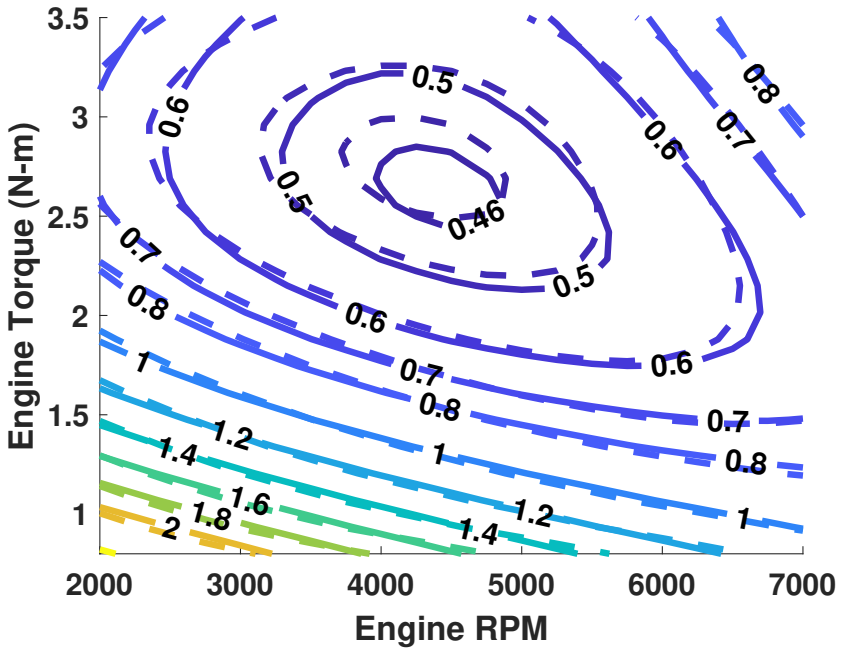


Figure 3.3: Refined model 2. Nonlinear thermal efficiency. Pumping Power included. Data (lines) versus predictions (dashed).

A much better agreement is seen between the approximation and the experimental data, especially at high torque and high engine speed. The SFC is well captured at high engine speed and the efficiency islands are well captured at high torque. However, there is still slight disagreement in trend. We believe the indicated thermal efficiency does not follow the form proposed by Goering and Cho or Mills for a 2-stroke engine. Instead, we propose

$$\eta_T = \frac{1}{f(\overline{Q}_E^3)g(\overline{\Omega}_E^3)}. \tag{3.18}$$

We found a torque and speed range where a simpler approximation held,

$$\eta_T \approx \frac{1}{b_0 + b_1\overline{\Omega}_E + b_2\overline{Q}_E}. \tag{3.19}$$

This range was $2200 - 4500$ RPM and $0.9 - 1.2$ N-m. This range was used to calibrate $fmep + pmep$. For the purposes of that calibration,

$$\frac{1}{\eta_B} = \left(1 + \frac{A_0 + A_1\,\overline{\Omega}_E + A_2\,\overline{\Omega}_E^2 + A_3\,\overline{\Omega}_E^3}{\overline{Q}_E}\right)(b_0 + b_1\overline{\Omega}_E + b_2\overline{Q}_E) \tag{3.20}$$

Once $A_0 - A_3$ are obtained, we revert back to the full expression of Eqn. 3.18 to calibrate η_B over the entire engine range.

$$\frac{1}{\eta_B} = \left(1 + \frac{A_0 + A_1\,\overline{\Omega}_E + A_2\,\overline{\Omega}_E^2 + A_3\,\overline{\Omega}_E^3}{\overline{Q}_E}\right) fg \tag{3.21}$$

$$fg = B_0 + B_1\,\overline{Q}_E + B_2\,\overline{Q}_E^2 + B_3\,\overline{Q}_E^3 + B_4\,\overline{\Omega}_E + B_5\,\overline{Q}_E\,\overline{\Omega}_E +$$
$$B_6\,\overline{Q}_E^2\,\overline{\Omega}_E + B_7\,\overline{Q}_E^3\,\overline{\Omega}_E + B_8\,\overline{\Omega}_E^2 + B_9\,\overline{Q}_E\,\overline{\Omega}_E^2 + B_{10}\,\overline{Q}_E^2\,\overline{\Omega}_E^2 +$$
$$B_{11}\,\overline{Q}_E^3\,\overline{\Omega}_E^2 + B_{12}\,\overline{\Omega}_E^3 + B_{13}\,\overline{Q}_E\,\overline{\Omega}_E^3 + B_{14}\,\overline{Q}_E^2\,\overline{\Omega}_E^3 + B_{15}\,\overline{Q}_E^3\,\overline{\Omega}_E^3$$

The model constants are listed in Table 3.1. Because they are non-dimensional and based on observed behavior of friction and pumping losses, we assume they are nominally representative of small scale four-stroke engines. The predicted fuel mass flow rate, specific fuel consumption, and brake thermal efficiency are plotted over the experimental data in Figs. 3.4, 3.5, and 3.6. The function

is evaluated across the engine operating range and specific fuel consumption is plotted versus engine power against the experimental data shown in Figure 3.7. The trends are satisfactorily captured. The model is now considered sufficiently accurate to be used in aircraft sizing.

Table 3.1: Calibrated model constants of scalable engine SFC model.

A_0	0.0268	B_1	79.383	B_6	778.58	B_{11}	277.80
A_1	0.4552	B_2	-173.91	B_7	-389.13	B_{12}	57.691
A_2	-1.0207	B_3	127.72	B_8	-154.29	B_{13}	-226.90
A_3	0.8034	B_4	92.491	B_9	751.11	B_{14}	107.96
B_0	9.5011	B_5	-603.95	B_{10}	-718.54	B_{15}	-1.2802

The indicated thermal efficiency and mechanical efficiency obtained from the model are shown in Fig. 3.8 and 3.9. The losses are roughly $10-30\%$ of the brake power at the nominal operating range of the engine. These losses are solely a function of engine speed. Friction increases at higher speeds. It is reasonable to expect friction force to be proportional to velocity, similar to a viscous damper, so power is proportional to Ω_E^2. Previous work also found that the friction losses can be approximated assuming a 2^{nd} order function in engine speed [14, 25]. It is assumed pumping force is proportional to velocity squared, similar to drag, so the pumping power is proportional to Ω_E^3.

The indicated thermal efficiency, η_T, has similar islands as the brake efficiency except at higher engine RPM. The mechanical efficiency, η_M, in Fig. 3.9 shows that losses are highest at high engine speed, especially at low torque. Conversely, highest mechanical efficiency is seen at low engine speed and high torque. While the mechanical efficiency is reasonable, the indicated thermal efficiency is fairly low. The maximum thermodynamic efficiency of an Otto cycle with a compression ratio of 5 is roughly 45%. The maximum attainable indicated thermal efficiency is expected to be about 30% [28], similar to the engine used in these experiments. Our values are near $20-22\%$. The additional losses are likely due to suboptimal operating temperature of the engine as well as tuning of the carburetor.

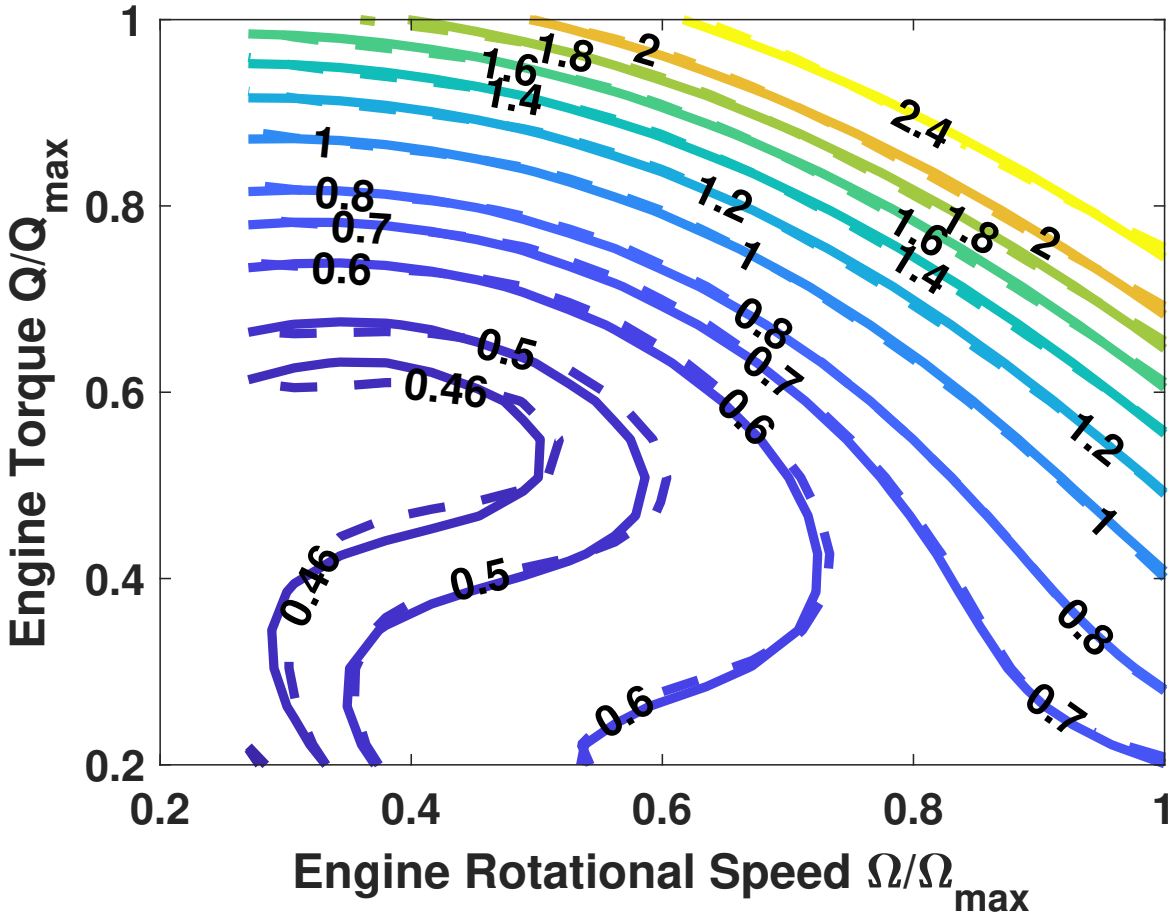


Figure 3.4: Final model. Contour of fuel mass flow rate. Agreement between predictions (dashed) and experiment (solid).

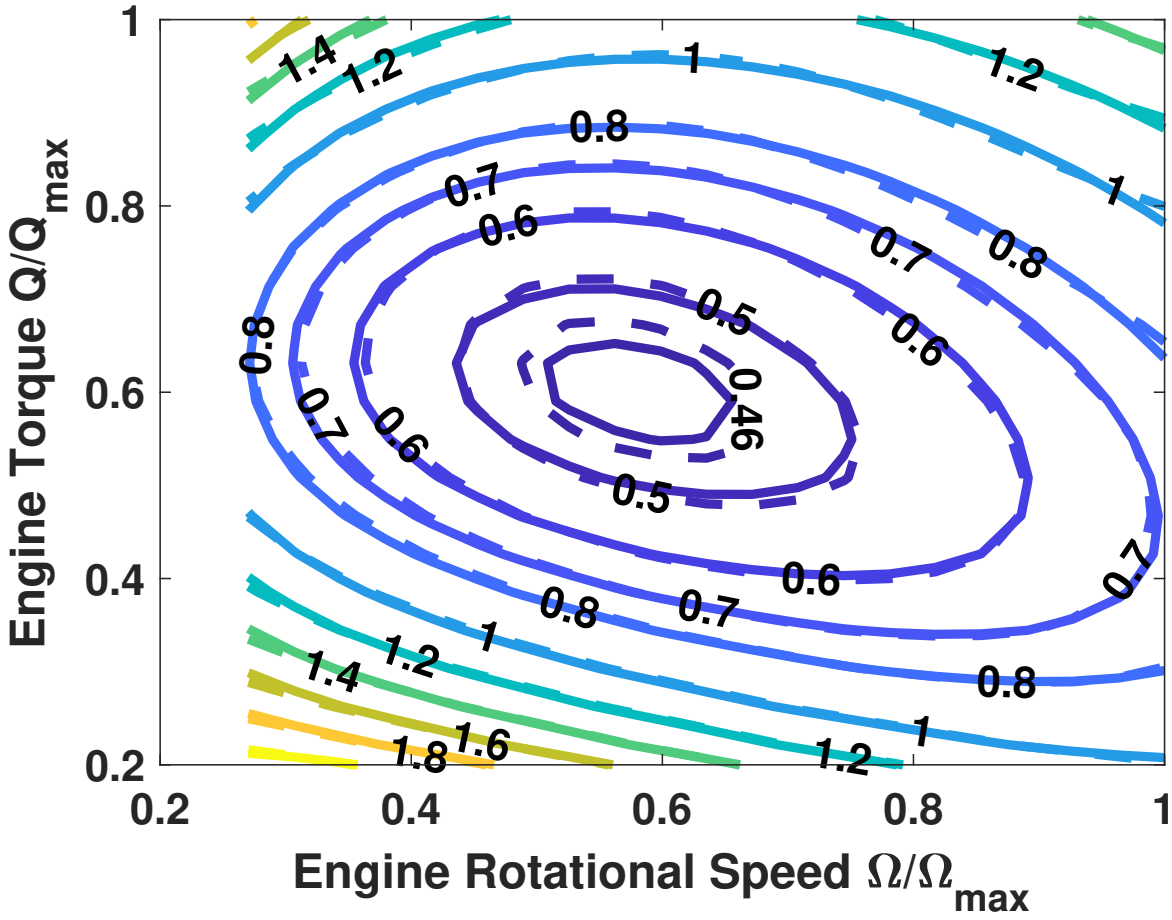


Figure 3.5: Final model. Contour of specific fuel consumption (SFC). Agreement between predictions (dashed) and experiment (solid).

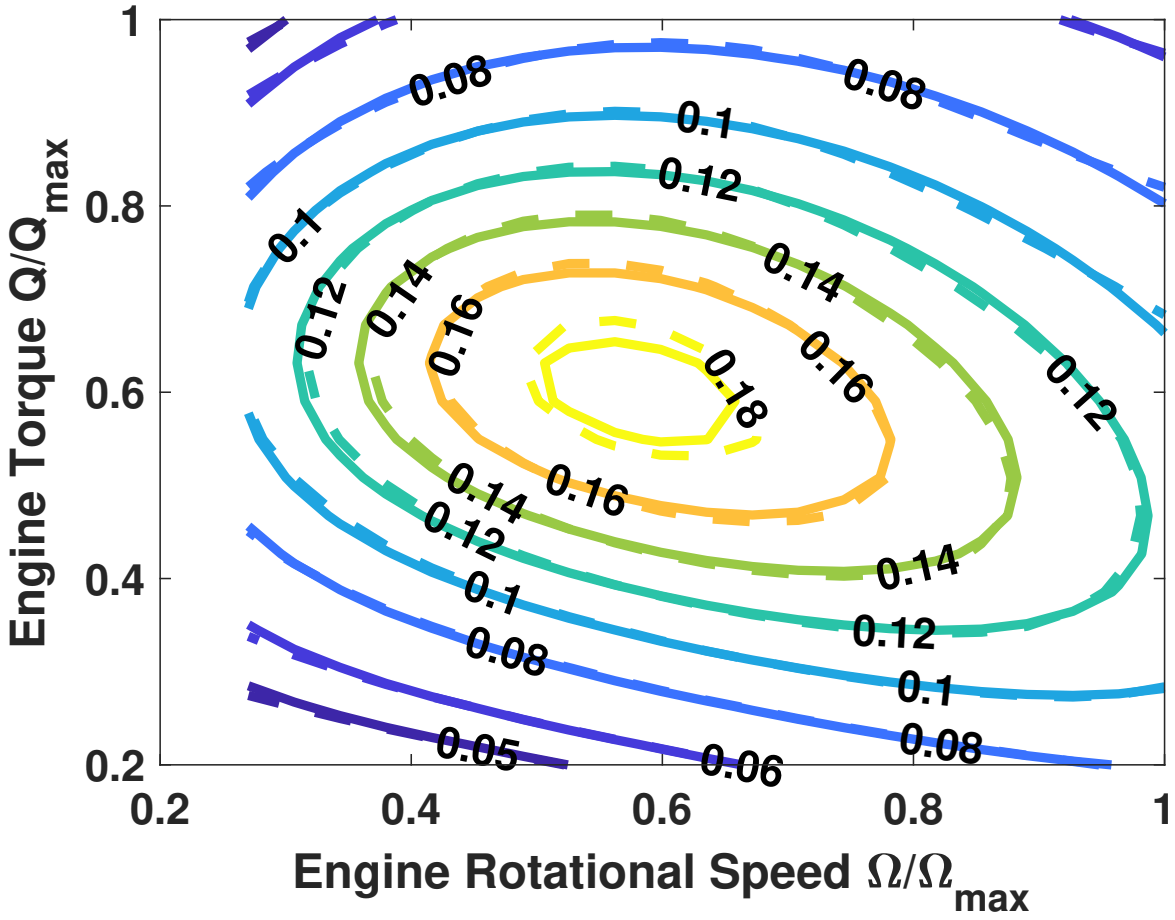


Figure 3.6: Final model. Contour of brake thermal efficiency η_B. Agreement between predictions (dashed) and experiment (solid).

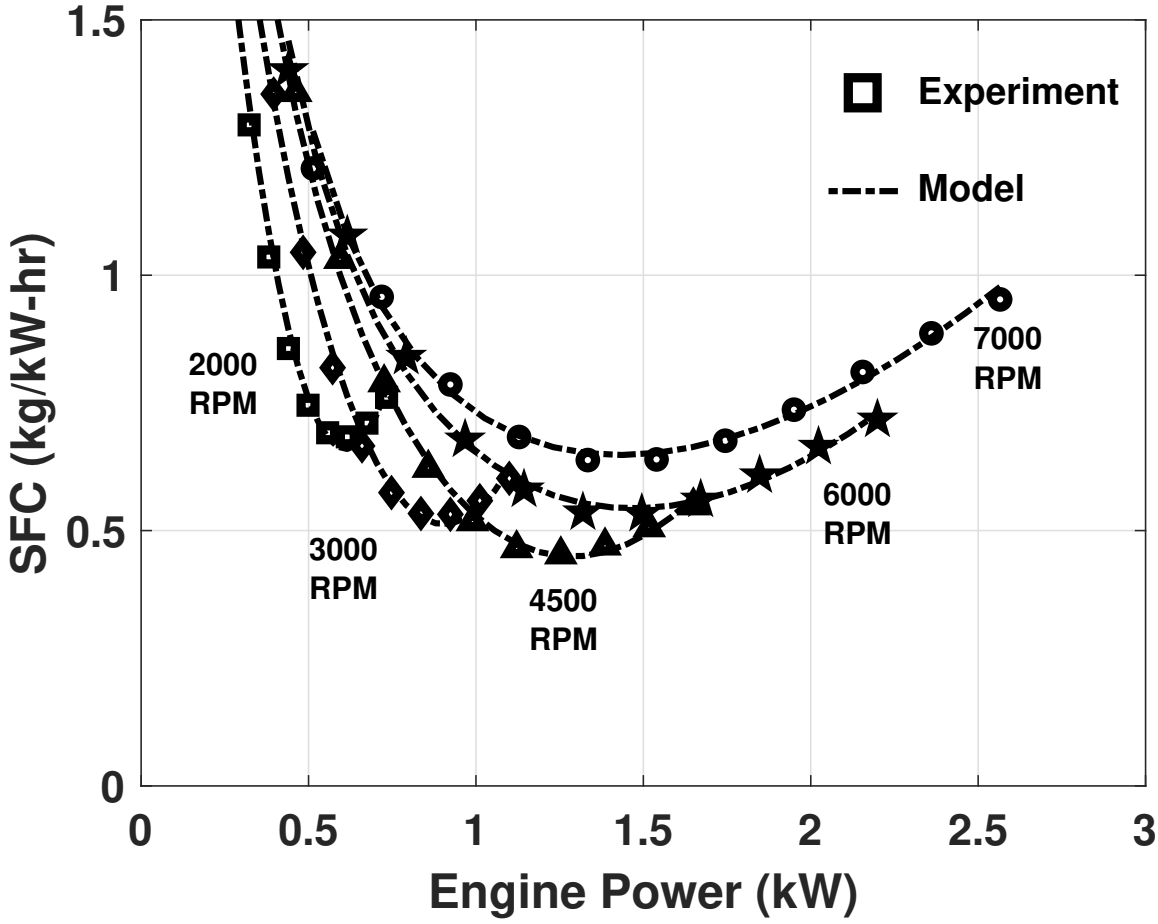


Figure 3.7: Final model. Engine SFC versus engine power.

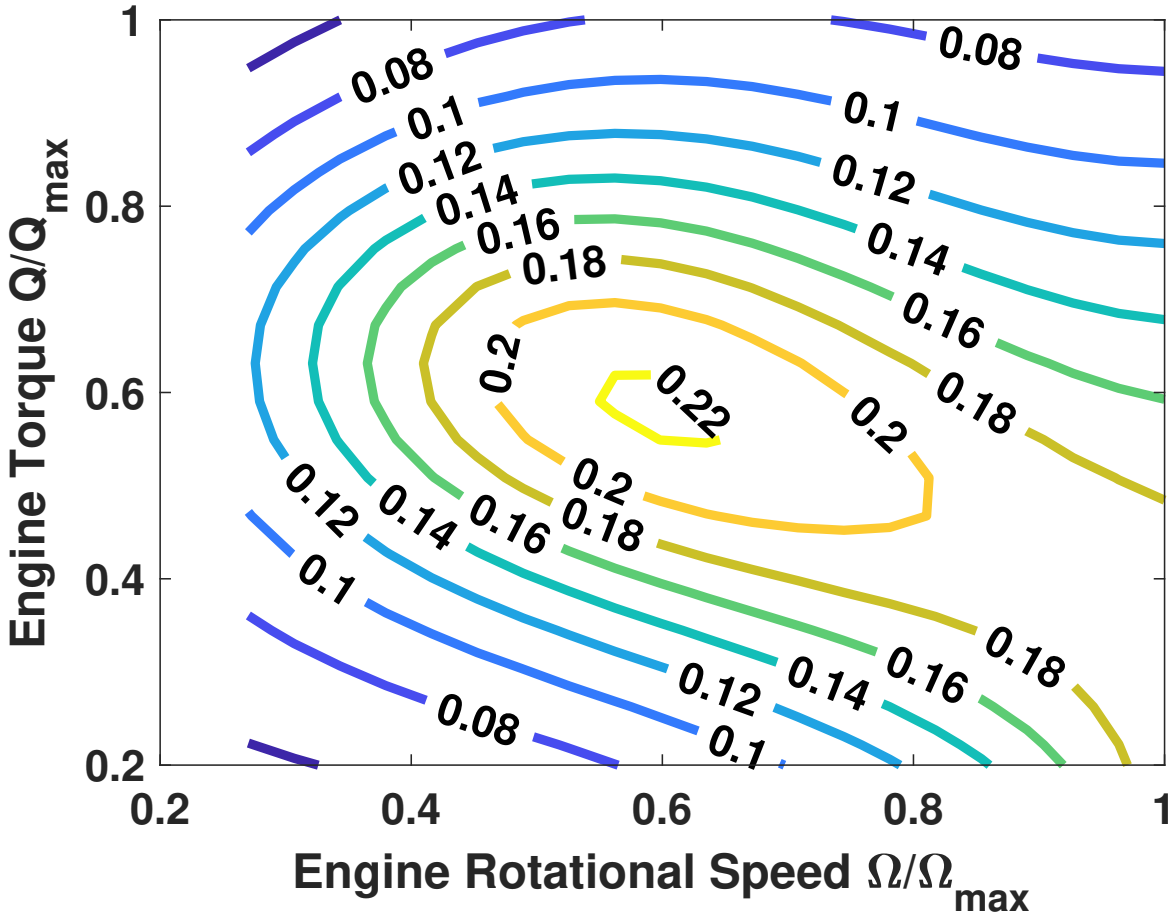


Figure 3.8: Contour of predicted indicated thermal efficiency η_T.

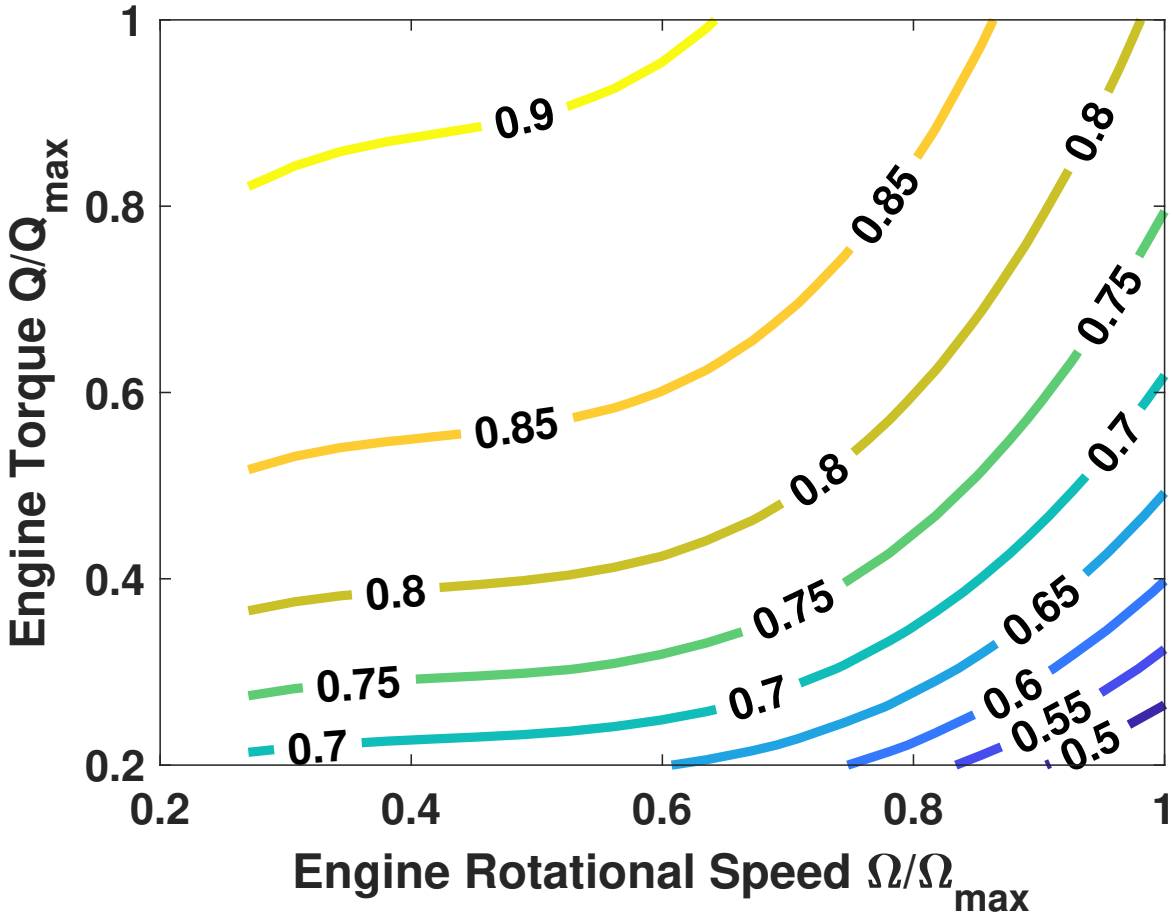


Figure 3.9: Contour of predicted mechanical efficiency η_M.

The carburetor needed to be tuned such that the engine could operate at the widest range of speed and torque possible. The high and low speed needles were fixed for the experiments thereby sacrificing performance at a specific operating condition.

3.5 Summary and Conclusions

This chapter detailed the the mathematical model developed to predict the fuel consumed of a 4-stroke engine. The model formulation, systematic build up, calibration, and resulting agreement were covered. The model parameters are non-dimensional for scalability. Based on this work, several key conclusions are drawn.

1. It is hard to model the SFC map due to high orders of nonlinearities in indicated thermal efficiency that vary up to third order in torque and engine speed.

2. A 3^{rd} order function in engine rotational speed can be used to approximate the pumping losses special in a 4-stroke piston-engine model.

The engine model is now ready to be integrated with an aircraft sizing analysis. Along with the qualitative understanding of component and system efficiencies, the impact of hybrid-electric power generation on aircraft design can now be realistically assessed.

Chapter 4: Rotorcraft Comprehensive Analysis

This chapter details the build up of analytical tools necessary to assess the performance and dynamics of an electric or hybrid-electric configuration. It covers simple analysis, detailed analysis, and a series of systematic validations.

4.1 Simple Rigid Blade Analysis

A simple rigid blade analysis is useful to calculate initial conditions for a detailed flexible blade analysis, for calibration of certain properties, and for a quick assessment of the impact of reducing tip speed. Tip speed reduction in forward flight is a key benefit of a distributed electric propulsion drivetrain and we will quantify why. In a simple model, blade flapping is rigid i.e. contains a single mode, inflow is uniform, there is no wake interaction between rotor and wing, and the wing has no flexibility. However, the rotor has a full set of C81 airfoil decks, so the airloads still capture Mach and stall effects. The full aircraft is trimmed for equilibrium so the aircraft attitudes, control angles, and power predictions are proper. This level of analysis is useful to calibrate properties such as aircraft drag by comparing with flight test data. Such properties are difficult to predict even with very high fidelity models.

The quantities we wish to accurately predict are aircraft attitude, specifically pitch, and the lift-to-drag ratio (L/D). The L/D is a universal metric of efficiency for aircraft. It is a non-dimensional

number representing the weight that can be carried for every unit of energy spent per distance traveled. More intuitively, it is the energy spent to carry unit weight over unit distance — turned upside down. So the less energy, the more L/D. The L/D is defined as

$$\frac{L}{D} = \frac{W}{P/V} = \frac{W\,V}{P} \tag{4.1}$$

The total power is P, energy per time, and the speed is V, distance per time. So P/V is energy per distance. The weight is W.

Propulsive trim is necessary to accurately predict the total power required in forward flight as both lift and drag are dependent on airspeed and attitude. The rotor orientation is fixed relative to the wing in forward flight. This creates a direct coupling between the rotor and wing which requires numerical iteration to achieve propulsive trim. The total power is found by calculating the individual components of it.

$$P = P_i + P_o + P_p \tag{4.2}$$

The induced power, P_i, represents the power required to generate lift. The profile power, P_o, represents the power required to overcome the profile drag of the rotor blades. The parasite power, P_p, represents the power required to overcome the drag of the rest of the aircraft. Drag varies with speed, U, and is approximated using the typical formula, $D = \frac{1}{2}\,\rho\,U^2\,f$, where ρ is air density, and f is the aircraft flat plate area. The flat plate area, also called drag area, is then the total drag divided by dynamic pressure, $q = 1/2\,\rho\,U^2$. A regression model is developed from historical data on measured full-scale helicopter and aircraft drag [29] so we can predict the drag at this stage of design. The formula is,

$$f = k \left(\frac{W}{1000} \right)^{2/3}. \tag{4.3}$$

The variable k is referred to as the Harris factor after Frank Harris who proposed this regression model. Weight is input in lbs, the factor is non-dimensional, and flat plate area is returned in square feet.

The simple analysis is first validated with the XV-15. The XV-15 was a heavily studied research tiltrotor and provided a wealth of flight test data, creating a good foundation to ground this analysis to. Despite being a much larger aircraft, with a design gross weight of 13,000 lb relative to the 50 lb aircraft, the configuration itself is similar, consisting of multiple rotors mounted on wings. In fact, it is the only aircraft consisting of a rotor mounted on a wing for which flight test data is available. For the XV-15, the Harris factor is calibrated to be $k = 0.9361$. This does not include the profile drag from the wings which comes from the airfoil decks. With parasite drag calibrated, the impact of tip speed reduction in forward flight can be studied.

The analysis requires two trim variables, lift and drag, and two controls, rotor collective and body pitch angle. The same collective is applied to both rotors. The flight speed is swept from 100 knots to 250 knots. The results are shown in Fig. 4.1 and Fig. 4.2. The test data collected was at a rotational speed of 91% nominal rotor speed (NR). Decent agreement is seen between the predictions and test data. Thus, the simple analysis is considered validated.

A key benefit of electric propulsion is the ability to reduce the rotor RPM in axial flight. Reducing the rotor RPM has the potential to unlock significant gains in L/D, also shown in Fig. 4.1. This is based on a simple principle that is illustrated in Fig. 4.3. Rotors are designed to be highly efficient in hover, which typically has the highest power requirement. In hover, rotor force equals weight. When

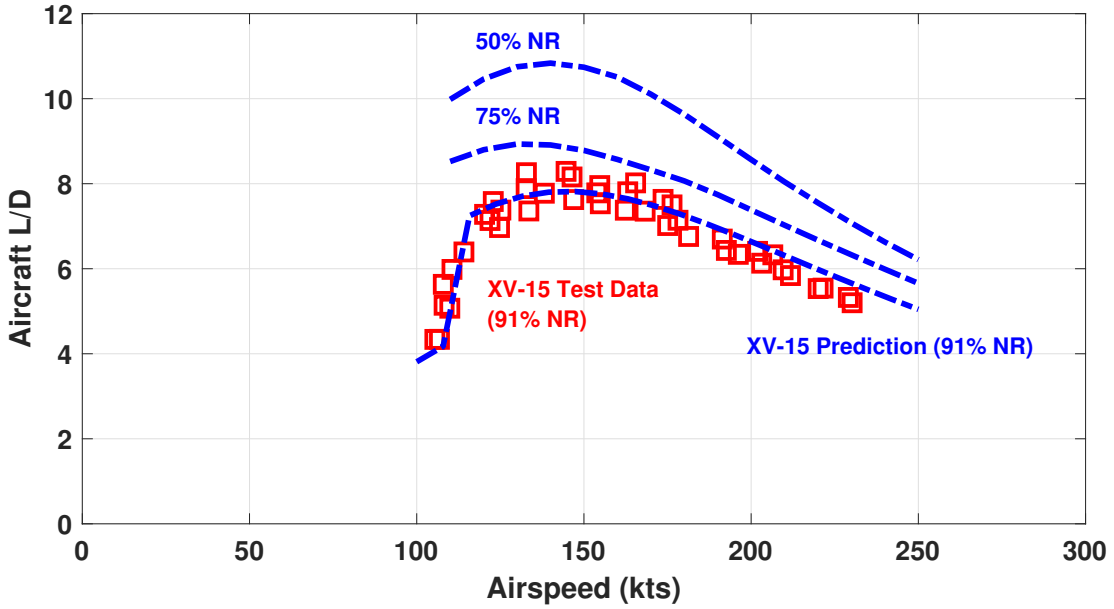


Figure 4.1: Prediction of L/D for the XV-15 (lines) versus measured (markers).

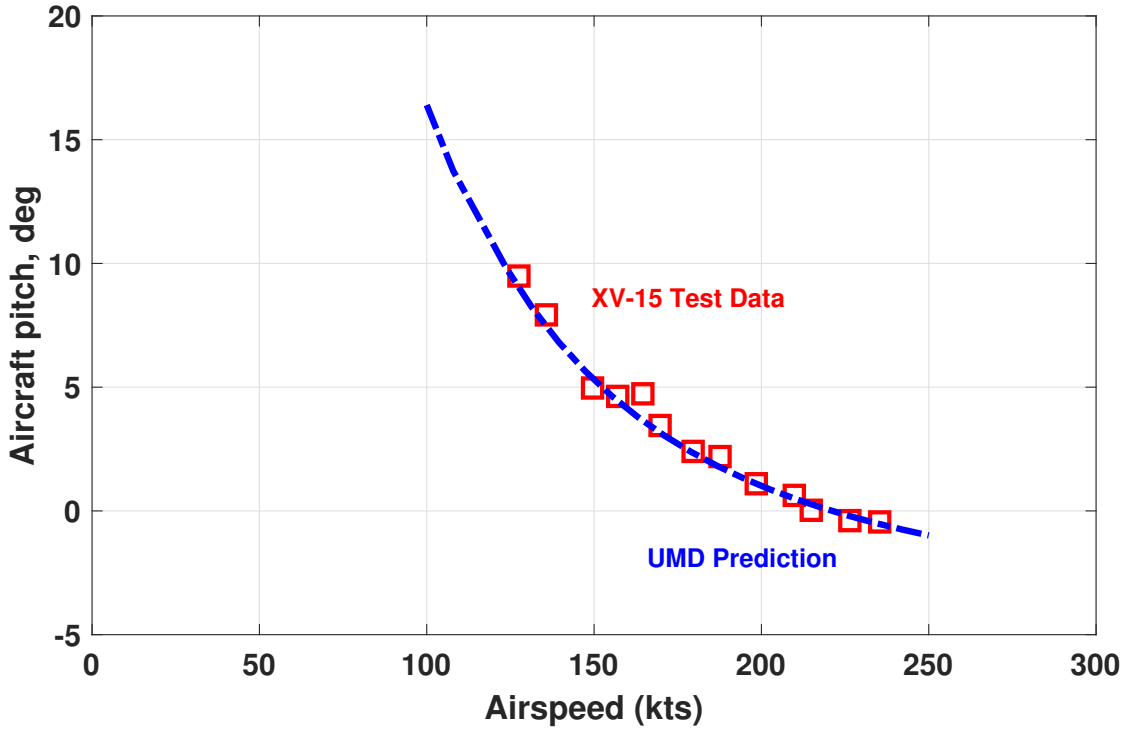


Figure 4.2: Prediction of XV-15 trim pitch attitude (lines) versus measured (markers) at 91% NR. Positive nose-up.

the rotor turns forward in cruise, force equals drag, which is almost an order of magnitude lower than weight. The lift generated by an airfoil section, which produces the rotor thrust, is proportional to the square of airspeed U^2 and angle of attack α. At the same RPM in cruise, angle of attack must drop to lower lift, forcing the airfoils to operate in an inefficient c_l/c_d range. If the RPM can be reduced, U^2 is reduced, and the blades can operate at higher angles of attack, in a more efficient c_l/c_d range.

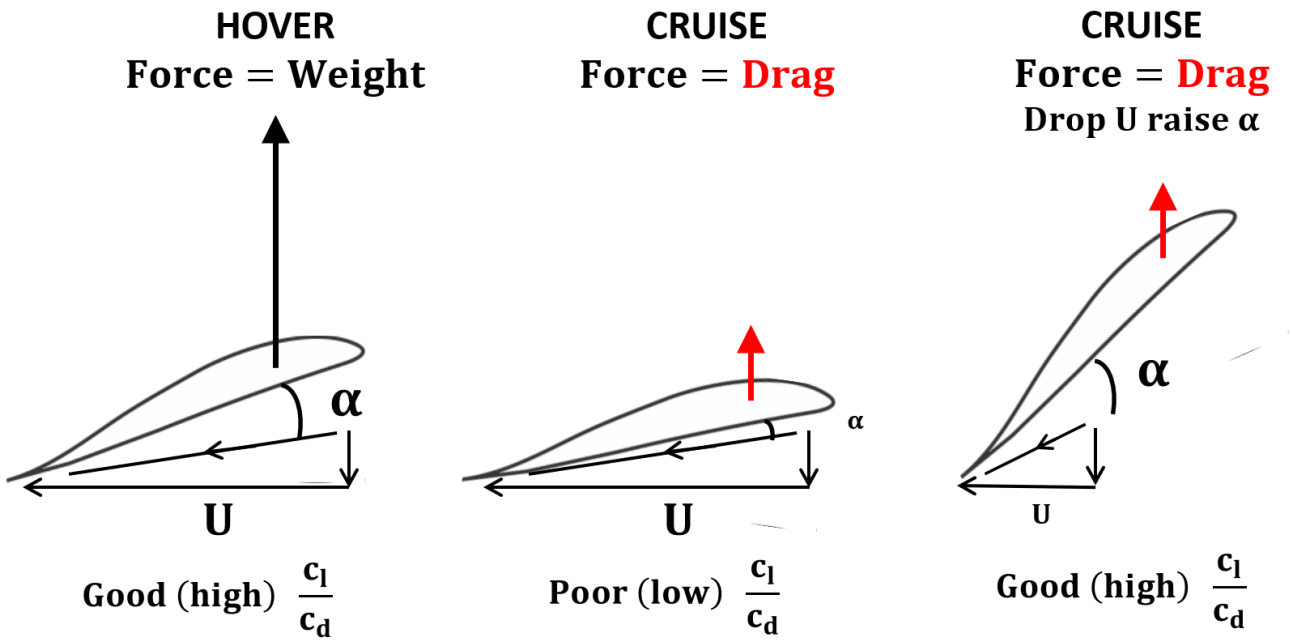


Figure 4.3: Impact of RPM reduction in axial flight on airfoil section c_l/c_d.

The anticipated gain in L/D of the XV-15 as the rotor RPM drops to 50% NR is seen in Fig. 4.1. The XV-15 was not able to operate at these rotor speeds, due to rotor and drivetrain dynamic instability, so no test data was collected. The question now is, do these trends hold at small scale with low Reynold number effects?

We now model the 50 lb aircraft using the simple analysis. This vehicle has four rotors and two full wings. This can be modeled as four rotor-wing pairs. The complexity is reduced by modeling two rotor-wing pairs, one counter-clockwise and one clockwise, much like the XV-15. The lift required is fixed. Half of the configuration is modeled, therefore the lift target is 25 lb. The thrust requirement

is calculated as before based on airspeed and an assumed Harris factor. In 2018, NASA conducted a conceptual design study where they sized an all-electric quadrotor [30]. The drag build-up resulted in a Harris factor around 3 for each variation of the configuration. The drag profile of the aircraft is expected to be closer to the electric quadrotor than the XV-15, so a conservative Harris factor of 3 is chosen for this analysis.

The L/D predictions for the 50 lb aircraft are shown in Fig. 4.4. The actual value of L/D is much lower than the XV-15, along with the flight speed for best range. Recall the XV-15 gross weight is 13,000 lbs and the quad biplane is 50 lb. Despite the small scale and increased drag, the same principle and trends with decreasing tip speed appear to hold.

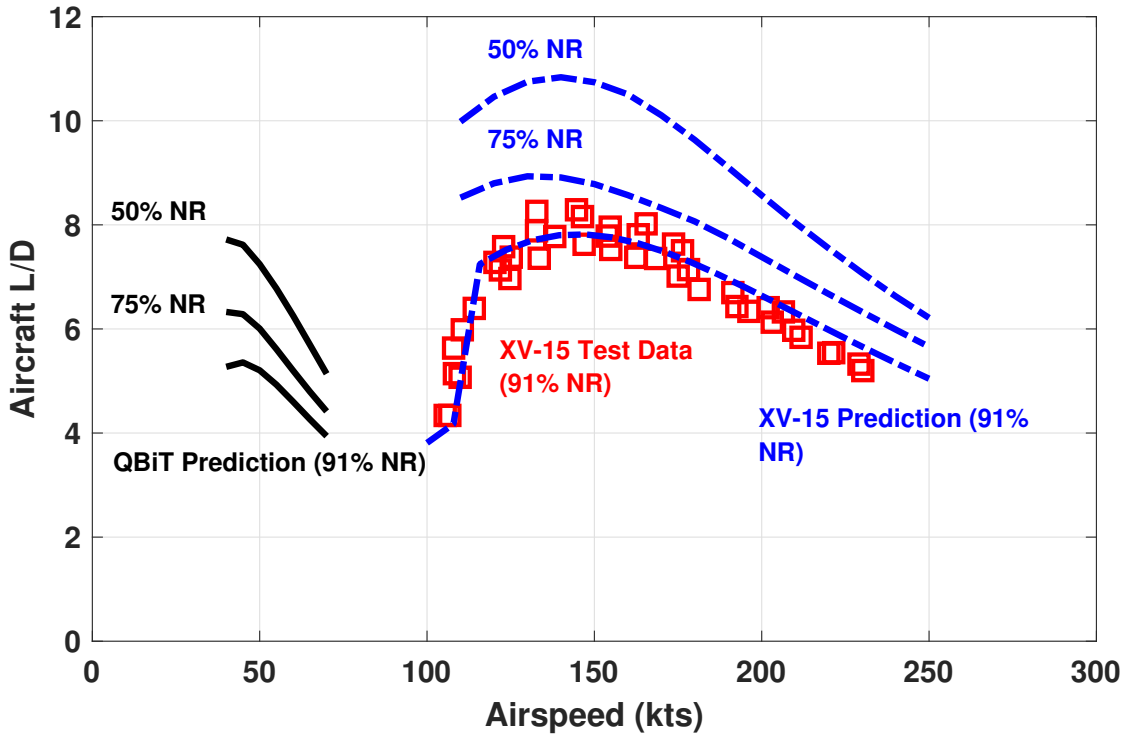


Figure 4.4: Predicted lift-to-drag ratio of QBiT relative to the XV-15.

There is very little evidence on what the correct value of aircraft L/D should be at a small scale. An 8 lb quad biplane was built and flown at UMD in the past. Power was measured to be 200 W at

a speed of 8 m/s (15 knots) which gave an L/D of 1.5. But the aircraft was flying at a 30°-40° pitch angle, far from airplane mode, almost in helicopter mode, and the rotor speed was not reduced at all. This research was never published.

More recently, an 80 lb quad biplane was analyzed with CFD [21] at a higher speed and pitch of 8° and they claimed an L/D of around 4. Thus, there is no consistent literature on the topic. The predictions here of L/D around 4 in airplane mode thus appear reasonable.

Do the trends hold when there is wake interaction? What is the impact of rotor flexibility? What is the impact of wing flexibility, when the rotor is offloaded and the aircraft is entirely wing borne? Does L/D change and in what way? There is no available test data to obtain answers to these questions. We can, however, begin to explore them using higher fidelity analysis. In order to answer these questions, we move on to comprehensive analysis.

4.2 Comprehensive Analysis

A comprehensive analysis of a hybrid-element rotorcraft must model its special characteristics. Some of the important ones are the following.

1. Short, highly twisted blades for which no small angle/helicopter mode assumption is acceptable,
2. Rotors mounted on lifting and/or non-lifting structures,
3. Multiple rotors and wings inflow for interactions,
4. Unconventional trim variable such as all collective or all rotor speed.

The baseline comprehensive analysis, University of Maryland Advanced Rotorcraft Code II (UMARC-II) is expanded to support these unique elements with careful validation of each.

UMARC-II is built on the foundation of Hodges-Dowell theory with Ormiston's pseudo coordinates integrated with multi-body dynamics as developed by Gul [31]. As with any comprehensive analysis, UMARC-II models structures and aerodynamics with equal texture/level of fidelity. Rotating- and fixed-wing can both be modeled with dynamic and aerodynamic interactions. The level of fidelity is low – structures as beams with cross-sectional properties and airloads with lifting-line and cross-sectional/airfoil properties.

4.2.1 Structural Model

The structure is modeled as a series of Hodges-Dowell/Ormiston beams that may deform in flap, lag, torsion, and extension and are connected by multibody joints. The Euler-Bernoulli assumption is made such that the cross-section itself does not deform. The formulation follows Hamilton's Principle with finite element discretization to obtain the governing equations. Aerodynamic and inertial forcing is determined. Deformations are converged to satisfy the governing equations.

The baseline UMARC-II was limited to modeling one flexible rotor mounted to one flexible wing. This dissertation expands UMARC-II to model multiple rotors and wings in the same simulation. The foundation for connectivity of the elements is written such that overhauling the formulation would be a PhD thesis on its own. Thus, the maximum number of rotors that can be structurally coupled to a wing is still one and all of the rotor-wing pairs are fixed at their respective wing root, so there are no rigid body modes (can be changed) nor any structural coupling between one rotor-wing pair to another. But any number of rotor-wing pairs can now be modeled, laying the groundwork to model dissimilar rotors and wings at once.

4.2.2 Aerodynamic Model

The foundation to obtain the aerodynamic forcing is lifting-line with unsteady thin airfoil theory. Improvements have previously been made to better resolve the bound circulation, lift, and tip loss of the blades using Weissinger-L type near wake, and to propagate vortex trailers in time and space, using free wake [31, 32].

The lifting surfaces are discretized with aerodynamic panels and the wake with filaments. The new transient Maryland Free Wake of Shastry [32] which is based on time, not azimuth, was integrated to allow unequal rotor speeds and transient variations. Initially, the time step for propagation of the wake is input as an azimuth step, $\Delta\psi$, but Δt is determined from the highest rotation speed of the rotors, if there are several. The wake markers are propagated in space at each time step and the Biot-Savart Law is used to resolve the induced velocity at the lifting surface.

The formulation of the time marching freewake itself already supports multiple lifting components. UMARC-II, however, needed to be modified in a general sense to ensure the appropriate induced velocity was assigned to each Gaussian point on each structure for the downstream computations. The core functionality only supported free wake for a single rotor with no wing, as shown in Fig. 4.5. Note that near wake computations were included, albeit fixes were made to the implementation of theory, but visualization was not.

The free wake interface in UMARC-II was systematically built up. First, one wing was included, shown in Fig. 4.6. Next, the components were duplicated and oriented on the left-hand-side of the model, shown in Fig. 4.7. Finally, modifications were made to initialize any number of rotor-wing pairs in any location. Additionally, it is now possible to define any number and location of vortex trailers for each structure individually. If one rotor is expected to generate two vortex trailers per blade

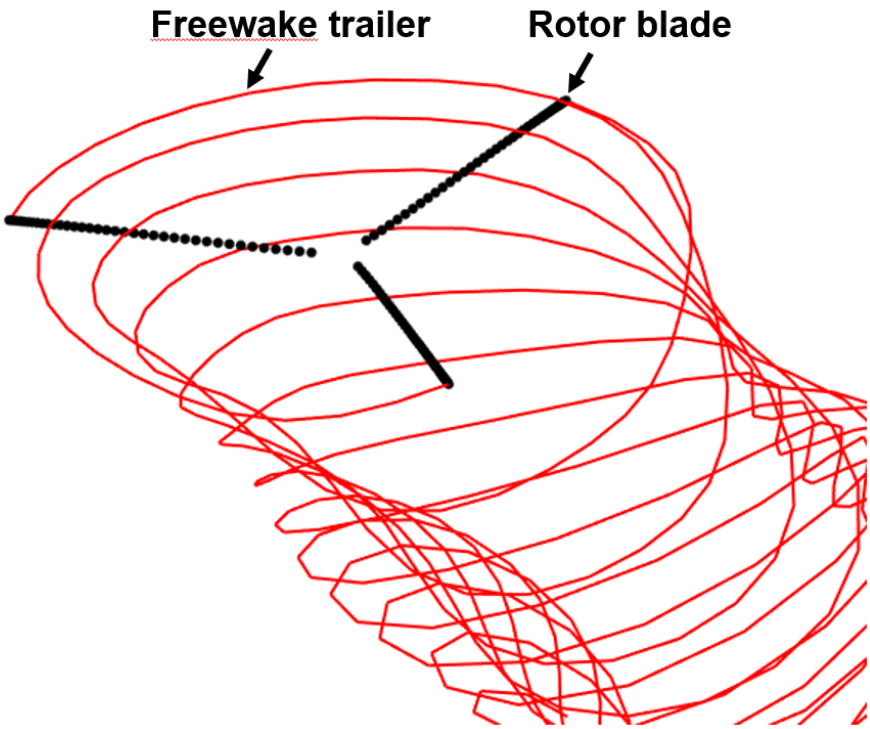


Figure 4.5: Baseline: a single rotor with one free wake tip trailer per blade

and another is expected to generate one, this can be modeled. The wing wake is generally modeled as a rolled up tip vortex. An illustration of this can be seen in Fig. 4.8.

Now, when used with free wake, the bound circulation and vortex trailers from all of the rotors and wings impact one another. This forcing makes its way into the loads which we will see later. So, despite the rotor-wing pairs remaining structurally uncoupled, they are all coupled aerodynamically.

4.2.3 Trim Solution

The trim procedure is standard. It finds the controls and aricraft attitudes for equilibrium in steady level flight. A jacobian is determined that stores the sensitivity of the trim targets to the trim controls. Once the hub forces and moments are resolved, residuals of the appropriate values to the targets are determined. The residuals are then used to update the trim controls to drive the targets to

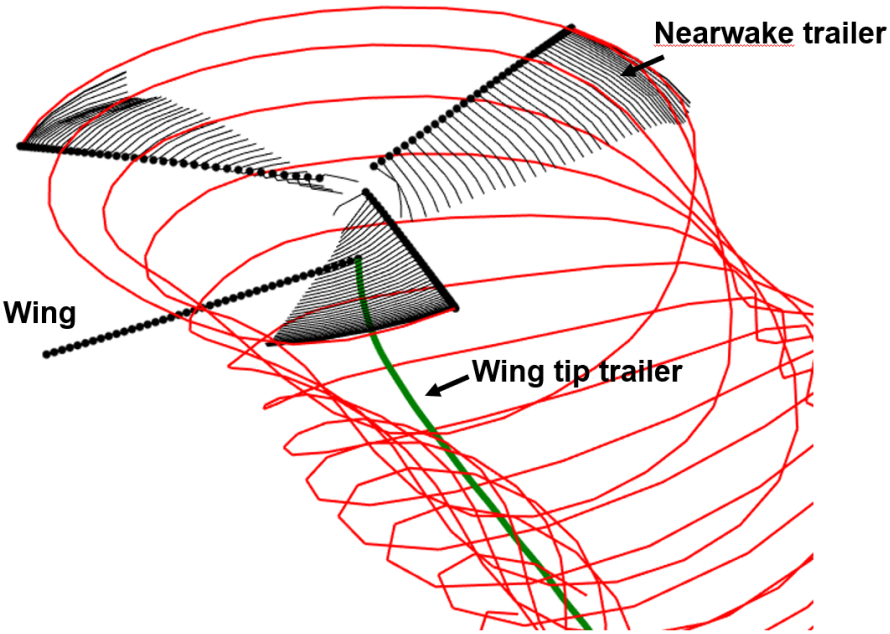


Figure 4.6: Refinement 1: One rotor with nearwake trailers, one tip trailer per blade, and one wing with one tip trailer.

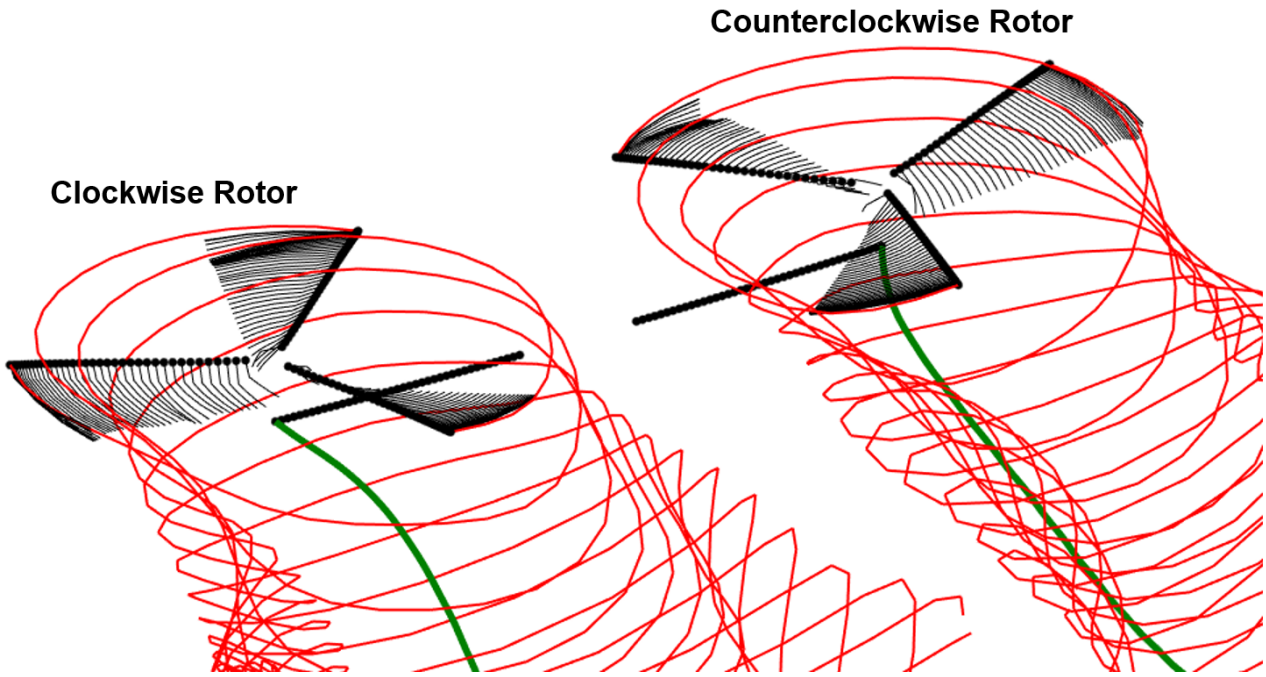


Figure 4.7: Refinement 2: Two rotors with nearwake trailers and one tip trailer per blade, and two wings with one tip trailer each.

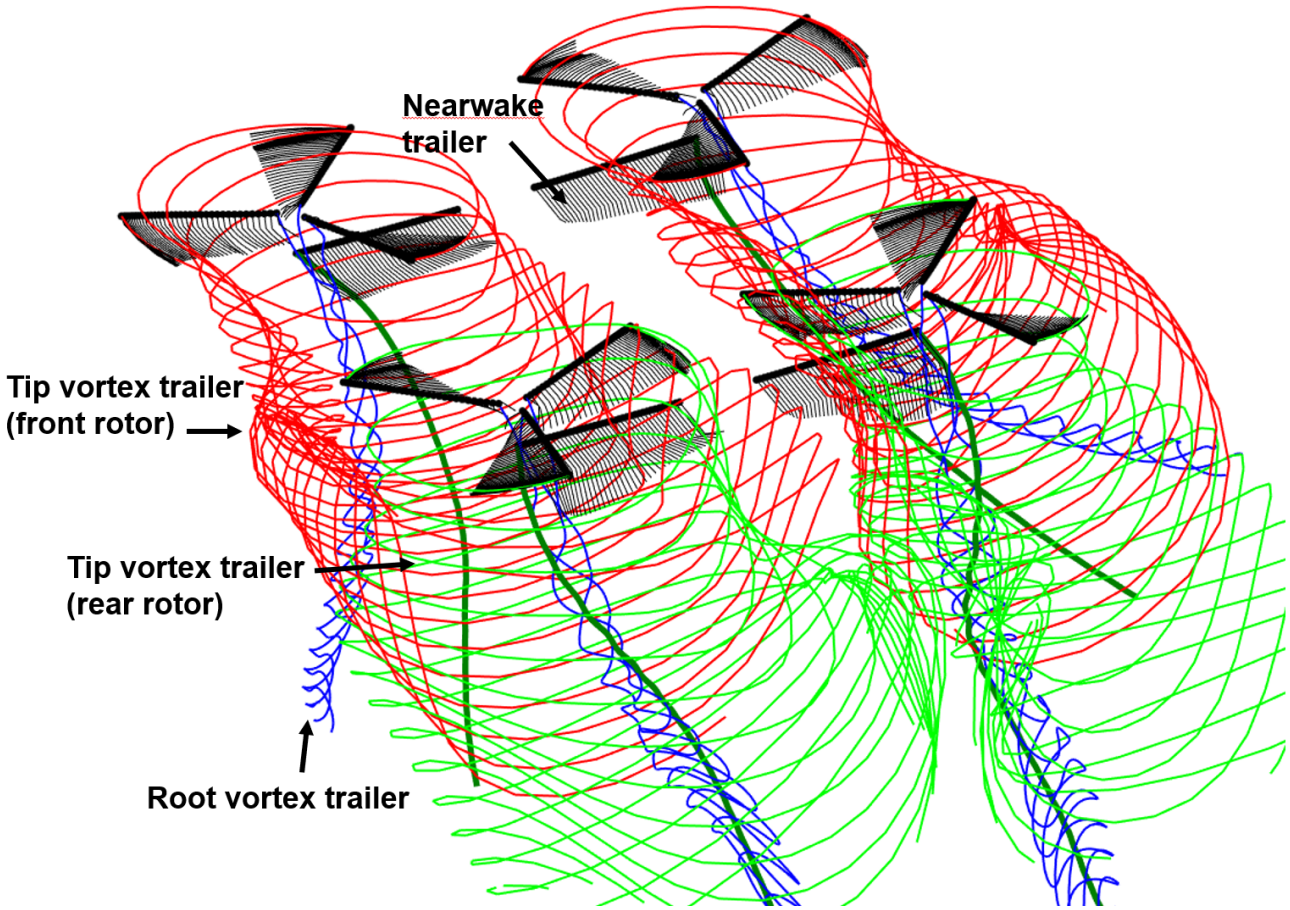


Figure 4.8: Refinement 3 (final): Four rotors with nearwake trailers, a tip trailer and root trailer per blade, and four wings with nearwake trailers and one tip trailer each.

convergence.

The baseline UMARC-II was capable of trimming only one rotor. UMARC-II has been expanded through this work to allow for any number of rotors and wings. Specific changes per rotor or per wing can be added in the inputs and the source code after duplication of the components, so the rotors and wings can all be different. This allows for each rotor to rotate at a different RPM, if desired, which is needed for RPM controlled multi-rotor aircraft. Additionally, it is now possible to provide trim targets in the inertial frame.

In summary, UMARC-II is now capable of coupling the aerodynamics of a multi-rotor, multi-wing configuration through freewake. Propulsive trim cases can be configured for any number of rotors, wings, and trailers. Individual rotor RPM can be initialized if desired. Now, the capabilities must be validated and verified to the fullest extent possible.

4.3 Validation

There are no publicly available test data for hybrid-electric or even all-electric rotorcraft to validate any of the elements identified. Therefore, a systematic approach is taken to validate piecewise performance and loads predictions based on data from conventional rotors that is publicly available.

High-twist hover power is validated with wind tunnel test data of the Boeing Model 222 (M222) and the Maryland Tiltrotor Rig (MTR). Loads predictions are validated using wind tunnel test data of the M222 [33]. Though not electric, these are twisted rotors with a hingeless hub, typical of what is expected on electric rotorcraft. They also cover both scales — full-scale and model-scale — and a broad range of tip Mach numbers. No data is available for a rotor on a boom. While the MTR rotor was mounted on a wing, the wing was pressure instrumented to actually measure the lift. Therefore,

predictions are compared to previously validated analysis of the M222 isolated rotor. Likewise, data is not available for a multi-rotor, multi-wing configuration. Therefore, the quad biplane is modeled using the previously validated analysis. Performance is predicted for half of the aircraft, i.e. two rotor-wing pairs, and compared to predictions of a single rotor-wing pair.

4.3.1 Hover Power

The MTR, shown in Fig. 4.9, is loosely based on a 1/5 Froude scale model of the XV-15. Details of the model can be found in Ref. [34]. The rotor has a radius of 2.375 ft, aspect ratio of about 6.7, and twist of -37°/span, making it a good candidate to analyze short, highly twisted blades. The data used was collected by setting the collective, θ_{75}, and measuring thrust and power.

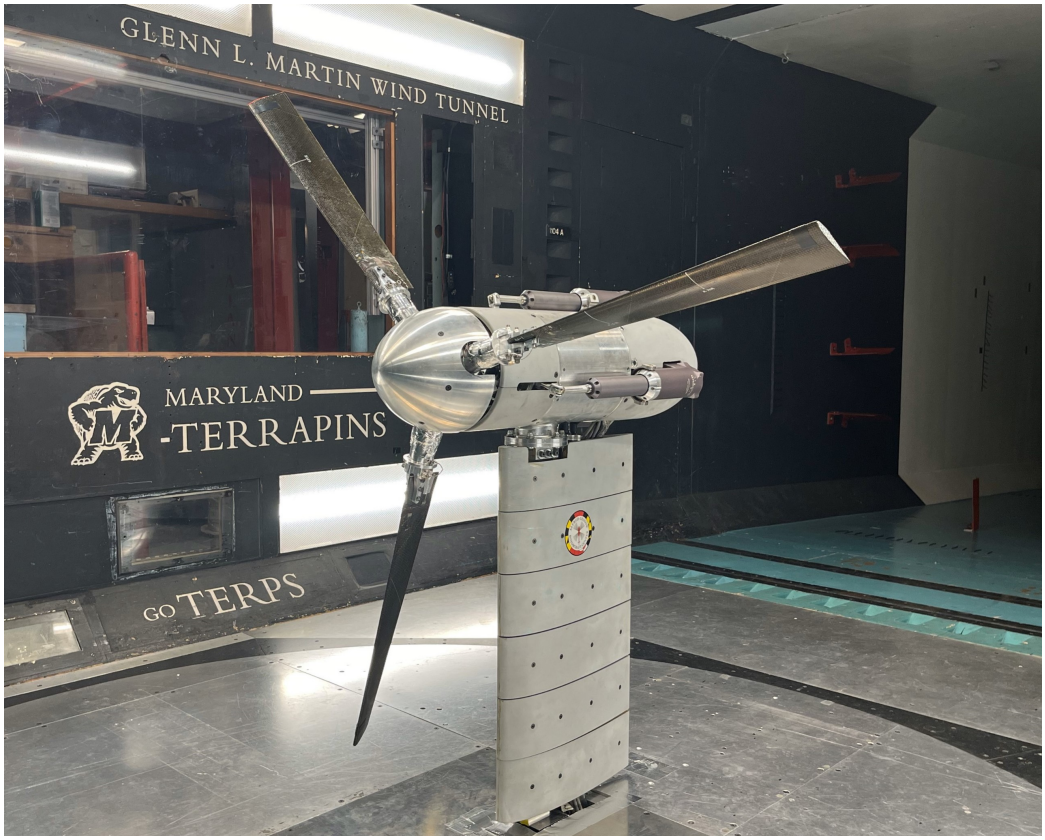


Figure 4.9: The MTR in the Glenn L. Martin wind tunnel.

To model this rotor in UMARC-II, the geometry and structural properties are input as 18 finite elements. The blades are uniform. A single airfoil, VR7, defines the blade profile. The MTR being a Froude scale model results in a low tip Mach number, between 0.2 and 0.3 and low tip Reynolds number, about 400,000. Refined C81 airfoil decks are used in the analysis generated at a Reynolds number of 300,000 with higher resolution at lower Mach numbers covering 0.01, 0.05, 0.1, 0.15, and 0.2. The C81 tables were calculated using in house 2D CFD TURNS2D [35]. The higher resolution table improved prediction considerably.

The collective is set based on the test case, from 2°-30°, and the total inflow is iterated on to convergence. In the wind tunnel there was a natural recirculation of the flow with increasing thrust. This tunnel speed was measured during the tests and is necessary to insert into the analysis as a forward speed. Essentially, the rotor is operating in slight axial flow that increases with thrust.

It has been observed in Ref. [36] that for highly twisted blades, the vortex sheet rolls up near the root as well as the tip, resulting in a visible root vortex. The tip and root vortices both impact hover performance and must be modeled. The strength and direction of rotation of the tip vortex varies with thrust. Free wake is used to model the vortices. The root vortex will naturally circulate opposite the tip vortex. This is specified in the source code. As a note, any vortex that wishes to be modeled along the blade would have a strength equal to the difference in bound circulation of the directly adjacent panels.

The tip vortex strength is assumed to be 70% of the maximum bound circulation. The same factor is also used for root vortex strength for consistency. The wake geometry of a high thrust case is shown in Fig. 4.10. The wake does not contract as much as hover because of the tunnel recirculation. Additional analysis is done to obtain the classical contraction in pure hover, shown in Fig. 4.11.

Figure 4.12 shows thrust coefficient against collective. The predictions, lines, follow the data,

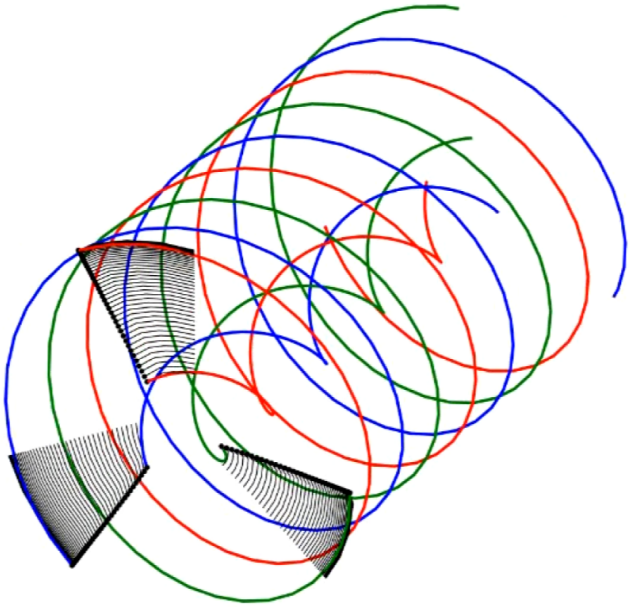


Figure 4.10: Wake geometry in hover with a tip trailer and root trailer. Wind tunnel test flight condition with tunnel recirculation.

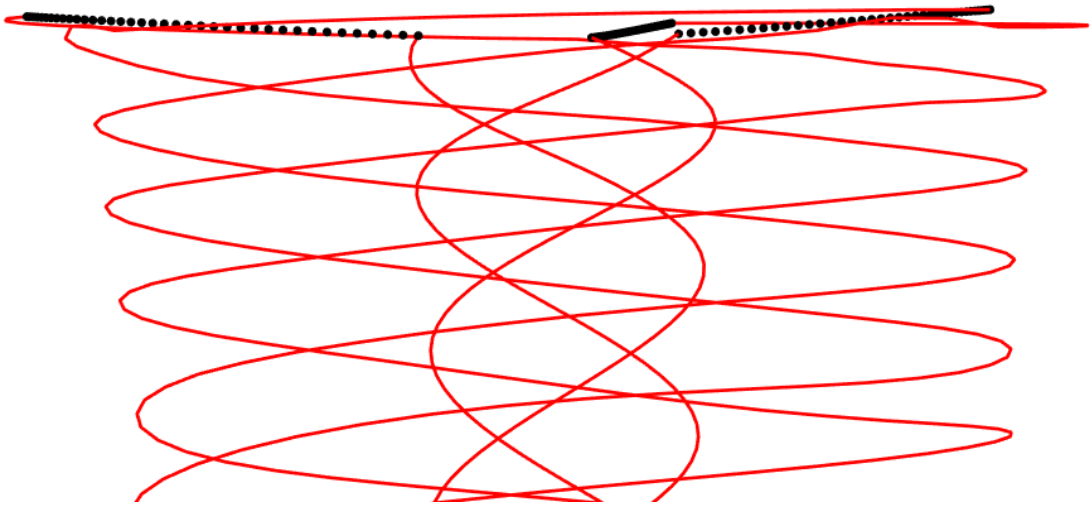


Figure 4.11: Wake geometry in pure hover with a tip trailer and root trailer.

markers, well. The different marker shapes are associated with different sets of collective sweeps. The stall regime is typically very difficult to capture at high collective, yet the analysis predicts an appropriate reduction in thrust. The higher resolution tables were crucial here.

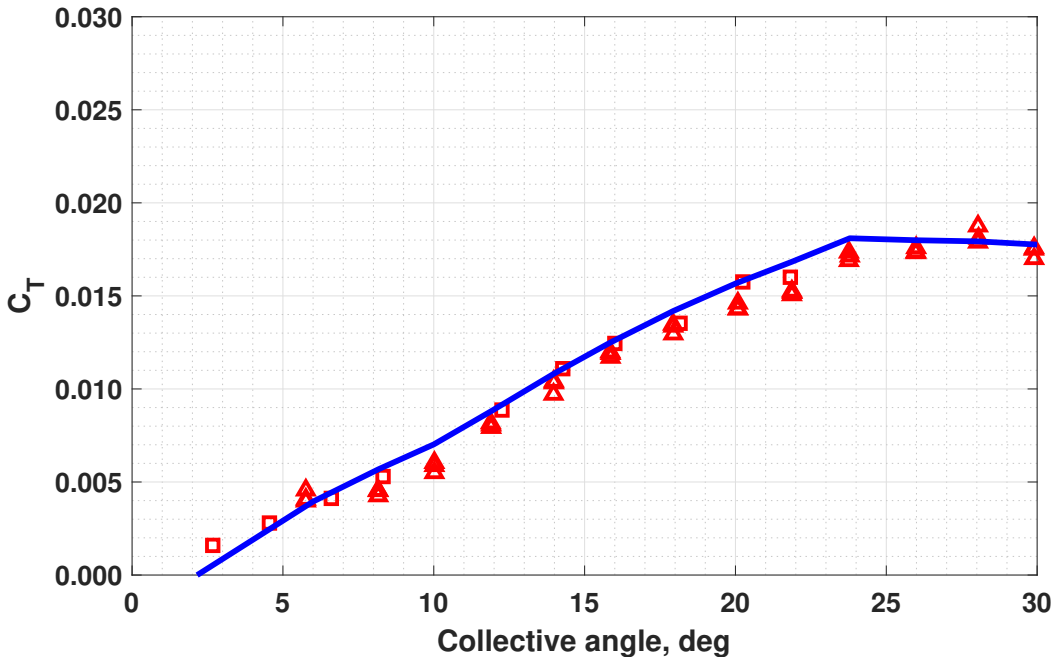


Figure 4.12: Measured thrust (markers) compared with UMARC-II predictions (lines).

Figure 4.13 shows power coefficient against collective. The predictions again follow the data well. Power is slightly overpredicted between 20 and 25 degrees collective. Note that no ad hoc profile drag corrections were needed and no additional low Reynolds number corrections are used, so the airfoil decks are quite accurate.

Figure 4.14 shows power coefficient against thrust coefficient. This is a common comparison because it takes the collective out of the picture which is typically prone to measurement errors. The predictions match the data near exactly.

Figure 4.15 shows Figure of Merit (FM*), which is a metric of hover efficiency corrected to account for slight axial flow. It is given by the following equation.

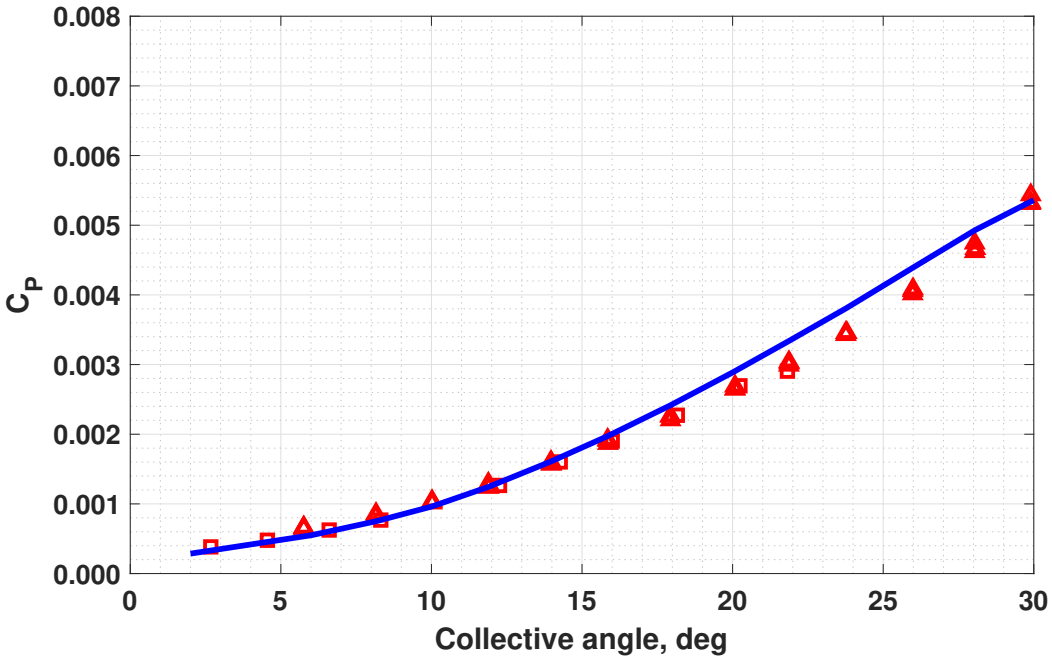


Figure 4.13: Measured power (markers) compared with UMARC-II predictions (lines).

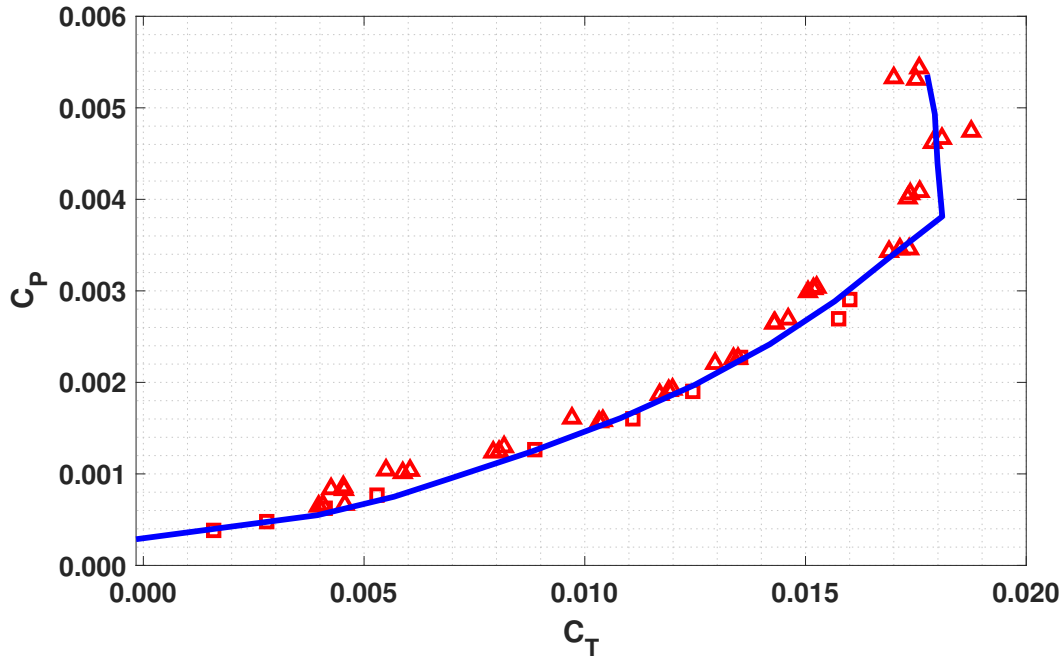


Figure 4.14: Two load cell measurements - thrust and power. Measured (markers) compared with UMARC-II predictions (lines).

$$FM^* = \frac{C_T\left(\lambda_i + \lambda_c\right)}{C_P} = \frac{C_T\left(\frac{\lambda_c}{2} + \sqrt{(\frac{\lambda_c}{2})^2 + \frac{C_T}{2}}\right)}{C_P} \tag{4.4}$$

The climb inflow, λ_c, represents the inflow component due to forward speed, in this case the tunnel speed. Good agreement is seen at high thrust, over 15°. At lower thrust, the experimental data deviation is likely due to errors in wind tunnel λ_c data as it is inconsistent with the good prediction of power and thrust in Fig. 4.14.

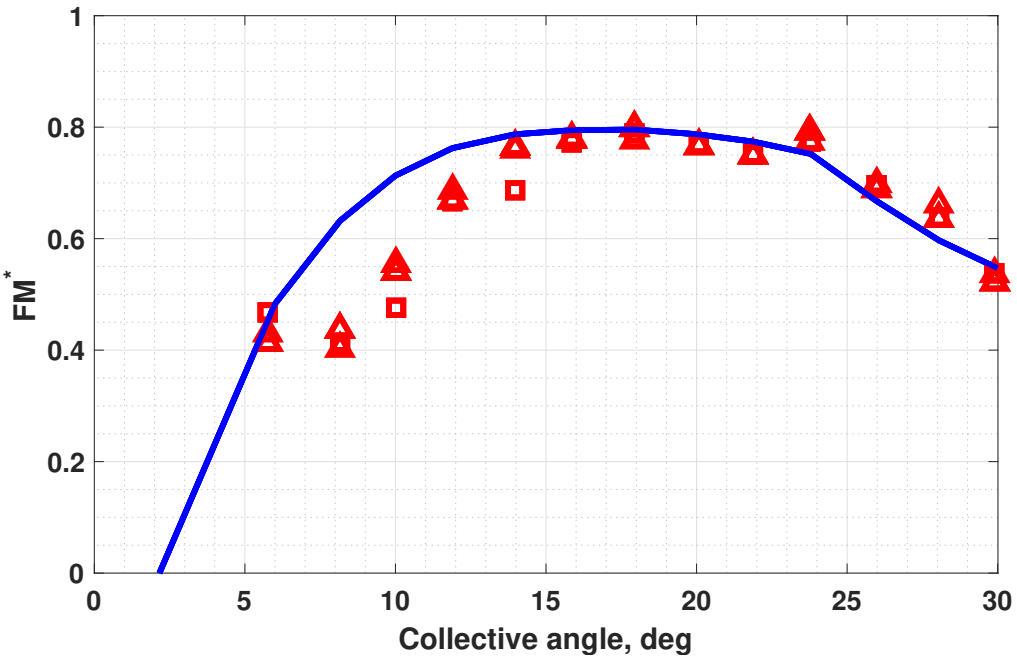


Figure 4.15: Measured (markers) compared with UMARC-II predictions (lines).

4.3.2 Cruise Power

Cruise power is validated with data from the M222 tests. The M222 was a soft in-plane hingeless hub tiltrotor research aircraft proposed by Boeing in the 1970s. A 26-ft diameter rotor half-wing configuration underwent rigorous wind tunnel testing in the 40 ft × 80 ft wind tunnel at NASA Ames

research center. A wealth of data on performance and loads in hover, transition, and low speed cruise was collected and published.

The M222 is larger than the MTR with a rotor radius of 13 ft and aspect ratio of 8.3. This rotor is not uniform and also has a high twist, -41°/span. Several airfoils define the blade profile. NACA 23012 is used inboard and BOEING 23010-158 outboard. The C81 decks for these airfoils are used to obtain the sectional aerodynamics. Free wake is used with a single tip vortex trailer per blade to compare predictions with data and previous analysis [31].

The data was acquired by running a collective sweep and measuring thrust, rotor speed, and torque, from which power is calculated. The rotor was mounted on a six axis load cell measuring all hub forces and moments. Similar to the MTR, the production of thrust resulted in tunnel recirculation inducing a vertical climb condition rather than pure hover. However, unlike the MTR, the tunnel fans were used judiciously to obtain data at multiple inflow ratios for the same collective by running in reverse to offset the flow generated. Thus, these data capture an important variation not captured by the MTR, and more akin to cruise. The data and predictions are plotted with inflow ratio λ_c on the horizontal at several collective angles.

First, thrust coefficient is shown in Fig. 4.16. The predictions follow the data closely. The gray lines are predictions obtained using the baseline comprehensive analysis to ensure consistency with previous validation.

Next, power coefficient is shown in Fig. 4.17. Similar to thrust, the results appropriately predict the power and match previous validation. There is discrepancy at $\theta_{75} = 12°$ but the scarcity of data makes any conclusion premature.

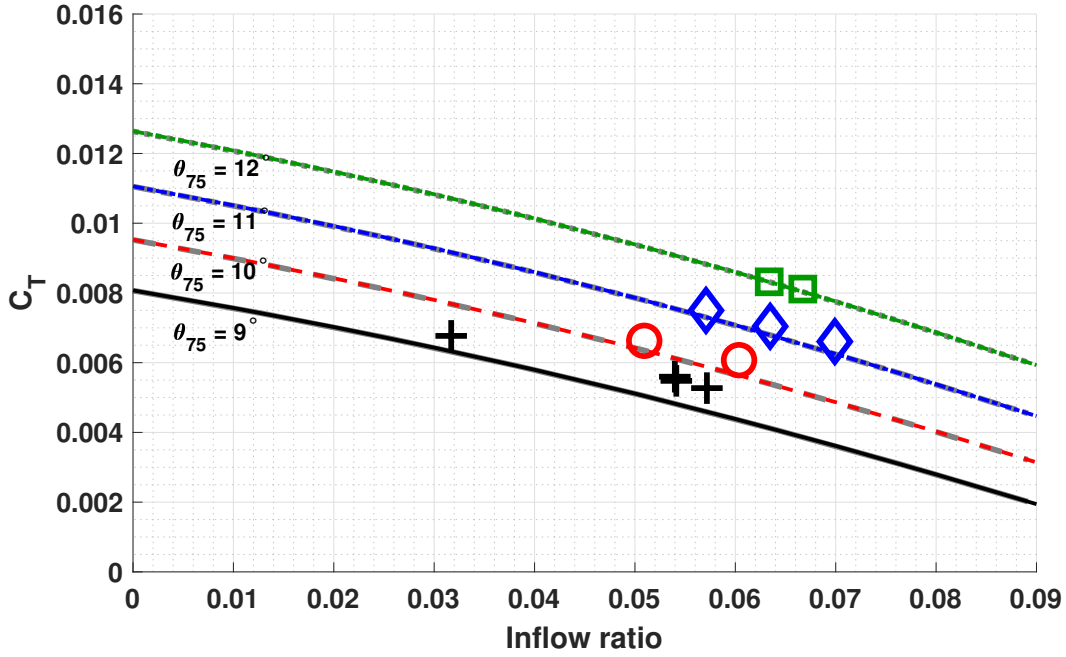


Figure 4.16: M222 measured thrust coefficient (markers) compared with UMARC-II predictions (lines) versus non-dimensional tunnel speed λ_c.

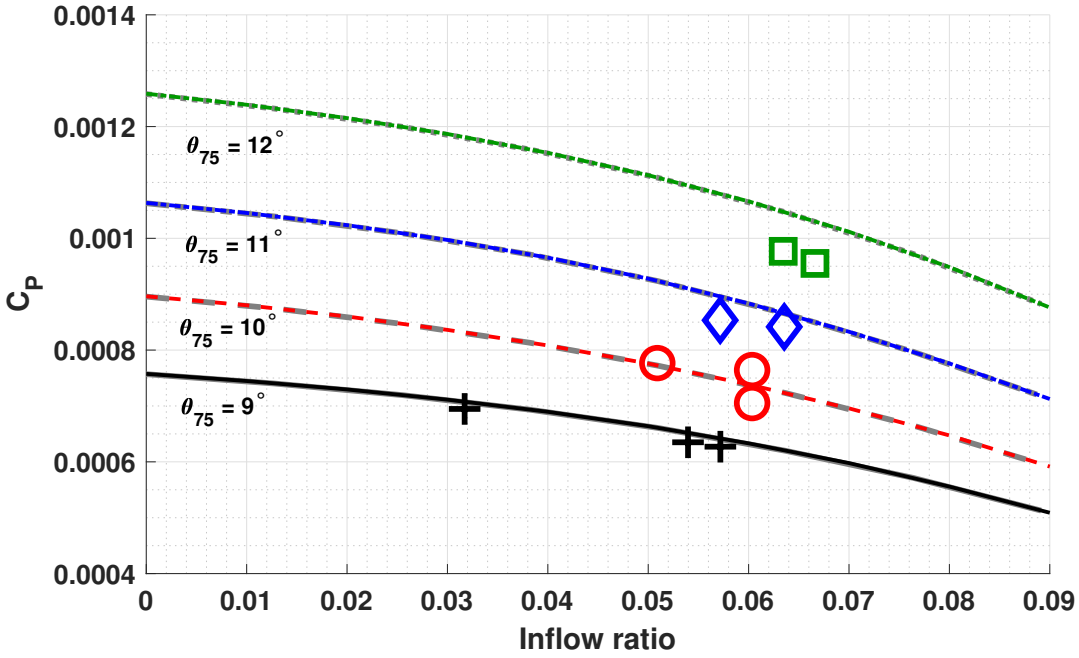


Figure 4.17: M222 measured power coefficient (markers) compared with UMARC-II predictions (lines) versus non-dimensional tunnel speed λ_c.

4.3.3 Structural Loads

The M222 test campaign provides a wealth of data from which we can validate the loads predictions of UMARC-II. Structural properties are available for both the rotor and the wing making it an ideal candidate to validate loads predictions. The rotor is analyzed as tested — as an isolated rotor experiencing a steady flight speed.

The structural model consists of 22 finite elements. The predicted fanplot with the first five frequencies is shown in Fig. 4.18. The measured non-rotating frequencies for first flap and lag are also shown. Rotating frequencies were measured at certain RPM and collectives for the first bending mode. The points are plotted as red markers with the associated collective written next to it. Predictions are generated for a collective of 8.8°, the solid lines, and 40°, the dashed lines. They are almost identical. The predictions match the data well. The hover speed was 551 RPM which placed the first lag frequency at 0.65/rev and the first flap frequency at 1.18/rev.

Tiltrotors must operate in many different flight regimes. Edgewise flight is where the highest loads are anticipated. Therefore, data collected from edgewise test cases are used to validate structural loads. The blades had strain gauges at 3.9%, 10.5%, 22.5%, and 55% radial stations. Periodic data was not reported, e.g. flap bending moment versus azimuth was not reported. Instead, half peak-to-peak (HPP) flap and chord bending moments were reported. For the hub, only mean pitch and roll moments are available.

The experiments were conducted by fixing one of the cyclics and varying the other. The published data has either lateral cyclic, θ_{1c}, or longitudinal cyclic, θ_{1s}, on the horizontal. The blade pitch is controlled by 1/rev inputs to the swashplate.

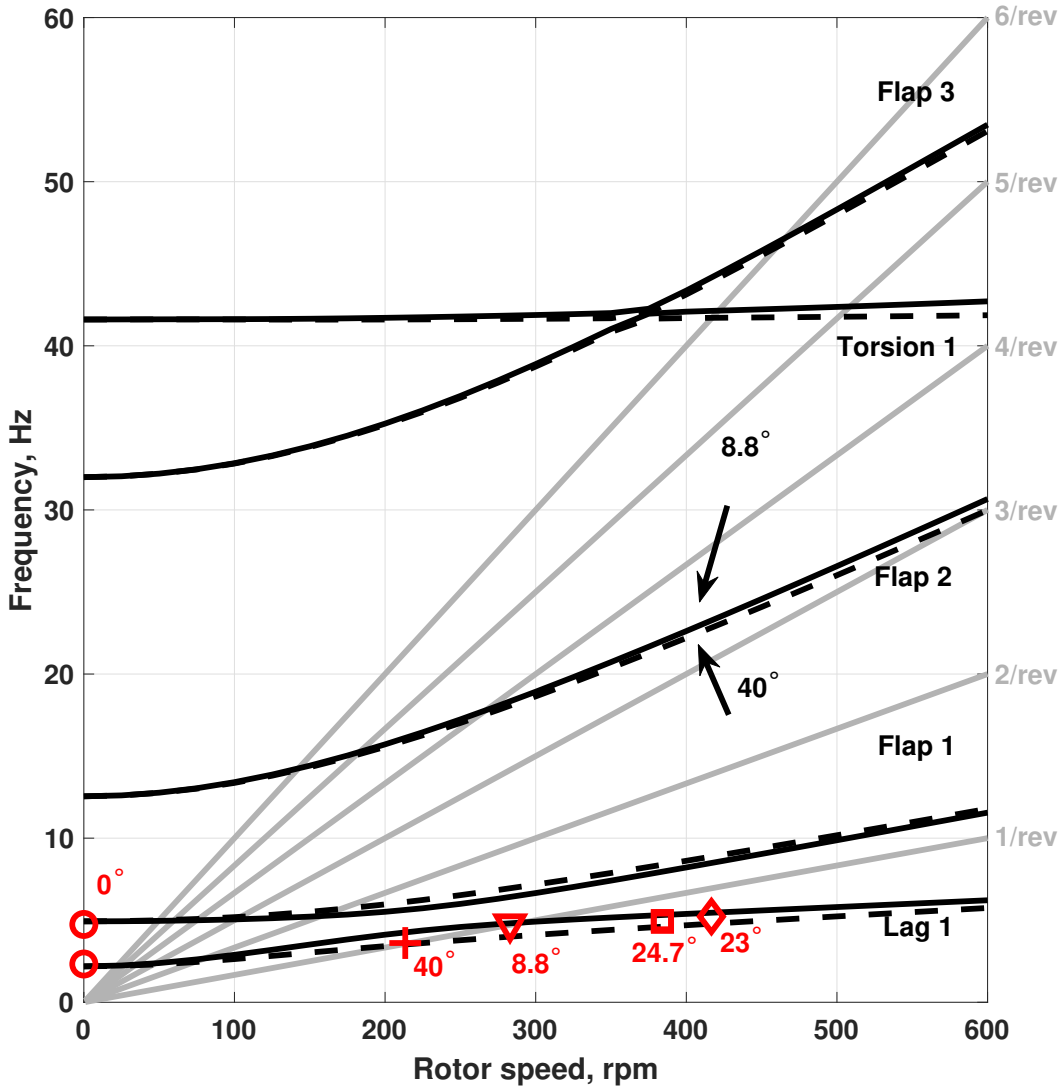


Figure 4.18: Fanplot of the M222 rotor. Measured (markers) compared with UMARC-II predictions (lines).

$$\theta = \theta_{75} + \theta_{1c} \cos \psi + \theta_{1s} \sin \psi \tag{4.5}$$

The following charts will show variation with lateral cyclic. The longitudinal cyclic is fixed at $\theta_{1s} = -1.41°$. The tunnel speed is 45 knots, the pylon incidence angle is $i_N = 85°$ up from airplane mode, equivalent to $5°$ down from helicopter mode, and the rotor speed is 500 RPM. The speed is reduced from 551 RPM for this test because of ground resonance concerns at higher pylon incidence angles. This results in an advance ratio of $\mu = 0.11$. The advance ratio is a non-dimensional metric that relates the velocity of the airflow in-plane with the rotor to the tip speed. It is defined as,

$$\mu = \frac{U \cos \alpha_s}{\Omega R}. \tag{4.6}$$

The angle of the disk into the flow measured from helicopter mode is termed the shaft angle, α_s. In this test case, $\alpha_s = 5°$, the flight speed is 45 knots, or 23.15 m/s, and the tip speed is 207.35 m/s resulting in $\mu = 0.11$.

This flight condition is important because around this advance ratio is when the blades start to interact with the trailed intertwined tip vortices on both the advancing and retreating side of the rotor, creating impulse loading. This impulse loading increases the peak-to-peak oscillatory loads that the blades experience. A time marching freewake scheme is used to propagate the tip vortex trailers and a second order lifting line model, also called nonlinear nearwake, is used to calculate the bound circulation. A single tip vortex is initialized and 40 stripwise aerodynamic panels are used with the resolution of panels increasing towards the blade tip. A 5° azimuth step is used to propagate the trailers in time. Finally, the tip vortex is initialized with a strength of 70% of the maximum bound circulation at the local time step.

Figure 4.19 shows the half peak-to-peak (HPP) flap bending moment versus lateral cyclic, θ_{1c}. The prediction at 55% R is reasonable and appears insensitive to lateral cyclic. The prediction at 3.9% R is less accurate but shows the same trend with lateral cyclic. The lateral cyclic required is underpredicted by 1°. As lateral cyclic increases, the peak-to-peak value of flap bending moment decreases and arrives at a minimum in the prediction. The trend reverses as lateral cyclic continues to increase, although there is no data to confirm this reversal.

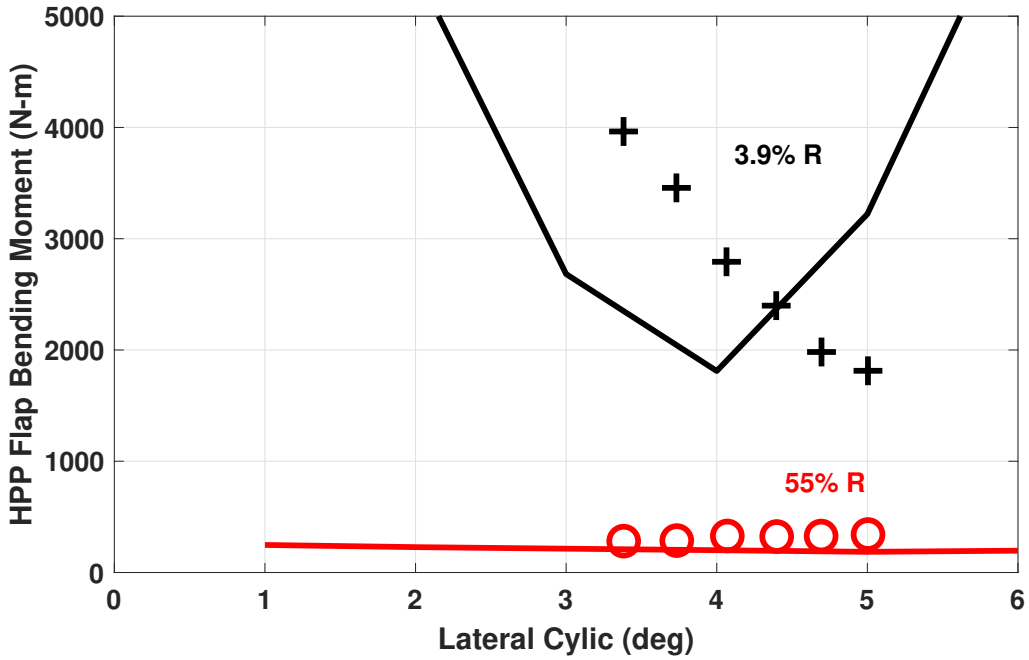


Figure 4.19: M222 half peak-to-peak flap bending moment in low speed flight (45 knots). Measured (markers) compared with UMARC-II predictions (lines).

The chord bending moment, shown in Fig. 4.20, shows the trend reversal clearly. A cyclic input exists that minimizes the oscillatory bending moment. This value is well underpredicted by about 0.5° at 3.9% R and overpredicted by about 0.5° at 55% R. The magnitude of the chord bending moment at 55% R is well predicted but the magnitude at 3.9% is significantly overpredicted, almost doubled. Bending moments near the blade root (3.9% R is very close to the shaft) are extremely difficult to measure, so this level of validation is satisfactory. The structure this close to the hub is

very stiff. Strain gauges measure strain and the bending moments are calibrated to it. The strains are extremely small and lead to low signal to noise ratio making precise measurement difficult. The hub is also complex structurally and aerodynamically to model. Thus, just HPP values are not adequate for proper validation. Azimuthal data is needed in the future and would have immense value to understand this problem.

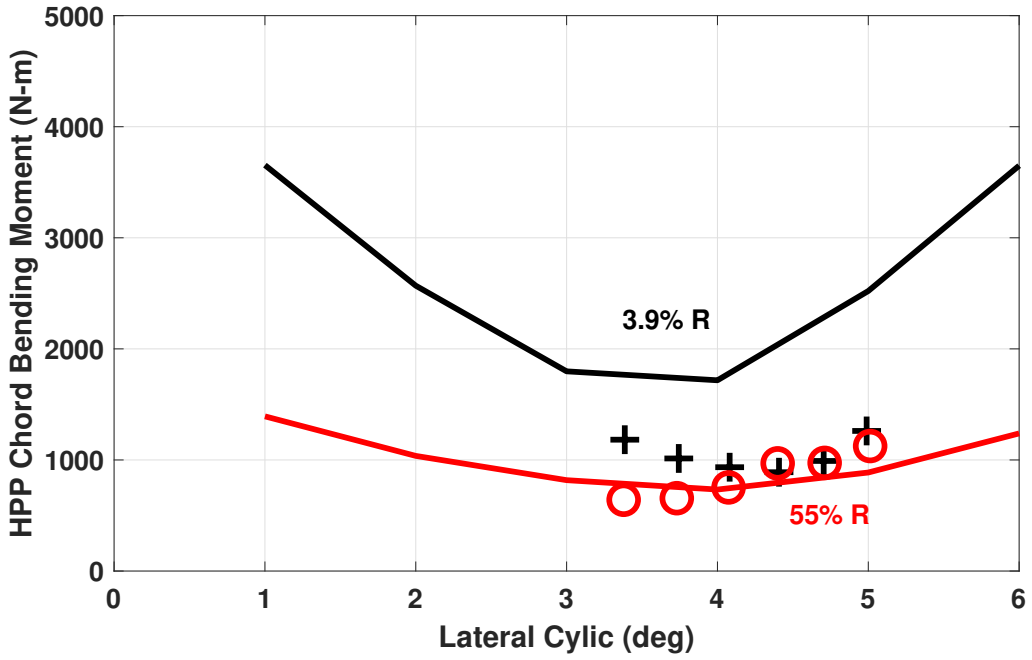


Figure 4.20: M222 half peak-to-peak chord bending moment in low speed flight (45 knots). Measured (markers) compared with UMARC-II predictions (lines).

The mean hub moments are shown in Fig. 4.21. The hub pitch moment (M_y) is displayed as red circles and the hub roll moment (M_x) as black plus signs. The mean hub roll moment is better predicted versus lateral cyclic but the pitch moment is only offset by about 1° or so. This is consistent with the offset seen previously in the blade bending moments. The hub pitch moment is defined positive nose up. The underprediction indicates the prediction of lift generated around $\psi = 180°$ is too low or the lift generated around $\psi = 0°$ is too high. This suggests the pylon is impacting the flow in some way that the analysis does not capture, but these effects cannot be verified without azimuthal data on bending

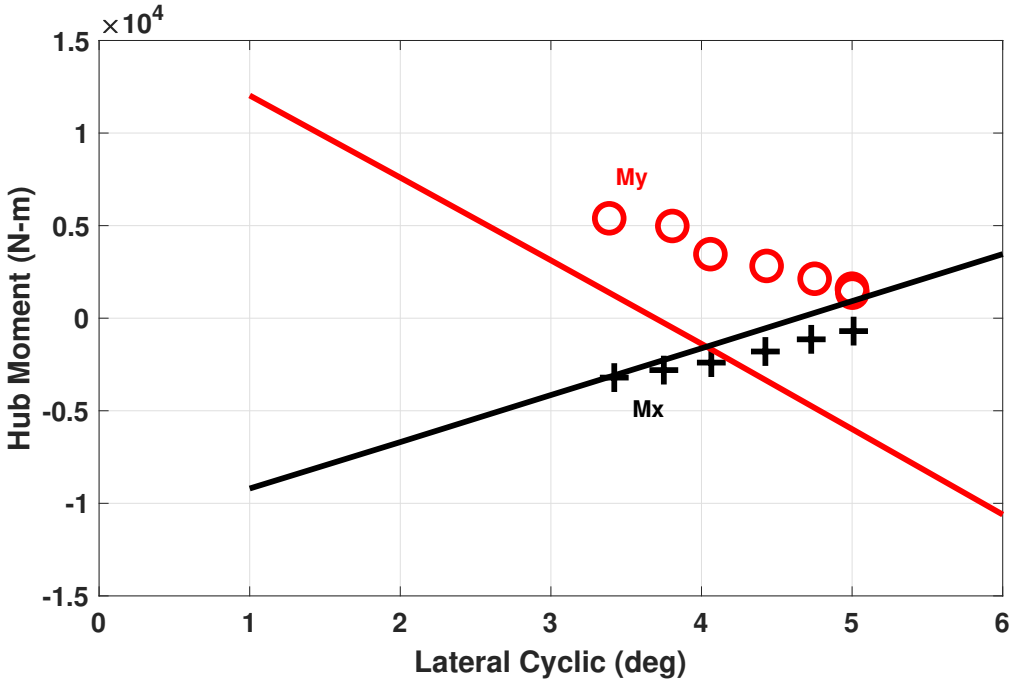


Figure 4.21: M222 mean hub moments in low speed flight (45 knots). Measured (markers) compared with UMARC-II predictions (lines).

moments. The data is replotted in Fig. 4.22 with the moments non-dimensionalized by the respective thrust and rotor radius. This provides targets for future wind tunnel testing at different scales.

The next validation is at a higher speed. The tunnel speed is 105 knots, the pylon incidence angle is $i_N = 27°$, again measured up from airplane mode, and the rotor speed is 551 RPM. The advance ratio is again $\mu = 0.11$ but the inflow through the disk is much higher. Recall the formula for advance ratio. The shaft angle here is $\alpha_s = 63°$, the flight speed is 105 knots, or 54.02 m/s, and the tip speed 228.49 m/s, resulting in $\mu = 0.11$. The longitudinal cyclic is fixed at $\theta_{1s} = -2.56°$. The free wake parameters are kept the same.

Figure 4.23 shows the flap bending moment versus lateral cyclic. The reversal of the bending moment is captured in this data, so the predictions are correct. Despite the trends being well captured, the lateral cyclic that minimizes the flap bending moment is underpredicted by 1°. This discrepancy is consistent with the predictions for the lower speed case. The magnitude is underpredicted as well,

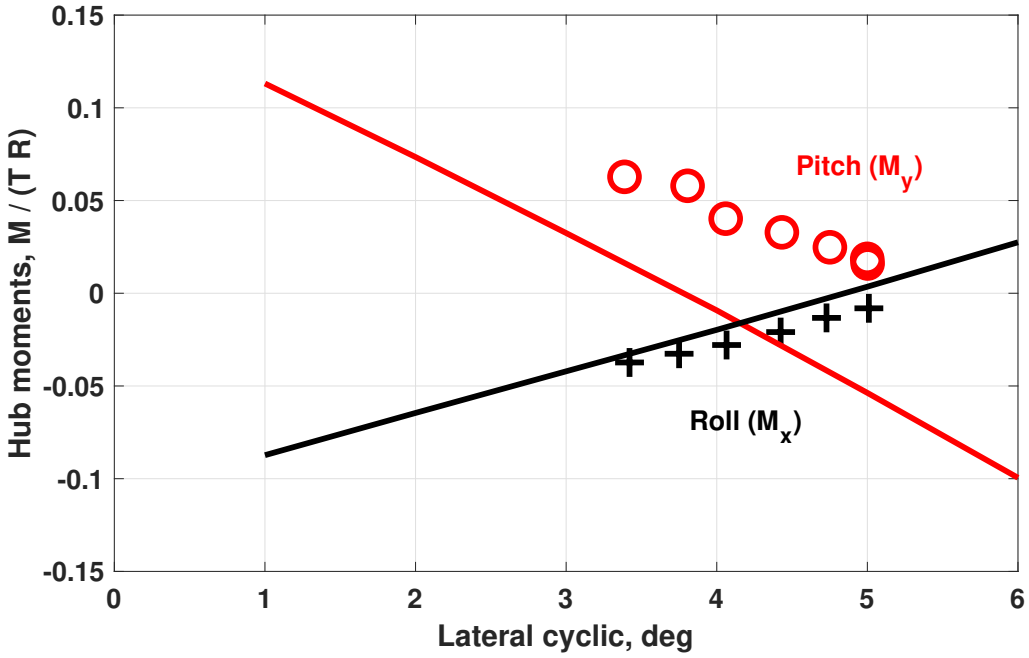


Figure 4.22: M222 non-dimensionalized mean hub moments in low speed flight (45 knots). Measured (markers) compared with UMARC-II predictions (lines).

with the gap increasing near the root.

The chord bending moment is shown in Fig. 4.24. Similar to flap, the lateral cyclic to minimize the load is underpredicted along with the magnitude. The trends in both flap and chord bending moments are consistent with low speed. Overall, the predictions are very good in magnitude and trends except for the radial station closest to the hub.

The mean hub moments are shown in Fig. 4.25. Now, both hub pitch and roll are underpredicted by 1° of lateral cyclic. The magnitude and trends however are well captured. Like the low speed case, the moments are non-dimensionalized and replotted in Fig. 4.26.

In all, the rotor thrust, power (i.e. torque), and hub moments are crucial for a proper trim solution and power prediction later for our aircraft. This validation provides confidence in the accuracy of the analysis.

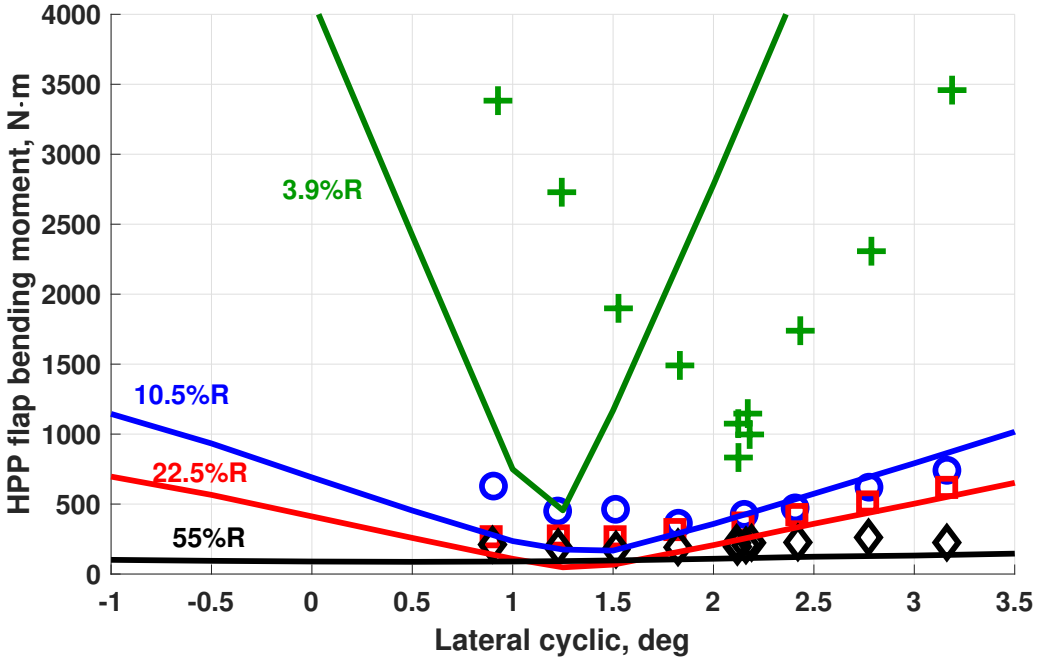


Figure 4.23: M222 half peak-to-peak flap bending moment in high speed flight (105 knots). Measured (markers) compared with UMARC-II predictions (lines).

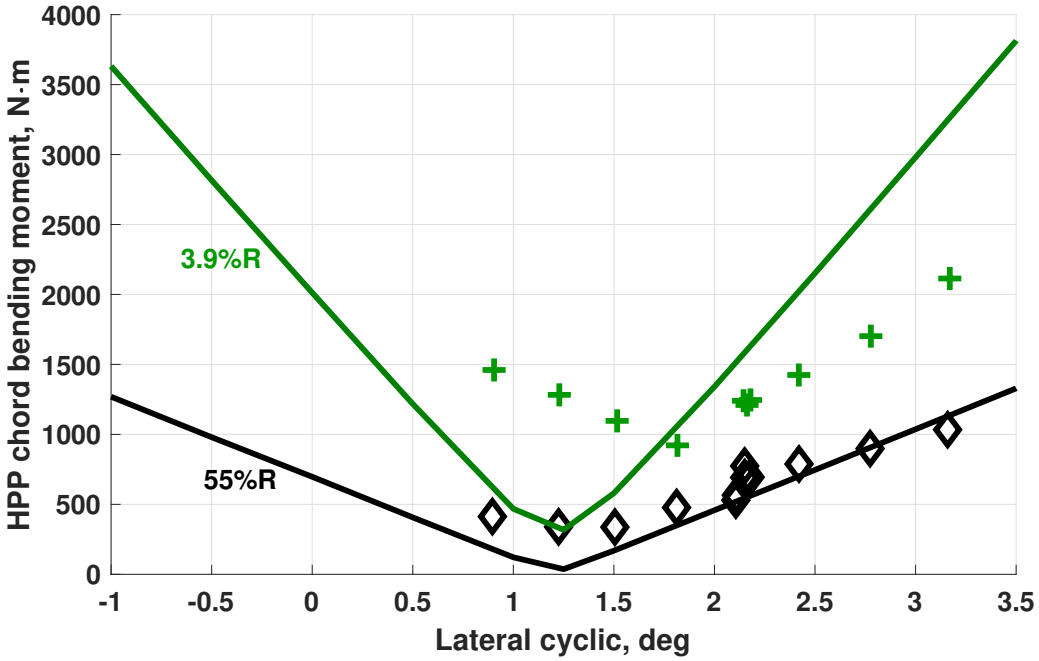


Figure 4.24: M222 half peak-to-peak chord bending moment in high speed flight (105 knots). Measured (markers) compared with UMARC-II predictions (lines).

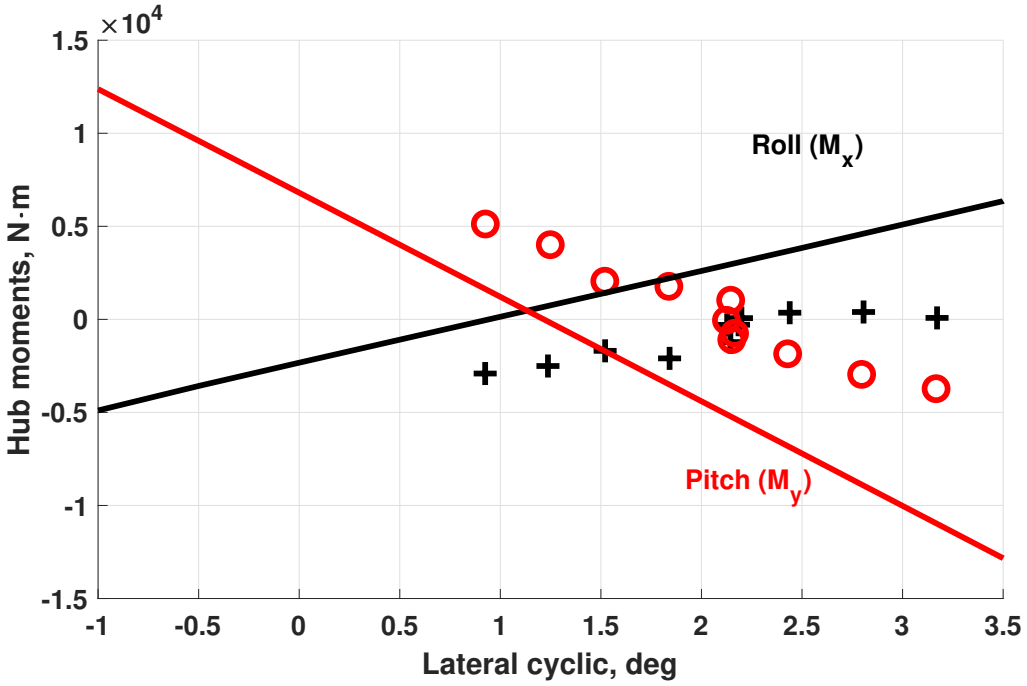


Figure 4.25: M222 mean hub moments in high speed flight (105 knots). Measured (markers) compared with UMARC-II predictions (lines).

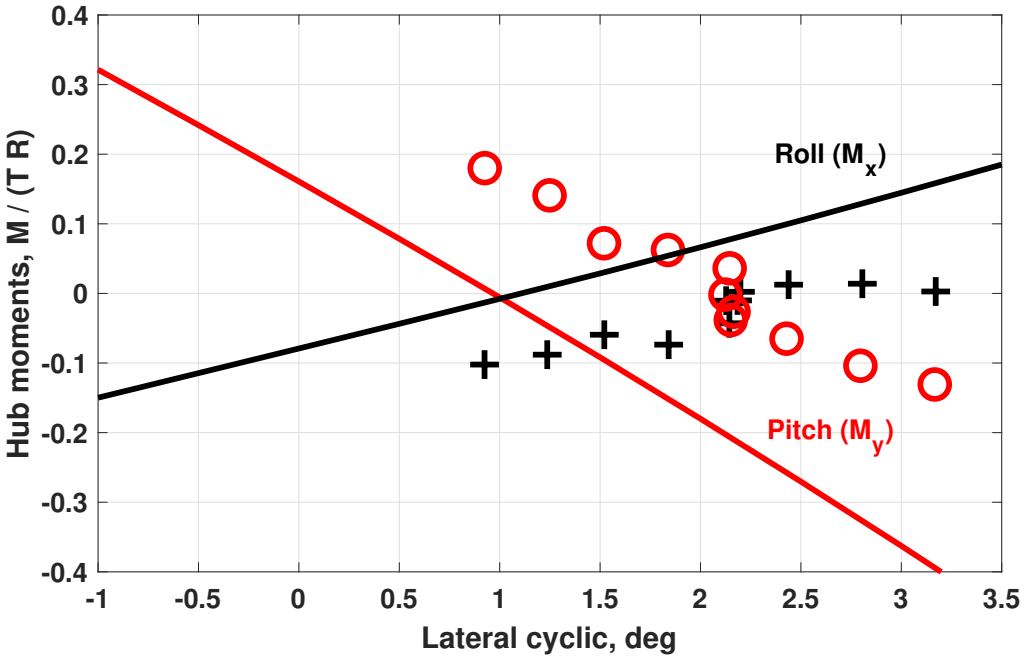


Figure 4.26: M222 non-dimensionalized mean hub moments in high speed flight (105 knots). Measured (markers) compared with UMARC-II predictions (lines).

4.4 Rotors on wings

A characteristic of electric and hybrid-electric VTOL has been rotors mounted on wings. Mounting one flexible structure on another — with one rotating and the other fixed — generates challenging dynamics due to time varying inertia and impacts the vibratory loads. It can also lead to dangerous instabilities such as whirl flutter. While whirl flutter is a separate field of research and out of scope from this work, the question here is, for a stable rotor, what is the impact on loads when the rotor is coupled to a flexible support?

This is the first element of analysis in this dissertation where no publicly available data exists to correlate with. However, the analysis must still be anchored to what is known. Therefore, the M222 rotor is retained but now a hypothetical wing is introduced underneath. The wing structure is modeled with seven finite elements. The first five frequencies of the isolated, cantilevered wing are given in Table 4.1. Figure 4.27 shows an illustration of the rotor mounted on the wing tip. The black dots are the actual structural nodes, or element boundaries. Wing aerodynamic panels are the red rectangles. The wing is a lifting line at 1/4 c so the panels are merely to illustrate the boundaries of each line segment.

Table 4.1: First five frequencies of the M222 wing in /rev. Rotor 551 RPM.

Beam bending 1	0.22
Chord bending 1	0.37
Torsion 1	0.90
Chord bending 2	3.99
Beam bending 2	6.76

The same high speed condition is studied, the only difference is the addition of the wing. The wing is modeled with the NACA 0012 airfoil. Two configurations are analyzed. The first is with a

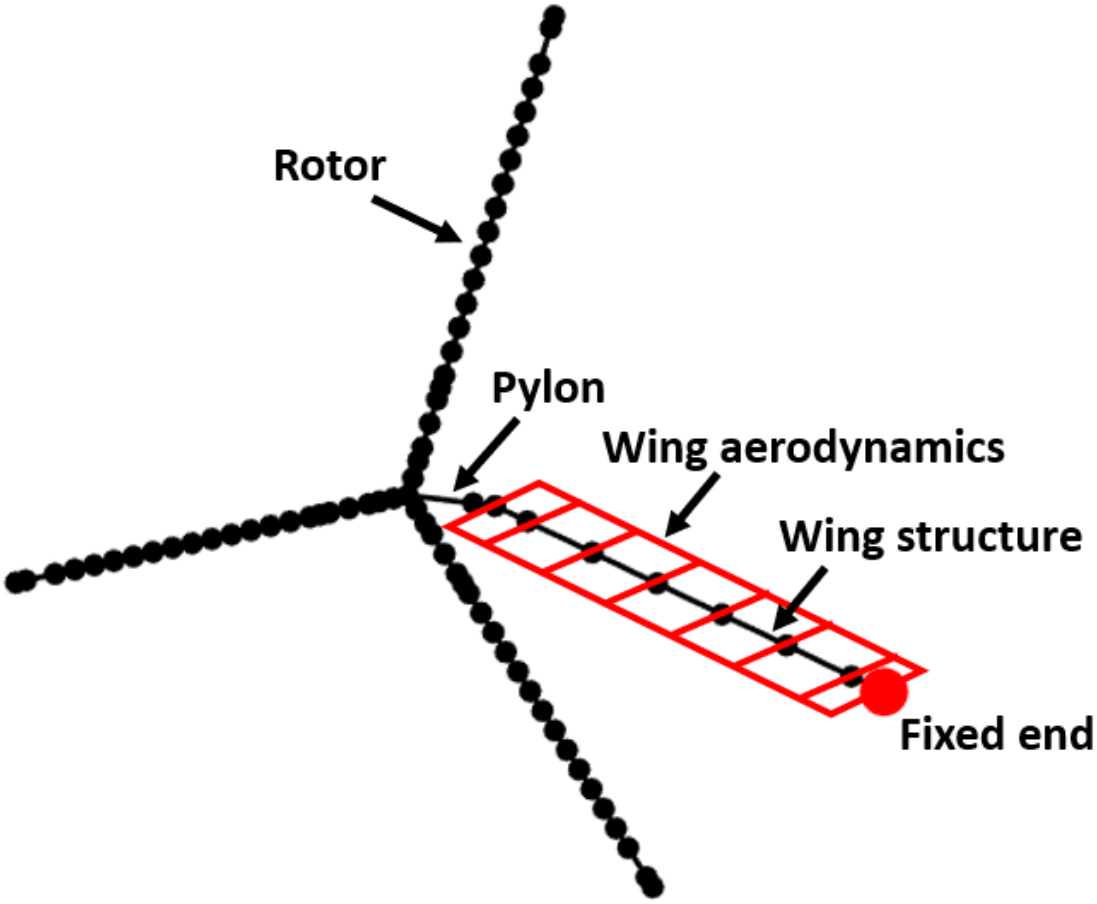


Figure 4.27: Finite element model of a single rotor mounted on a wing tip.

wing incidence angle of 4° (low lift). The second configuration is with a wing incidence angle of 12° (high lift). This is done to gradually strengthen the wing tip vortex and bound circulation that may interact with the rotor.

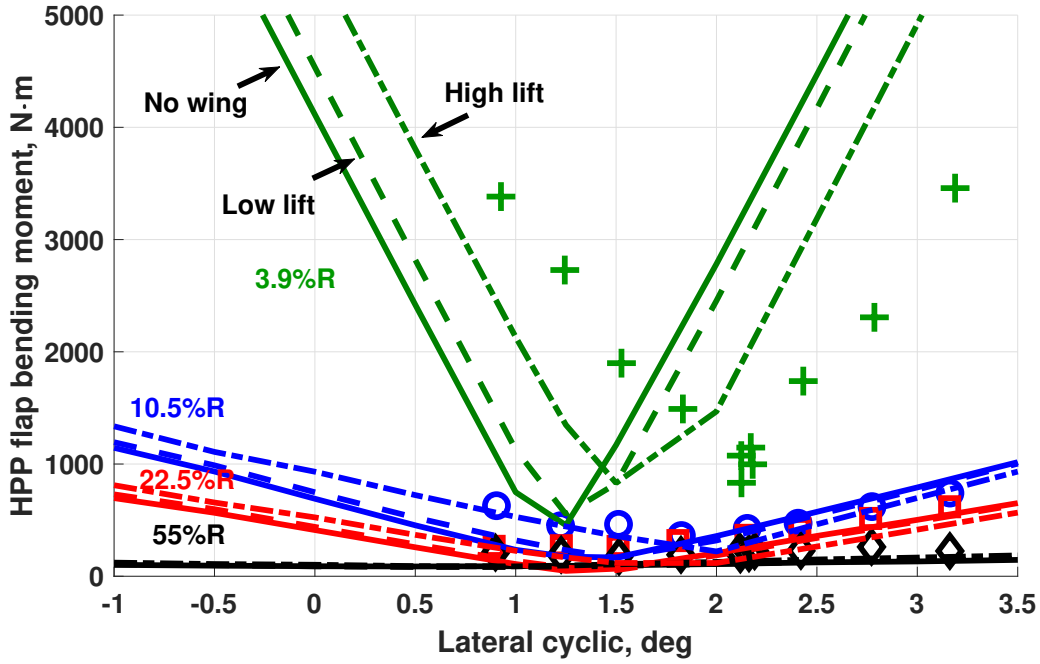


Figure 4.28: M222 half peak-to-peak flap bending moment in high speed flight (105 knots). No wing (solid), wing at $\alpha = 4°$ (dashed), wing at $\alpha = 12°$ (dot-dashed).

The flap bending moment versus lateral cyclic is shown in Fig. 4.28. The solid lines are retained from the isolated rotor case. The dashed line is the lower lift configuration and the dot-dashed line is higher lift. At each radial station, the HPP flap bending moment increases in magnitude, strengthening towards the blade root. The magnitude increases as the wing lift increases. Additionally, more cyclic becomes necessary to minimize the oscillatory flap bending moment.

The lines for the isolated rotor and low lift configurations are removed and replotted in Fig. 4.29 for clarity. The predictions end up closer to the experimental data at each radial station. In the wind tunnel tests, the rotor was mounted on a test stand directly below it. Even though the rotor

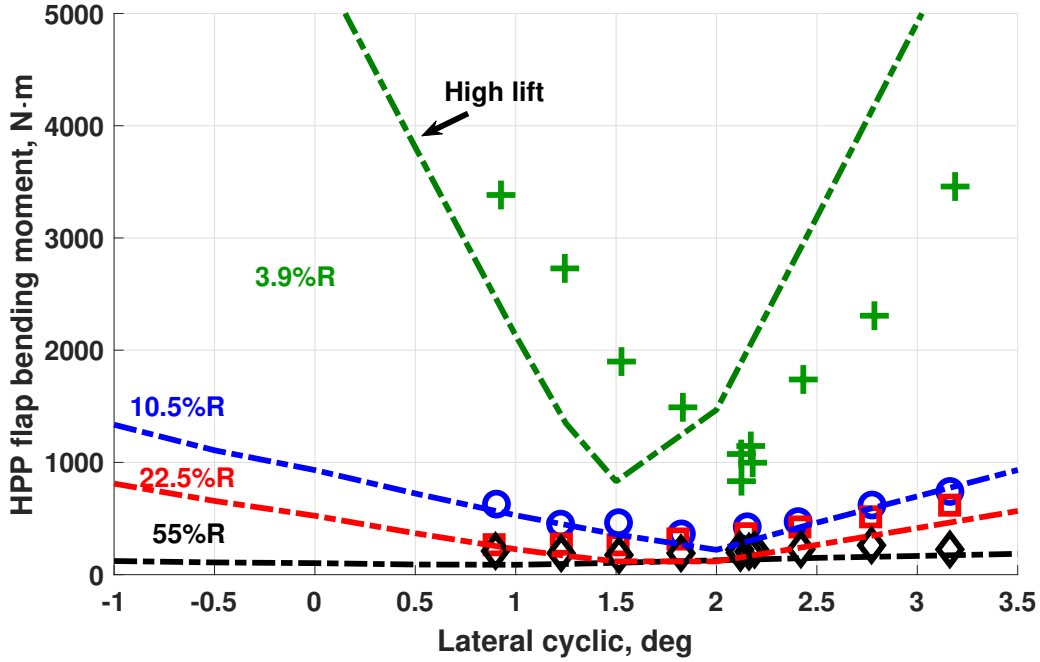


Figure 4.29: M222 half peak-to-peak flap bending moment in high speed flight (105 knots). Wing at $\alpha = 12°$ (dot-dashed).

support structure was not a wing, these results indicate the presence of an interaction between the rotor and a fixed structure. The lateral cyclic to minimize the flap bending moment at the hub is now underpredicted by only 0.5°. Figure 4.30 shows the chord bending moment. The same trend is seen as flap. The magnitude of the HPP chord bending moment is less underpredicted than with the isolated rotor. The lateral cyclic to minimize the chord bending moment at 55% R is now correct while the cyclic necessary for the root is underpredicted by less than 0.5°. Finally, the mean hub moments are shown in Fig. 4.31. As the wing generates more lift, both the hub pitch and roll moments strengthen at any given lateral cyclic. The predictions once again approach the measured data. The presence of a wing increases the 1/rev oscillatory blade moments, hence the mean hub moments. As the blade moments increase in magnitude, more lateral cyclic is required to minimize them.

Why does the wing influence the rotor in this way? Is this a result of aerodynamics or structures?

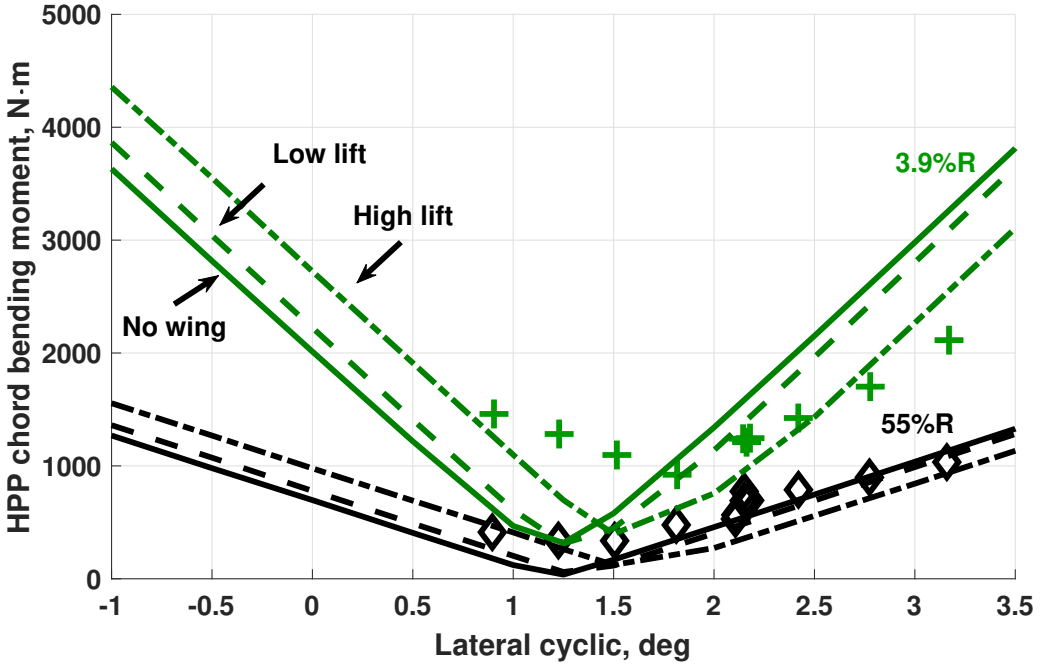


Figure 4.30: M222 half peak-to-peak chord bending moment in high speed flight (105 knots). No wing (solid), wing at $\alpha = 4°$ (dashed), wing at $\alpha = 12°$ (dot-dashed).

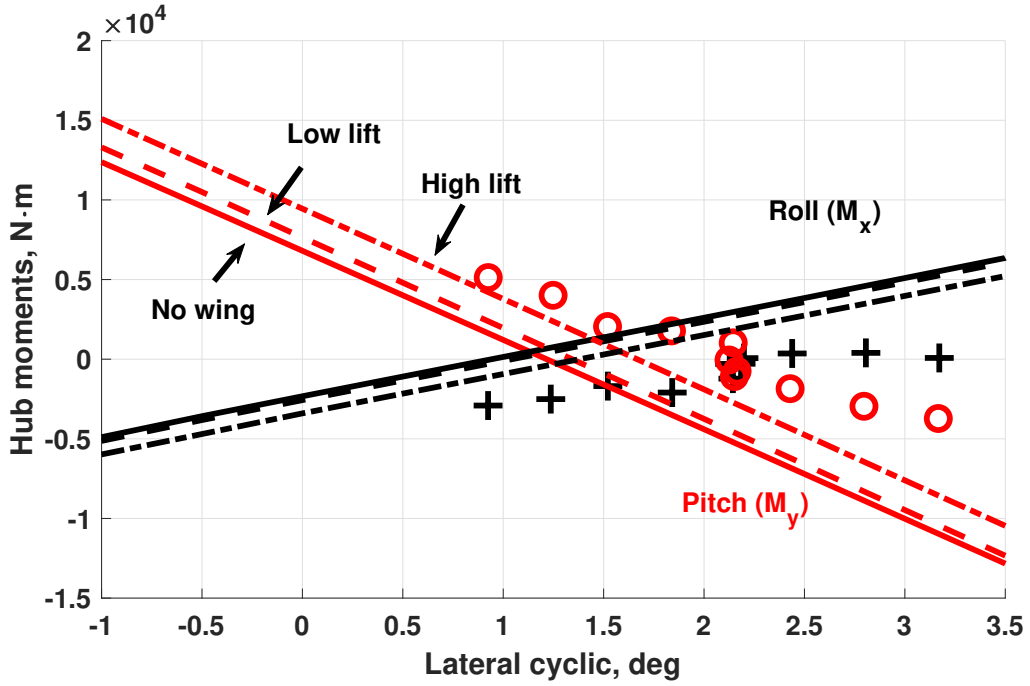


Figure 4.31: M222 mean hub moments in high speed flight (105 knots). No wing (solid), wing at $\alpha = 4°$ (dashed), wing at $\alpha = 12°$ (dot-dashed).

To investigate this we turn off the aerodynamics of the wing. Doing so essentially turns the wing into a boom. Figures 4.32 and 4.33 show two different configurations. The first is the exact orientation as the previous case, now without aerodynamics. The second is rotated such that it protrudes into the flow like a boom. From these configurations we should be able to deduce the impact of a rotor mounted to a non-lifting structure on the blade oscillatory moments and mean hub moments.

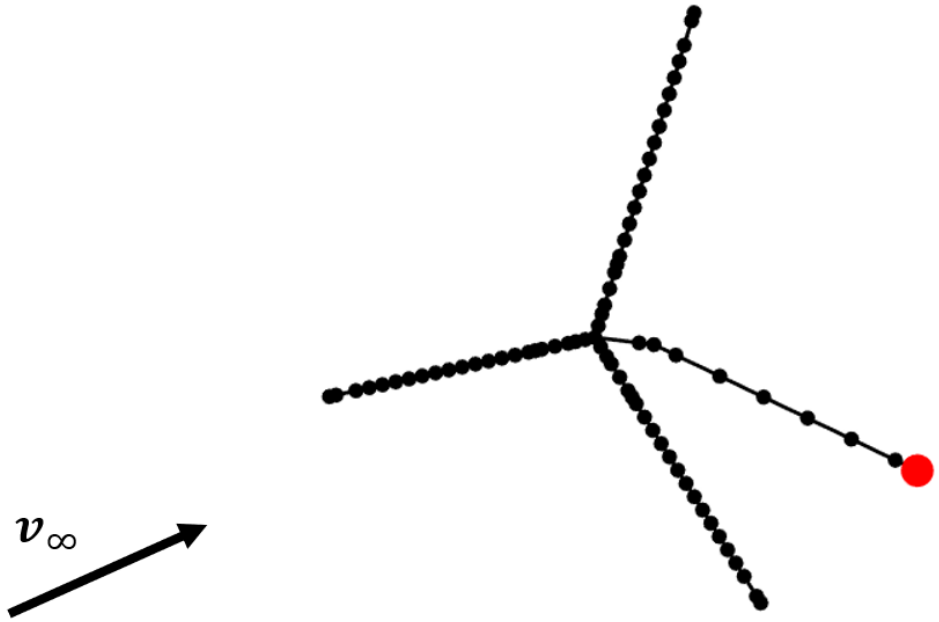


Figure 4.32: Finite element model of the M222 rotor on a horizontal boom, like a wing.

The transition case is retained because of the large moments. The solution parameters are kept exactly the same. First, figure 4.34 shows the flap bending moment. All of the predictions are almost exactly the same as the isolated rotor with aerodynamics. The wing structure is flexible and does deform, but not nearly enough to influence the forcing and response of the rotor. This indicates that structural coupling is not the driver of the increased oscillatory moments. The same conclusion is drawn from Fig. 4.35 for chord.

Given the blade moments do not change, the hub moments should not change as well. That

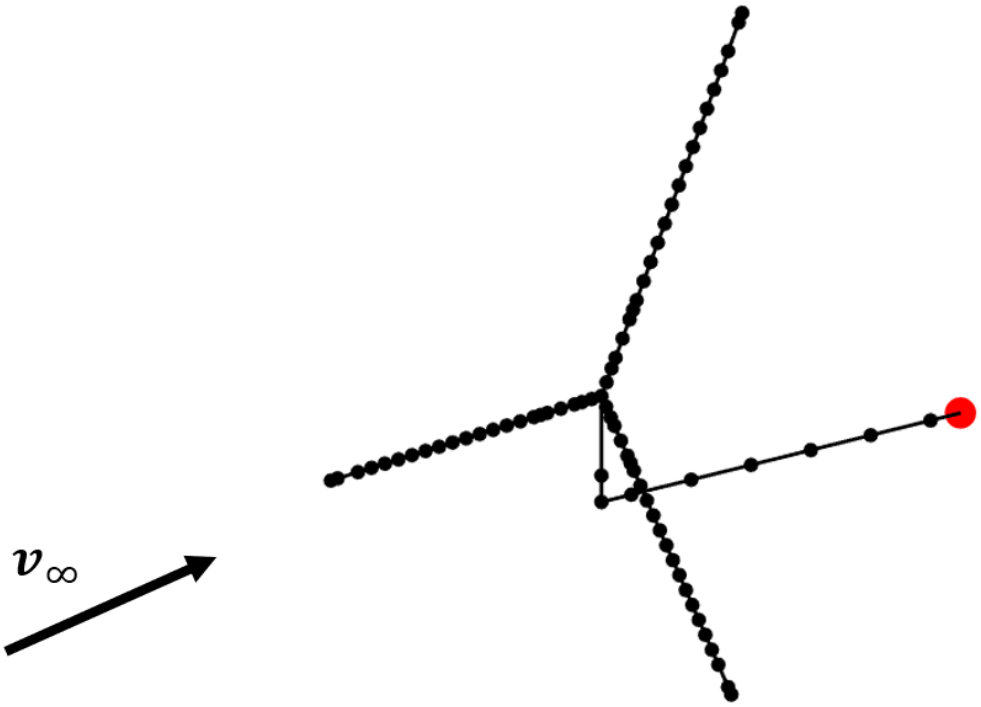


Figure 4.33: Finite element model of the M222 rotor on a vertical boom, protruding into the airflow.

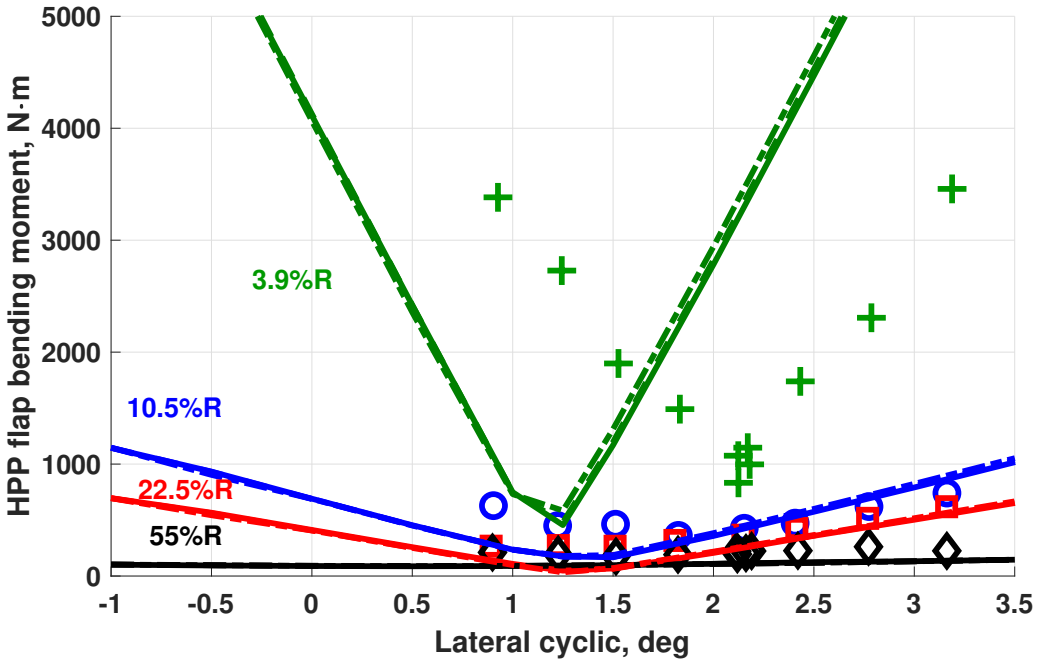


Figure 4.34: M222 half peak-to-peak flap bending moment in high speed flight (105 knots). No wing (solid), horizontal boom (dashed), vertical boom (dot-dashed).

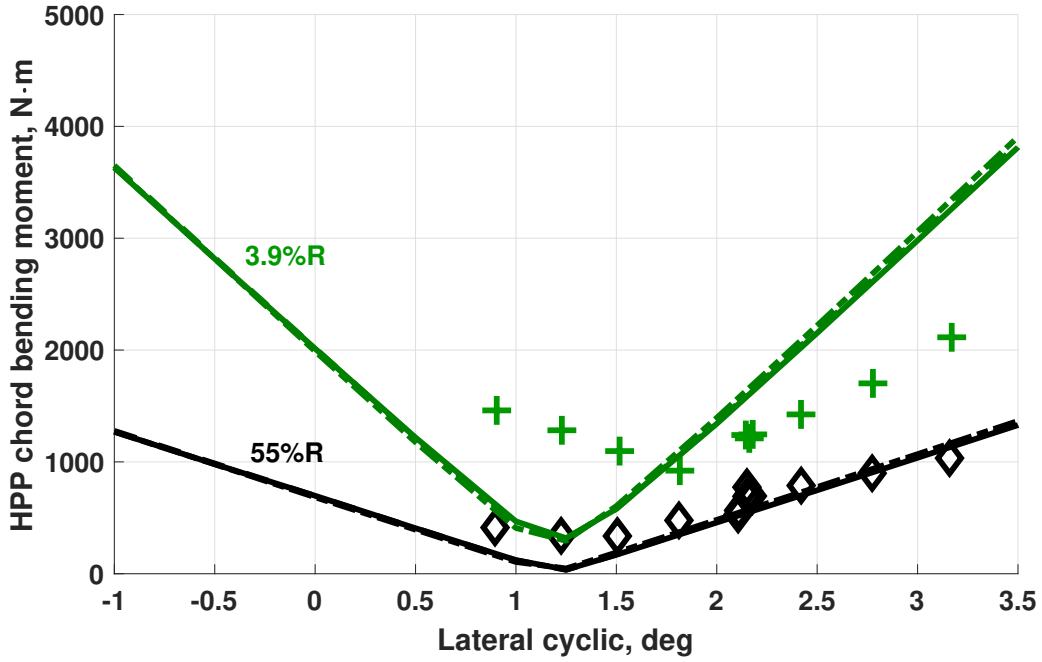


Figure 4.35: M222 half peak-to-peak chord bending moment in high speed flight (105 knots). No wing (solid), horizontal boom (dashed), vertical boom (dot-dashed).

assumption is confirmed in Fig. 4.36. These results indicate the increase in oscillatory moments and hub moments stem from the wing aerodynamics.

Looking further into the wing aerodynamics, the sectional airloads of one of the simulations are analyzed. The appropriate non-dimensional metric to represent sectional lift of a rotary-wing is M^2c_n. It is defined as,

$$M^2c_n = \frac{dN/dr}{\frac{1}{2}\rho a^2 c} \tag{4.7}$$

The sectional normal force N, in N/m, is divided by the air density, speed of sound squared, and local chord. It is essentially division by dynamic pressure times local chord but instead of the local velocity, the speed of sound is used. This ensures that this value is always defined. If instead the velocity is used, non-dimensional lift would balloon to infinity as the local velocity approaches zero,

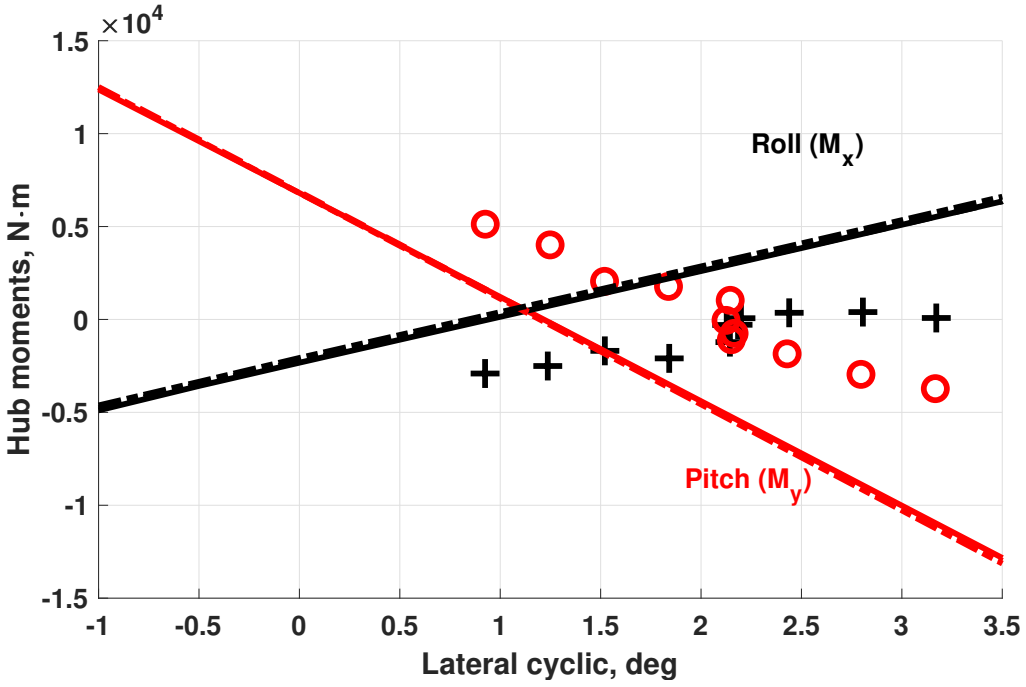


Figure 4.36: M222 mean hub moments in high speed flight (105 knots). No wing (solid), horizontal boom (dashed), vertical boom (dot-dashed).

like on the boundary of reverse flow. The result is the local normal force coefficient multiplied by the Mach number squared.

Figure 4.37 shows how the retreating side of the disk is aligned with the wing. The sectional normal force coefficient at 90% R is shown in Fig. 4.38. The figure shows that as the wing generates more lift, the sectional lift of the rotor blade near the tip experiences an impulse around $\psi = 270°$. The model predicts this behavior due to the bound circulation of the wing.

The increase in lift results in increased flapping, shown in Fig. 4.39. As the blades flap back down, the angle of attack, and subsequently lift, is reduced which results in the lower peak in $M^2 c_n$ seen around $\psi = 90°$. As a result, the presence of the wing increases the rotor blade oscillatory loading. The more lift the wing generates, the stronger this impact. The wing tip vortex does not seem to have much of an effect on these results. The increase in oscillatory blade loading and mean hub

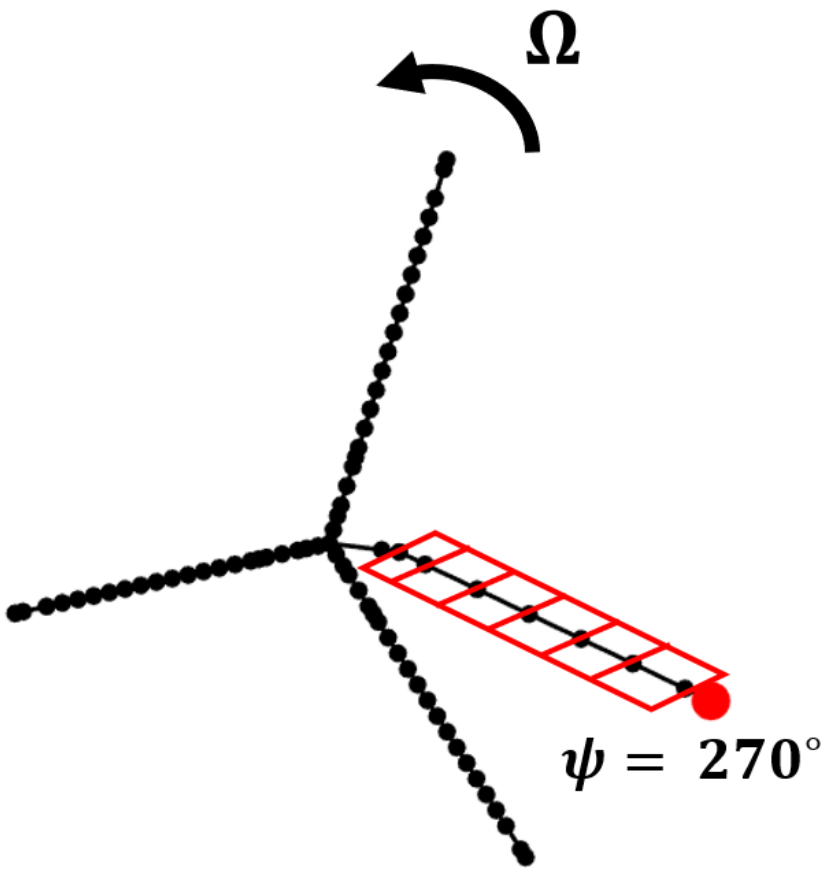


Figure 4.37: Finite element model of the M222 rotor and wing. Wing on retreating side of the rotor.

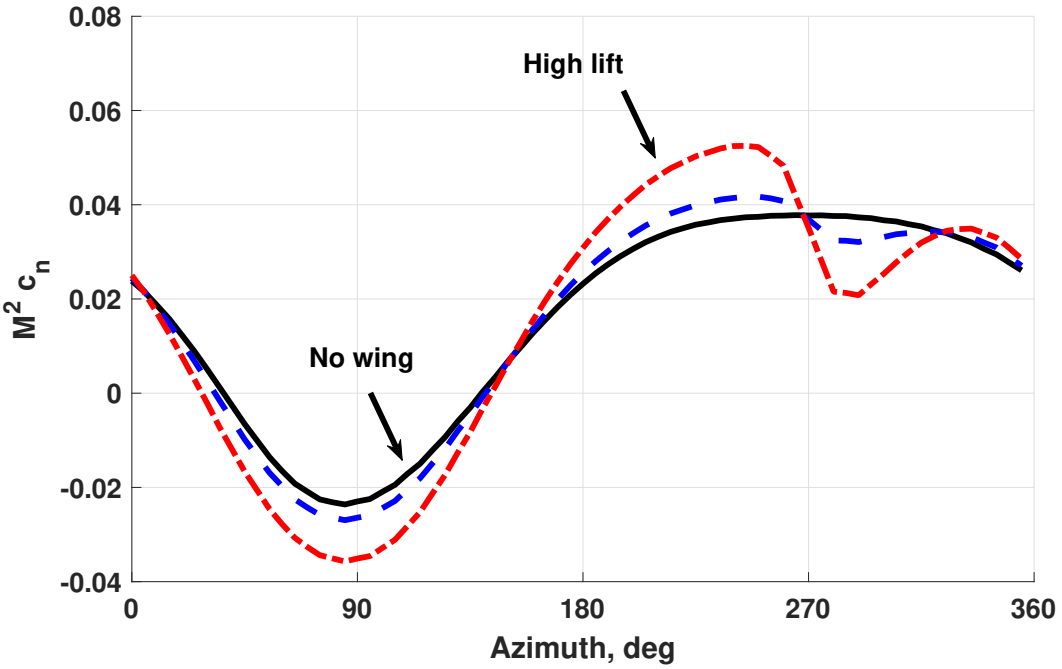


Figure 4.38: Rotary-wing normal force coefficient at 90% R versus azimuth. No wing (solid), wing at $\alpha = 4°$ (dashed), wing at $\alpha = 12°$ (dot-dashed).

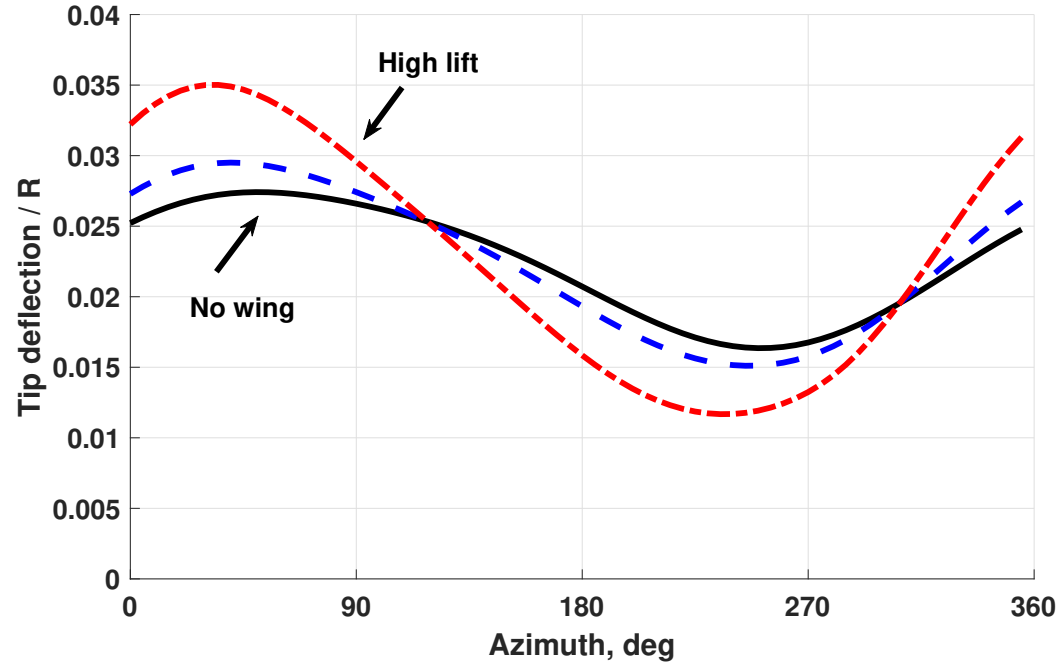


Figure 4.39: Blade tip deflection divided by radius versus azimuth. No wing (solid), wing at $\alpha = 4°$ (dashed), wing at $\alpha = 12°$ (dot-dashed).

moments primarily comes from aerodynamic interference.

4.5 Multiple rotors and multiple wings

Electric and hybrid-electric configurations often have multiple rotors and multiple wings. There is no publicly available data to reference for such a configuration. As we transition to analyzing this type of vehicle, the model is changed to that of the conceptual quad biplane. The aircraft is shown again in Fig. 4.40, has four rotors mounted on two full wings. To analyze such a configuration using comprehensive analysis, it is generally sufficient to simplify the model to a single rotor, or a single rotor mounted to a wing. If all rotors are operating purely in unimpeded flow, identical rotors will have identical results. However, many multi-rotor configurations have rotors that are not identical. Some may be geometrically equivalent but rotate in different directions for natural anti-torque and controllability. This is shown in Fig. 4.40.

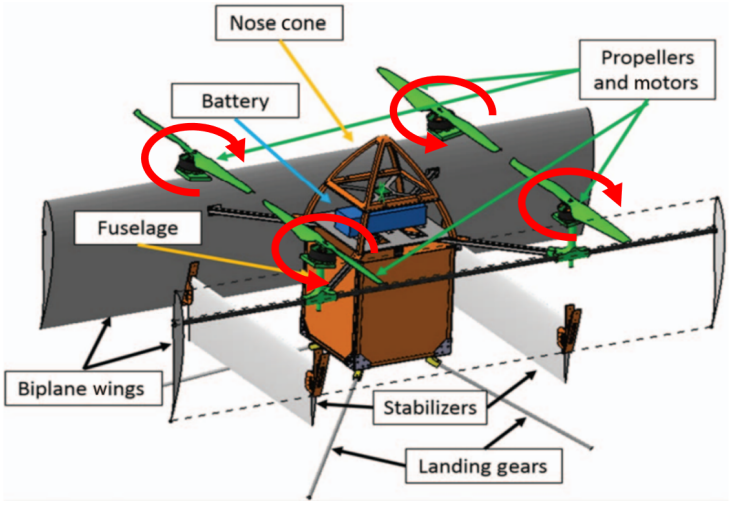


Figure 4.40: Rotor direction of rotation for quad biplane.

The model has two rotors mounted on two wings. It is assumed that the direction of rotation for each rotor of the aircraft follows this scheme. For the sake of this analysis, the model is simplified by

cutting the aircraft in half longitudinally. Since the vehicle is symmetric about the fuselage, the results from analyzing one side are applicable to the other.

The rotors are two bladed with a radius of 1.2 ft, aspect ratio of 5.7, twist of -40°/span, and root cutout of 0.1. The tip speed is nominally 328 ft/s. The blades are modeled in UMARC-II with 10 finite elements. The structural properties are not important for this analysis. The blade profile is defined by a single airfoil, VR7. The half-wings are defined by 10 finite elements, have a span of 2.9 ft, chord of 0.58 ft, and no twist with an airfoil of NACA 0012. The pylons have a length of 0.29 ft and protrude the rotors into the flow with a pylon incidence of $i_N = 0°$.

Ideally, the rotors are spaced so that they do not interfere with each other. However, the wake will always interfere with the airflow over the structure it is mounted on. When mounted to a wing, the wake of the rotor will impact the wing's lift distribution leading to oscillatory wing loads and a change in performance.

The rotor direction of rotation has a significant impact on the wing's performance at low speeds as it nears stall. A flight condition of 45 knots is chosen to understand this. Free wake is used with a single tip vortex trailer per blade and a single tip vortex per wing. The nonlinear nearwake is used to calculate the bound circulation of both the rotor blades and wing. This flight condition converged to a high body pitch, about 17°, on the boundary of wing stall. Figure 4.41 shows how the rotor vortices pass over the middle of the wing. The bottom rotor rotates counter-clockwise and the top clockwise.

This analysis revealed that the wing attached to the clockwise rotor stalls sooner than the one mounting the counter-clockwise rotor. To understand this, the wing angle of attack associated with the clockwise rotor, is plotted in 3D against spanwise position along the wing and azimuth of the rotor, shown in Fig. 4.42. The peaks are the result of a two-way interaction. The rotor vortices interact with the wing influencing angle of attack and subsequently lift, but also the wing's bound circulation

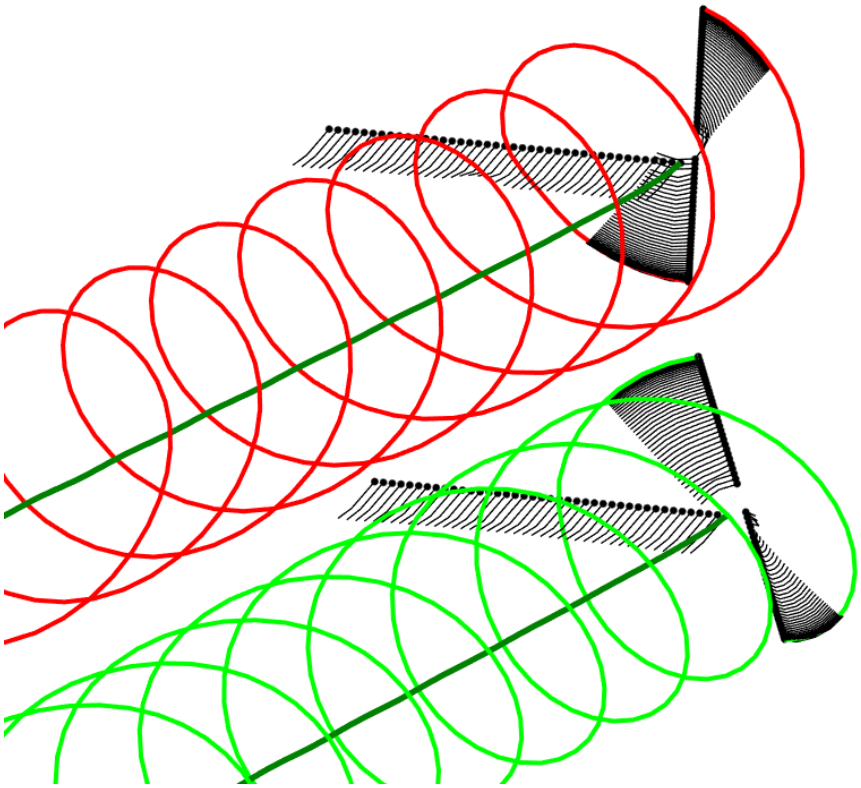


Figure 4.41: Visualization of rotor tip vortex contact with wings. Counter-clockwise rotor bottom, clockwise rotor top.

interacts with the vortices.

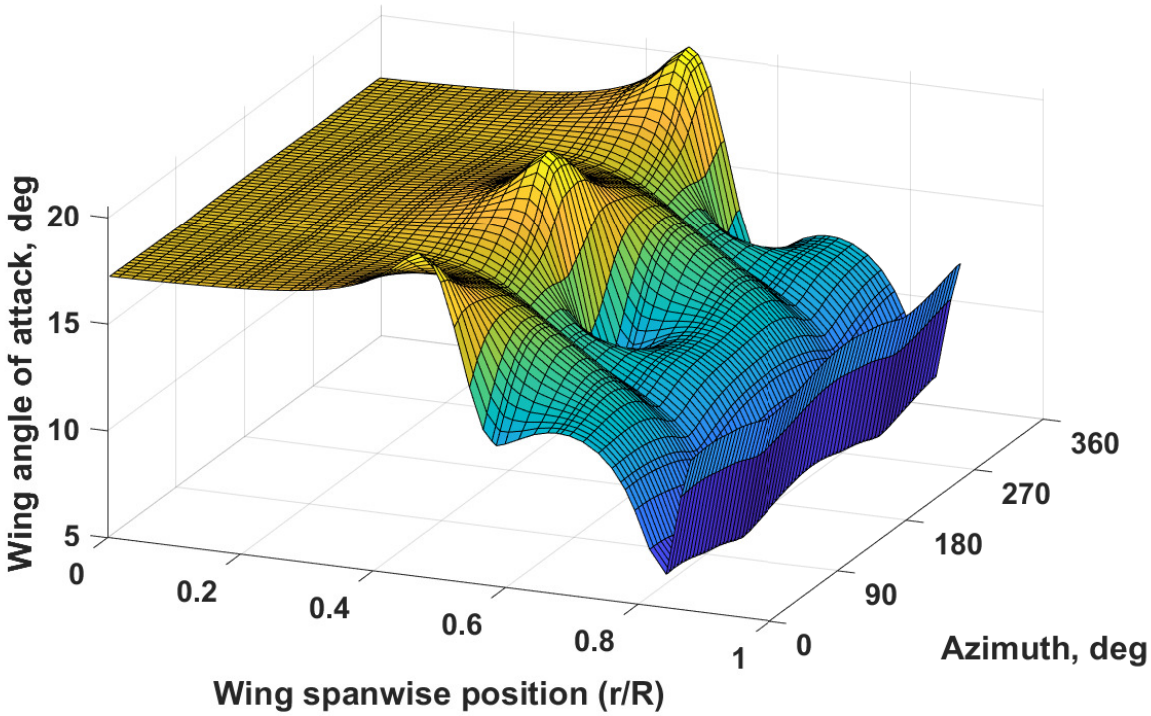


Figure 4.42: Hooper plot of wing angle of attack. Peaks from blade tip vortex passage.

Consider the illustration of the 3-bladed M222 from earlier, shown in Fig. 4.43. The bound circulation of a wing generating positive lift is defined positive nose up. As the blades generate lift, the vortices that roll up are based on the magnitude and sign of the bound circulation. For the counter-clockwise rotor, shown on the left, it is clear that the bound circulation of the rotor blade and fixed wing are naturally pointing opposite directions. The bound circulation on a fixed wing naturally weakens the trailing vortex from the rotor tip. For the clockwise rotor, on the right, the opposite is true. The bound circulations both point the same direction, so the fixed wing ends up strengthening the trailed vortices from the rotor tip. As a result, vortices of different strength interact with the wings they pass over. To generalize, the vortex will be strengthened if the rotor direction of rotation is in the same direction as the wing tip vortex. Conversely, the vortex will be weakened if the direction of rotation

opposes the natural rotation of the wing tip vortex. In this case, a weaker vortex interacts with the bottom wing and and a stronger vortex interacts with the top wing.

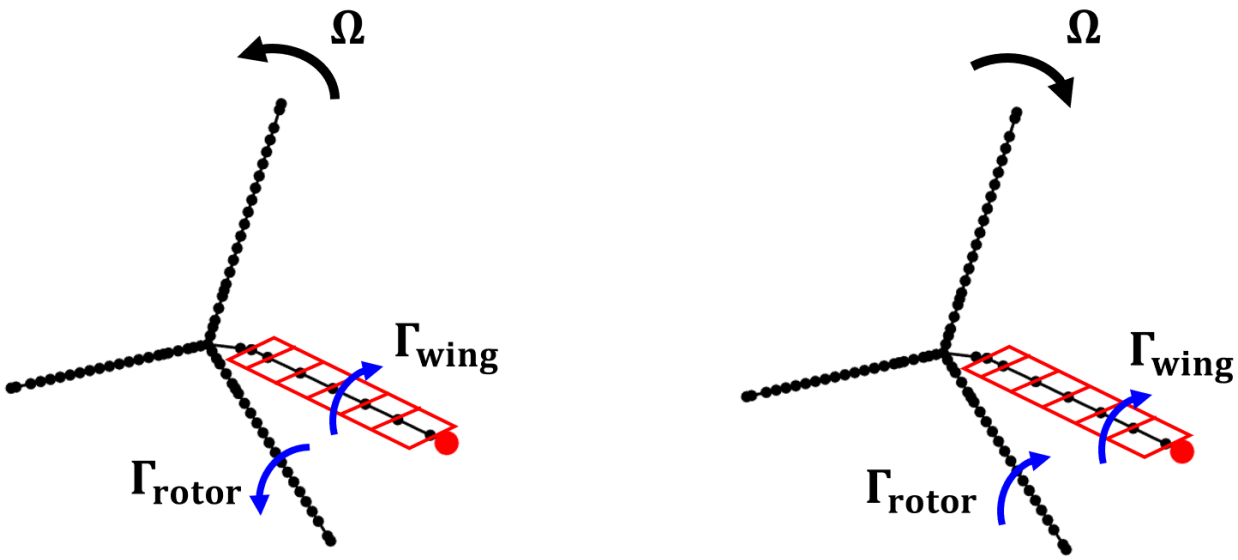


Figure 4.43: Diagram of rotor and wing bound circulation interaction.

The surface plot shows the strongest interaction around 50% of the wing span, the spanwise position of 48.9% is chosen to reduce the information to two dimensions. Figure 4.44 shows the difference in both wing angles of attack relative to the wing alone. A much stronger interaction is seen from the vortices shed from the clockwise rotor. This interaction pushes the wing into stall much faster than the other wing. The magnitude of the interaction increases as the rotor and wing generate more lift. The aircraft has two blades which is why two peaks are seen.

All of these details finally culminate to predicting the thrust and power of the quad biplane. Recall the objective is higher fidelity performance predictions to more accurately design a 50 lb hybrid-electric quad biplane tailsitter. One question remains; is it sufficient to simplify the model to a single rotor-wing pair and apply the results to the entire aircraft, or is it necessary to model the rotors and wings together?

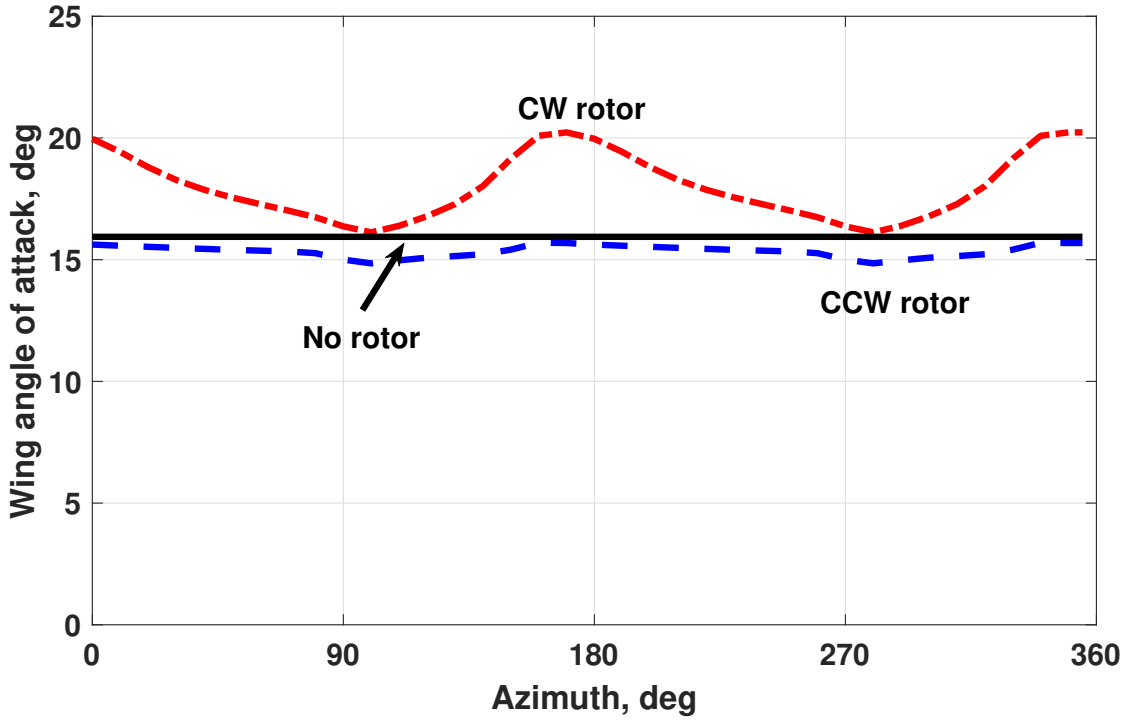


Figure 4.44: Wing angle of attack at 48.9% span. No wing (solid), wing at $\alpha = 4^\circ$ (dashed), wing at $\alpha = 12^\circ$ (dot-dashed).

Recall the L/D predictions of Fig. 4.4. The XV-15 data is removed to de-clutter and predictions using UMARC-II are added in Fig. 4.45. It is clear that the simple analysis, even with all its ad hoc calibration, is still inadequate. It significantly overpredicts the efficiency of the aircraft at lower speeds. At 91% rotor RPM it actually underpredicts L/D. A comprehensive analysis is needed. For the most part, the partial model of a single rotor and wing is sufficient to accurately predict the L/D. The velocity for best range is identifiable by modeling a single rotor and wing. However, as the aircraft approaches stall at low speeds, modeling the clockwise rotor becomes important as it accelerates the transition into stall. Then, a full model of the aircraft is needed.

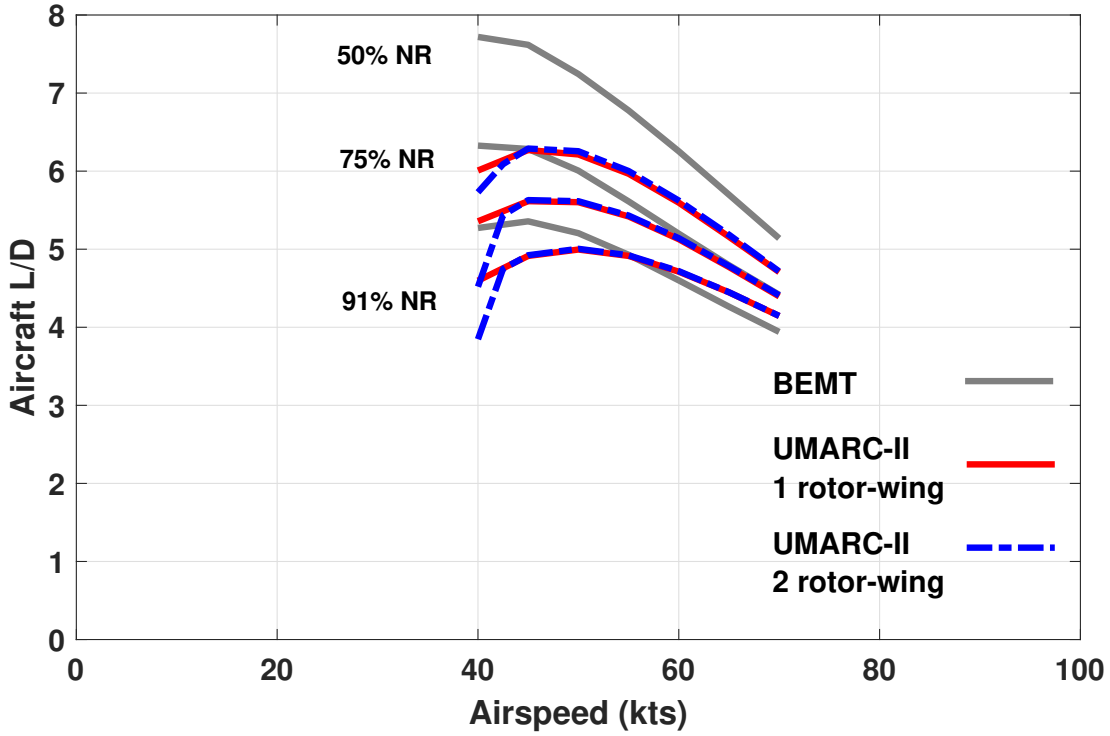


Figure 4.45: L/D prediction of quadrotor biplane aircraft. UMARC-II 1 rotor-wing CCW, 2 rotor-wing CCW+CW.

4.6 Chapter summary and conclusions

This chapter detailed the build up of analytical tools necessary to assess the performance and dynamics of an electric or hybrid-electric configuration. It covered simple analysis, detailed analysis, and a series of systematic validations.

A simple blade element analysis was used for initial predictions of power and L/D for a 50 lb quad biplane. The in-house comprehensive analysis UMARC-II is expanded significantly for multi-rotor, multi-wing calculations with free wake interaction and flexible rotors and wings. These refinements were validated with experimental data from several wind tunnel tests at NASA and UMD. UMARC-II was then used to understand rotor-wing dynamic and aerodynamic interactions. Finally, UMARC-II was used to predict power and L/D of the same aircraft, and was compared to the predictions from simple analysis. Based on this chapter, several key conclusions are drawn.

1. A simplified aircraft model is not adequate for performance calculations of a multi-rotor prop driven rotorcraft. It can overpredict L/D by up to 40% and it will miss stall. Structural loads are crucial to such aircraft which also requires interaction of wake.

2. The refined rotor-wing model using comprehensive analysis is critical to accurately predicting power required in forward flight. The model must include free wake, high fidelity airloads to the highest extent possible, and flexibility of the rotor and the wing through finite element models. A partial geometry — half wings and rotors — can be used before wing stall. For speeds approaching wing stall, the full geometry is needed.

3. When a rotor is mounted on a wing, wing aerodynamics are important to model for accurate blade and hub loads.

4. When a rotor is mounted on a wing, the tip vortices trailed from the rotor are strengthened if the direction of rotation is the same as the wing tip vortex. The vortices are weakened if the direction of rotation opposes the wing tip vortex. So the latter is desired to minimize wing induced power.

   The validated power and platform models are now ready to be integrated.

Chapter 5: Integrated power-platform

This chapter covers development and validation of a rotocraft sizing analysis to ultimately size a 50 lb hybrid-electric quad biplane. The engine model of Chapter 3 is integrated with the aircraft model of Chapter 4 to carry out a sizing analysis. In a sizing analysis, the mission and payload are specified and the minimum gross weight of the aircraft along with the engine power are predicted. Through the analysis, the answers to the two key questions are found. They are: (1) What is the optimal rotor speed reduction in cruise? and (2) how should this reduction be accomplished?

5.1 Rotorcraft sizing

Sizing calculates the gross weight of the aircraft given a mission profile and a specified payload. A typical flowchart for sizing calculation is shown in Fig. 5.1. The key elements are calculation of rotor and powertrain performance, component empty weights, and fuel burn throughout the mission.

The mission is specified then the configuration is specified. Several key parameters are specified based on the configuration. For a rotor, these include number of blades, disk loading, tip speed, rotor solidity, airfoils and blade structural properties; for a wing, these include wing loading, aspect ratio, airfoils, and structural properties. Gross weight is initialized. Based on this gross weight, and basic rotor and wing dimensions that fall out of the specified parameters, power is calculated followed by weights. The calculated weights update the initial weight, which updates the vehicle dimensions and

the cycle iterates.

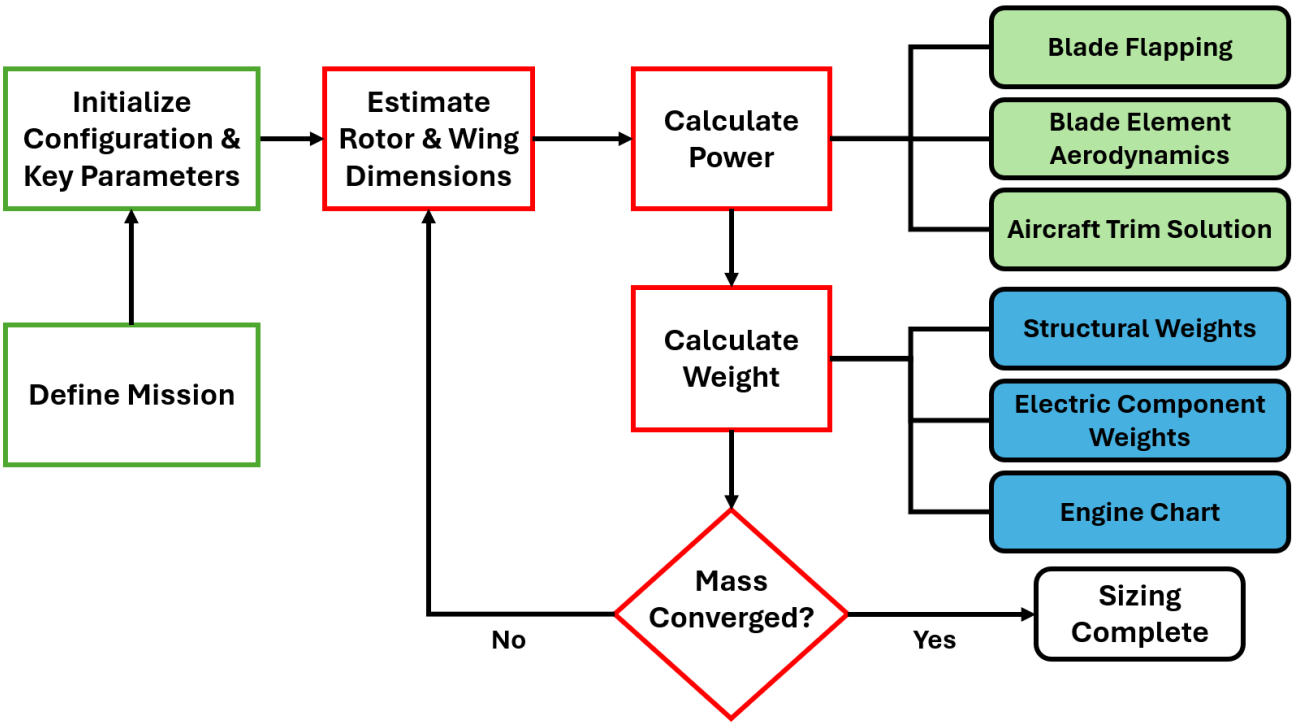


Figure 5.1: Flowchart of sizing methodology.

Calculating power accurately requires blade motion, airloads, free wake, and a trim solution. In the previous chapter, it was made clear that comprehensive analysis is necessary to accurately predict the performance.

Calculation of weights is difficult and rely on historical regression models or data from successful full-scale flight test articles. Weight calculations are separated into two groups. The structural weights are calculated from weight models developed by the Army. The electrical component weight models are developed in-house. Throughout this chapter, the word "weight" is used to stick to convention although "mass" is the true variable.

5.2 Breakdown of Sizing Framework

First, the mission profile must be defined. The mission is specified as mission segments, e.g. hover, climb, cruise, etc. The altitude, temperature, and duration of each segment is specified. The desired cruise speed is specified for best range, best endurance, or may be fixed. If best range or endurance is desired, this speed will change throughout the iterations. All of the mission inputs are initialized into a single structure/object.

The configuration is defined as a collection of group weights. Each group is initialized as its own object in the code. The groups are listed in Table 5.1. The group of particular importance in this work is the propulsion group. It specifies engine SFC and weights, electric motor/generator efficiencies and weights, cooling systems and overhead for the electrical systems, and plumbing/wiring. It also specifies the type of propulsion system. The options are: piston engine, piston-electric, turbine, battery, or hydrogen fuel cell.

Table 5.1: Group structures in rotorcraft sizing analysis.

Aircraft	Rotor	Tiltrotor/Tiltwing Wings	Empennage	Hydraulics
Mission	Propulsion	Nacelle & Air Induction	Fuselage	Alighting
	Fixed Wings	Fixed System Equipment	Flight Controls	Anti-Icing

The gross weight and hover Figure of Merit are initialized. From initial inputs, the initial rotor, wing, and fuselage dimensions are calculated. Next, the power required in each mission segment is calculated. Power calculations can use several options – momentum theory, hover BEMT, or lifting-line comprehensive analysis (maximum fidelity). The required engine power in each segment is then calculated from the rotor's power requirements. This consists of stepping through component efficiencies determined by the type of propulsion system. Then, the specific engine operating point, in

RPM and torque, is calculated for each mission segment. This step is crucial as different modes of engine control change the engine operating point to supply the power required to the rotor. From the maximum continuous power required, the installed power is calculated. The installed power is the maximum continuous power multiplied by a specified factor.

The Army Aeroflightdynamics Directorate (AFDD) weight models are used for all groups [37] except for the small scale engine, electric motors, and power inverters. The weight models for these components were developed in-house from commercially available data. These regression models are based on Mills [26]. The equation for the engine weight is given in Eq. 5.1, electric motor weight in Eq. 5.2, and inverter weight in Eq. 5.3. The data and model are shown in Figs. 5.2, 5.3, and 5.4. For all models, weight is returned in kg.

$$W_{Eng} = \begin{cases} 0.2860\, P^{1.3015} & P \leq 30\,\text{kW} \\ 1.1012\, P^{0.9785} & P > 30\,\text{kW} \end{cases} \tag{5.1}$$

$$W_{EM} = \begin{cases} 0.2519\, Q^{0.5857} & Q \leq 13\,\text{N-m} \\ 0.1062\, Q^{1.0422} & Q > 13\,\text{N-m} \end{cases} \tag{5.2}$$

$$W_{Inv} = \begin{cases} 0.04972\, P^{0.7897} & \text{Air-cooled} \\ 0.46550\, P^{0.6188} & \text{Water-cooled} \end{cases} \tag{5.3}$$

Table 5.2 lists all weight functions currently available. The formulae for all functions are given in Appendix A. Once all of the weights are calculated, the design gross weight is updated from the previous iteration. The updated dimensions are recalculated and the cycle repeats until the gross weight

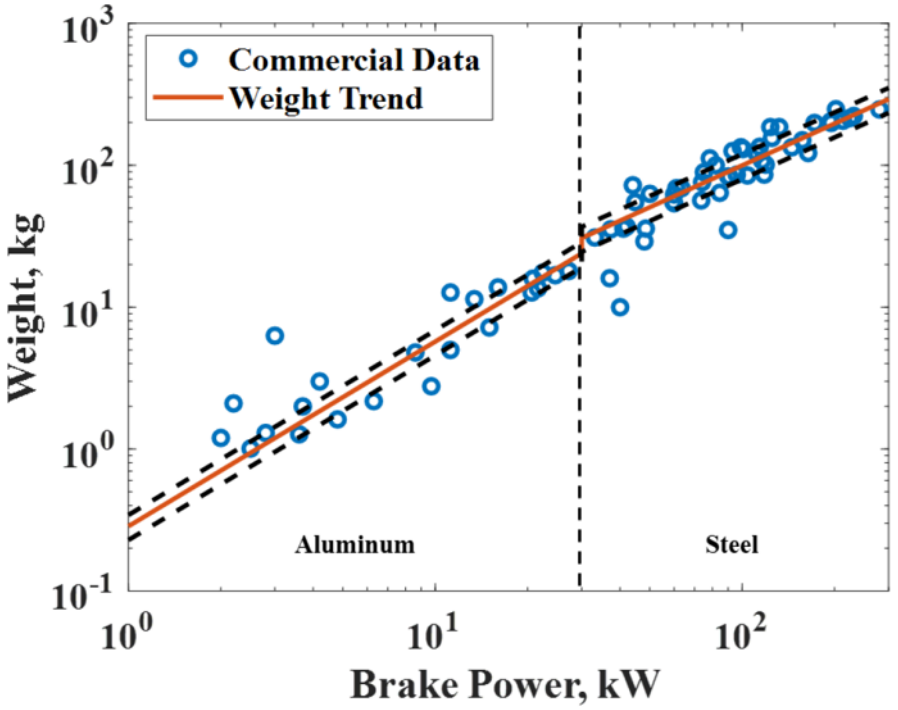


Figure 5.2: Engine weight model.

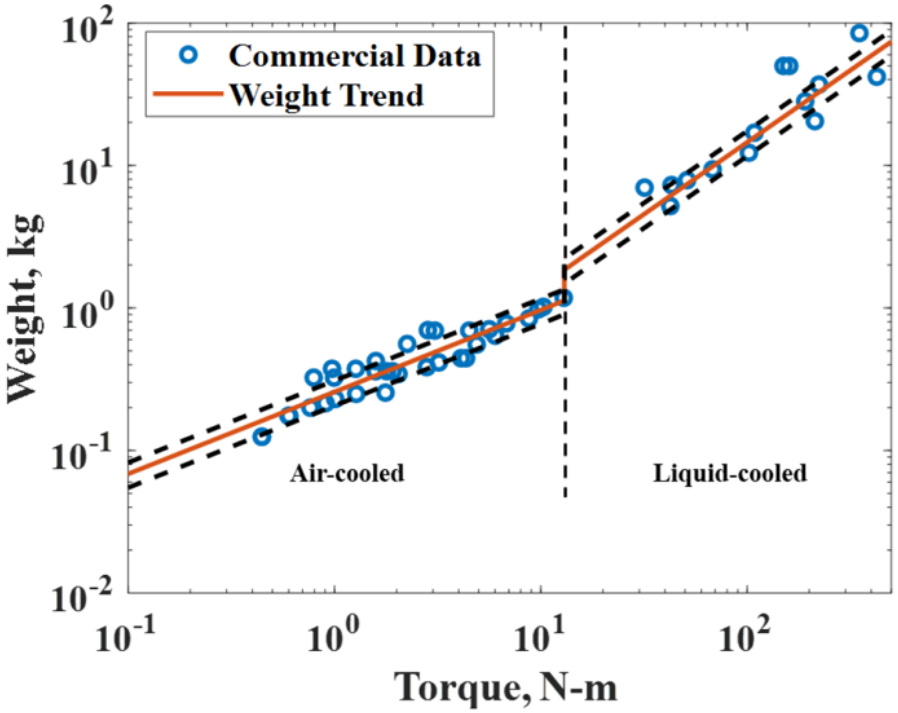


Figure 5.3: Electric motor weight model.

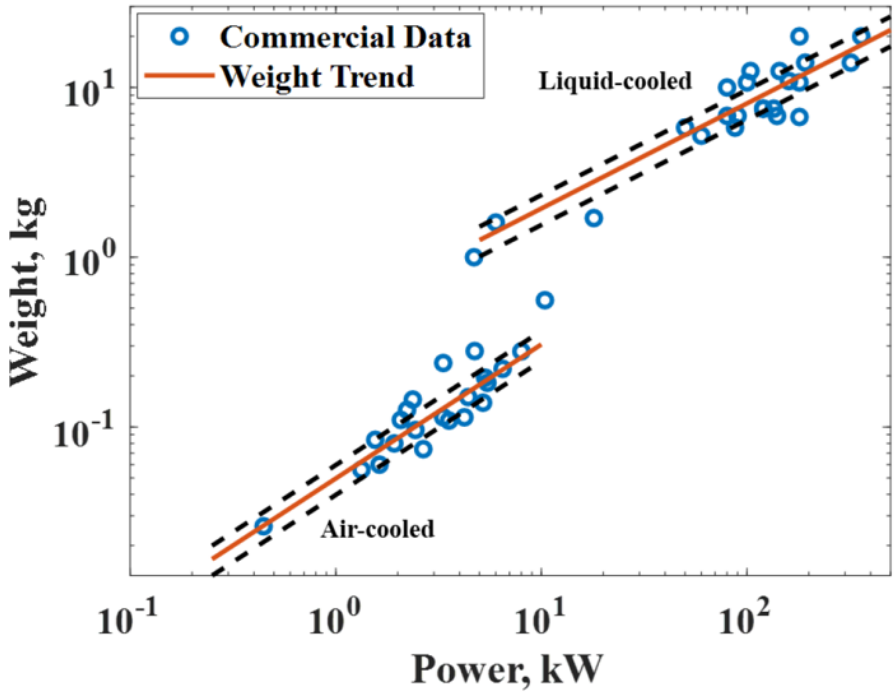


Figure 5.4: Inverter weight model.

converges.

Table 5.2: Group weight calculations in rotorcraft sizing analysis. Formulae given in Appendix A.

Rotor	Drive system	Fixed Wing
Propeller	Engine	Tiltrotor/Tiltwing Wing
Empennage	Generator	Nacelle & Air Induction
Fuselage	Electric motor	Flight Controls
Booms	Inverter	Hydraulics
Alighting	Battery	Anti-icing
Mission Fuel	Fuel cell	Fuel System

5.3 Validation with XV-15 Weights

A detailed weight breakdown of the XV-15 was obtained from NASA Ames and is used to validate the sizing analysis. Only the classical weight models are needed, without any hybrid-electric components. The blade element analysis is used for a crude estimate of performance. The technology

factors used match those reported in Ref. [38]. The actual weights are not published, however, a percent comparison is shown Table 5.3.

Table 5.3: Percent comparison of predicted weight groups relative to actual weight groups of the XV-15.

Wing	-2.76%
Blades	-3.21%
Hub & Hinge	+14.40%
Tail	-0.36%
Body	6.29%
Landing Gear	12.35%
Cowl	-0.29%
Nacelle (less cowl)	-0.33%
Spinner	-17.51%
Engines	-4.94%
Gearboxes + Rotor Drive	+0.24%
Drive Shafts	+3.53%
Propulsion Subsystems	-3.59%
Exhaust System	0.00%
Fuel Tanks	+10.14%
Fuel System Plumbing	+12.73%
Rotor Flight Controls (non-boost)	-3.66%
Rotor Flight Controls (boost)	+1.46%
Rotor Flight Controls Hydraulic Systems	-16.43%
Conversion System + Hydraulics	+8.22%
Fixed Wing Flight Controls + Hydraulics	-1.62%
Basic Airframe	+1.21%
Fuel	-3.06%
Design Gross Weight	**+0.48%**

The final predicted gross weight is within 0.5% of the actual design weight of the XV-15. Note that some differences are seen between the groups. The higher percentages are simply a result of low magnitude, e.g. actual weight of 5 lb and prediction of 4 lb leads to $+25\%$ error. The agreement between the predictions and data is satisfactory. The technology factors used will not be changed henceforth. The electric weight models are validated next.

5.4 Verification of Electric Weights

In the absence of any full-scale electric aircraft data, the models are verified with a conceptual design published by Johnson et al from NASA [30]. The conceptual aircraft is a battery powered quadcopter with disk loading of 2.5 lb/ft^2, payload of 250 lb, and cruise speed of 70 kts. The hover time is fixed to 5 min hover, and cruise reserve to 20 min. Similar to the XV-15, the equivalent flat plate area was approximated by $D/q = k\,(W/1000)^{2/3}$ but with $k = 2.95$ to account for the less aerodynamic body and boom structures. Additional technology factors for the electric weight models are provided in the study.

Results from different battery energy densities are compared. Figure 5.5 shows weight versus range capability. The current state-of-the-art in battery energy density is still less than 400 Wh/kg. The practical limitations of an all-electric quadcopter is glaring. Indeed, the range increases dramatically with increasing battery energy density. This trend, while yet to be confirmed by test data, is consistently predicted. The hover power of the quadcopter versus range is shown in Fig. 5.6. The trends are again consistent between predictions. With these, weight models for the electric components are also considered verified.

The conceptual quadcopter, however, was all-electric, i.e. powered only by the battery, not hybrid-electric. For that, we turn attention to our platform – the quadrotor biplane. There is no test data for such an aircraft, so the sizing is an excursion, relying only on pieces that are validated separately.

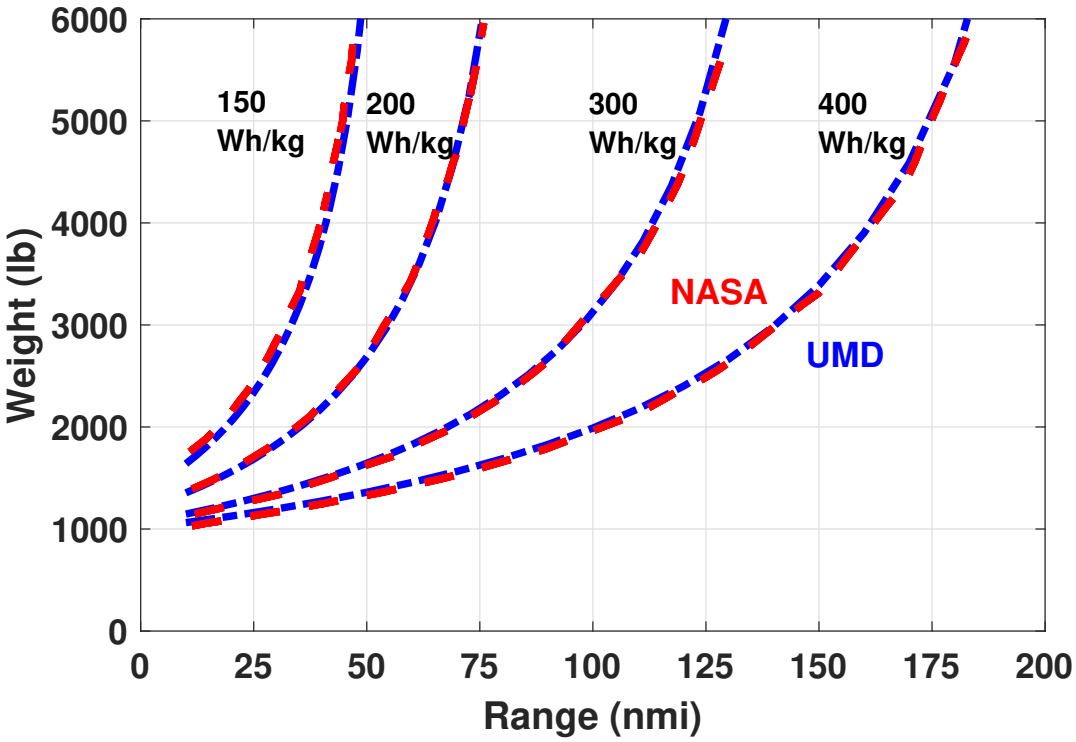


Figure 5.5: Gross weight prediction of NASA electric quadrotor.

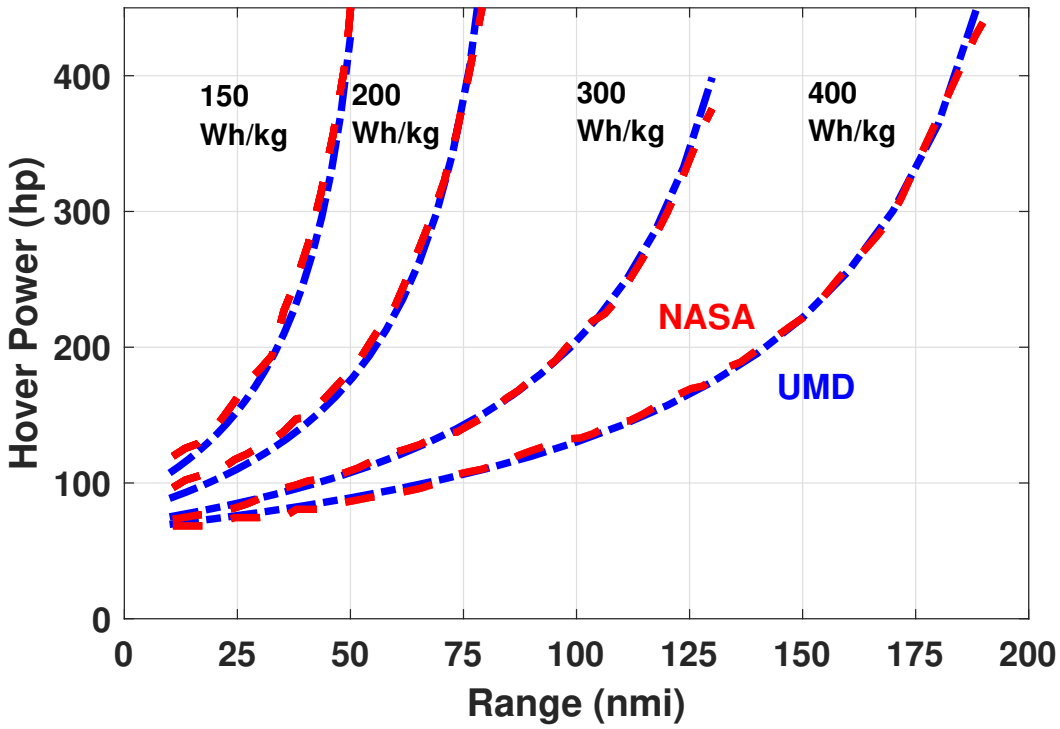


Figure 5.6: Hover power prediction of NASA electric quadrotor.

5.5 Sizing a Hybrid-Electric Quad-Biplane

With models verified and technology factors frozen, we turn to a quadrotor biplane tailsitter (QBiT) configuration. This study is anchored to the aforementioned conceptual design study [13]. The mission is kept deliberately simple as shown in Fig. 5.7. The target weight is 50 lb, to match the scale of the experimental work, the payload is 5 lb, and the cruise speed is fixed at 60 kts. The fixed aircraft parameters are shown in Table 5.4. These specific parameters are fixed so we can isolate the impact of the detailed SFC model. The weights of the powertrain components and fuel consumed are the core variables in this sizing study.

Rotor power and torque drive the weights of the engine and electric motors, respectively. A constant transmission efficiency of 85% is assumed based on the generator efficiency measured from the experiments.

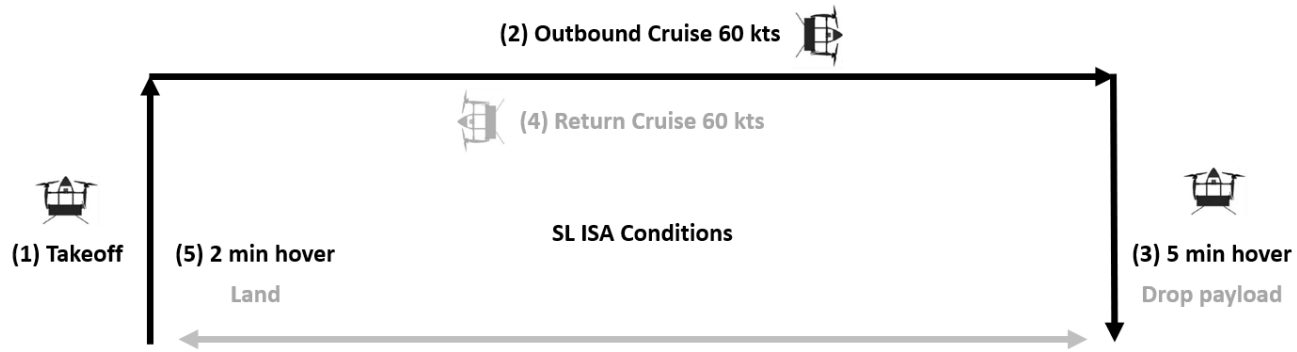


Figure 5.7: Sizing Mission; payload 5 lb, range falls out.

The rotor tip speed in hover is the nominal rotor tip speed (NR). Recall that reducing the tip speed in forward flight provides a dramatic increase in L/D from aeromechanics. But, the true impact of tip speed can only be determined in conjunction with engine performance. The benefits from increasing L/D can be negated by the engine if specific fuel consumption suffers. This means, at a certain tip speed, the aircraft may reach maximum L/D (minimum P/V), but if the engine becomes less efficient,

Table 5.4: Fixed aircraft parameters of the quadrotor biplane sizing study.

Rotors	4
Blades	2
Disk Loading	2.76 lb/ft^2
Solidity (per rotor)	0.1
V_{tip}	328 ft/s
Wings	2
Wing Loading	7.43 lb/ft^2
Wing Aspect Ratio	10

more fuel is required to deliver that power. To maintain the same gross weight, the extra fuel needed reduces the payload capability.

First, the true impact of tip speed reduction must be assessed. The predicted L/D of this aircraft at a fixed cruise speed of 60 kts is shown in Fig. 5.8 where the tip speed is reduced in cruise from 100% NR to 35% NR. Trim is achieved through collective control. The best L/D is achieved at 40% NR. The question now is, is 40% NR still the best reduction for integrated design when the engine SFC model is added?

Recall the engine model, redrawn in Fig. 5.9. The maximum engine speed, Ω_{max}, is set to 7400 RPM. This was the maximum engine speed of the 4-stroke engine previously tested and is similar to other engine's maximum speeds at this scale. Consider first, the engine speed sets the bus voltage and is assumed to follow the rotor speed i.e. if the rotor RPM is dropped to 50% NR, the engine RPM is also dropped to 50% NR. This method of control mimics how a mechanically connected engine would operate and serves as the baseline mode RPM reduction. Additional modes of RPM reduction are discussed later in Section 5.6. The maximum engine torque is calculated in each sizing iteration. The torque required from the engine is found for each mission segment. The maximum torque throughout the mission is limited to $90\%\, Q_{max}$. Because the maximum engine RPM is fixed, allowing the maximum torque to change is what allows the engine contour to scale with power.

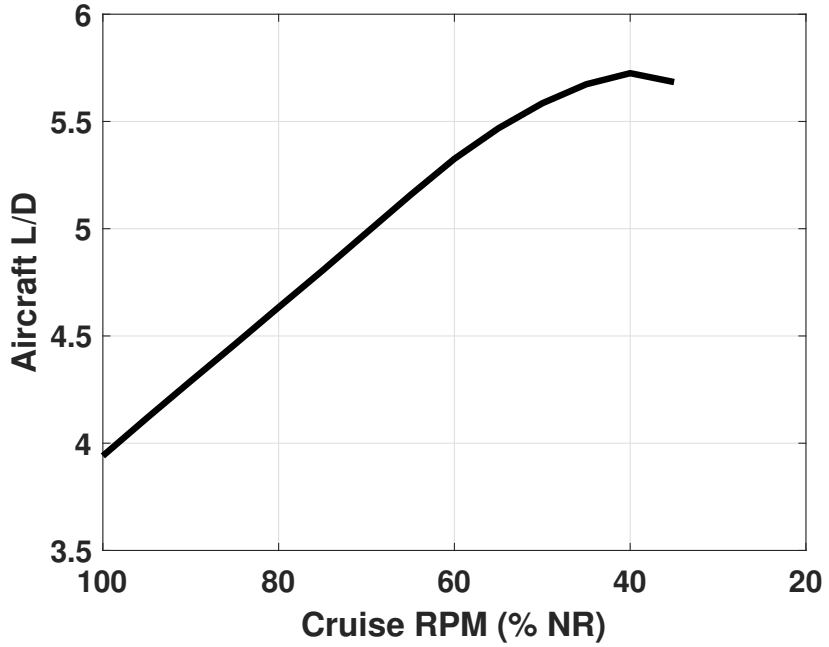


Figure 5.8: Quad biplane L/D versus tip speed reduction in cruise.

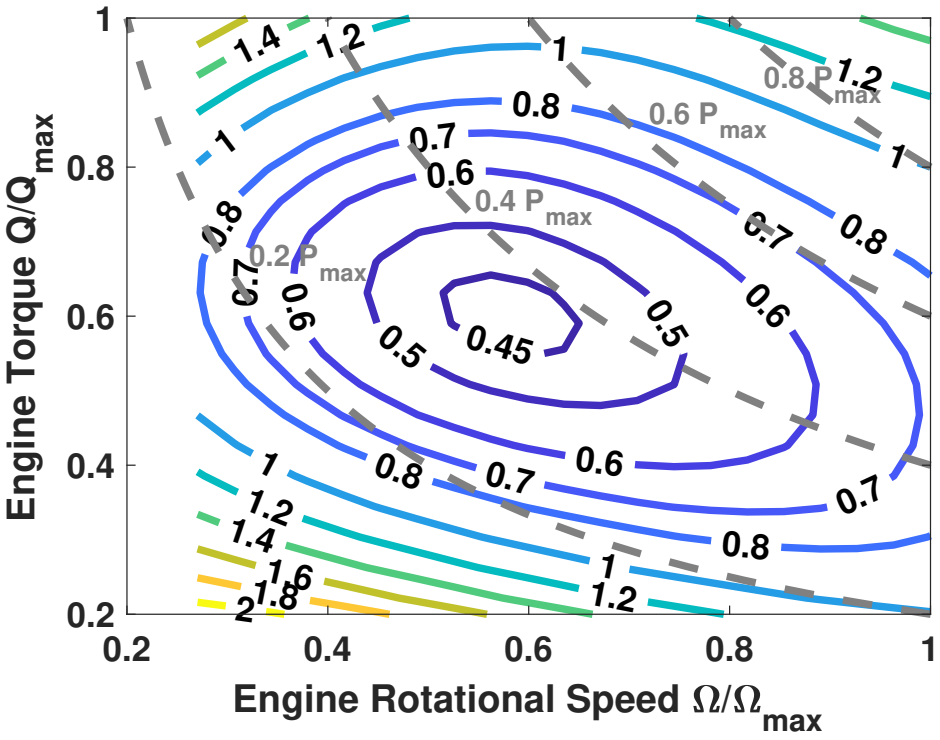


Figure 5.9: Engine SFC contour with constant power lines marked.

The aircraft is first sized with tip speed fixed to 100% NR, shown in Fig. 5.10. Then, the vehicle is sized assuming a cruise tip speed of 40% NR with the expectation of maximizing L/D, shown in Fig. 5.11. The detailed model shows RPM reduction to 40% NR in cruise increases gross weight despite higher L/D. For example, for 80 nmi range, the design gross weight is 80 lb for 100% NR and 90 lb for 40% NR. The increase in SFC more than offsets the gains from aircraft L/D through increase in fuel consumption. Additionally, the cruise torque becomes higher than hover which increases the size of the electric motors. The weights of the propulsion components and fuel consumed are quite sensitive to how the engine supplies the necessary power. Thus, aerodynamic performance must be considered together with engine performance and torque requirements.

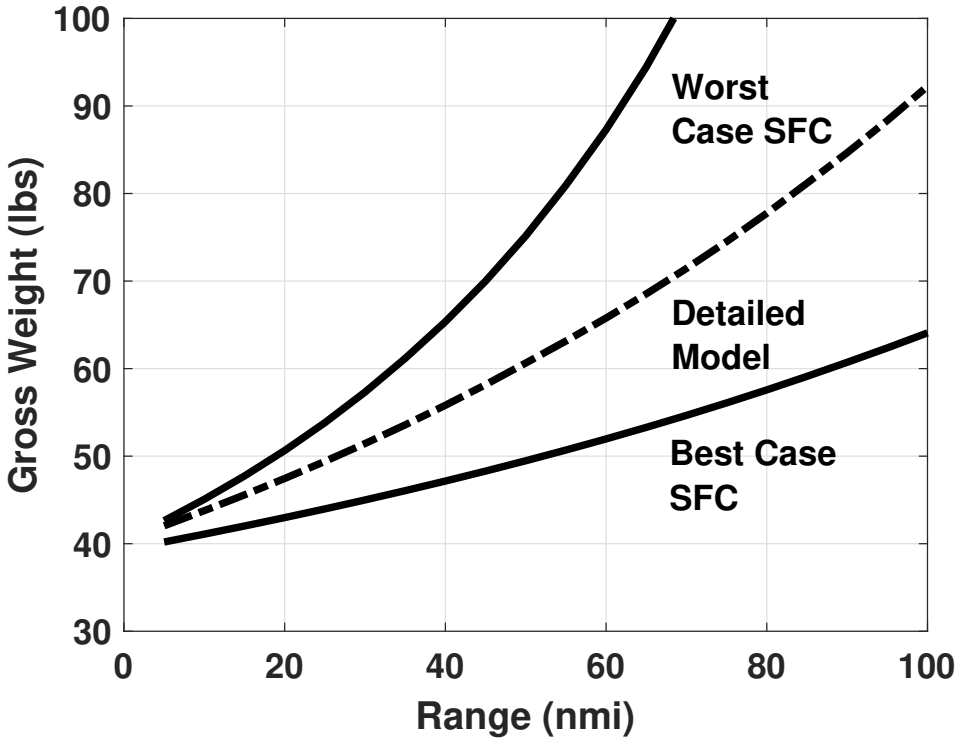


Figure 5.10: Cruise RPM = 100% NR.

A sensitivity analysis is performed by also sizing the aircraft assuming best-case and worst-case scenarios for engine SFC. The minimum gross weight is predicted with varying range for each case,

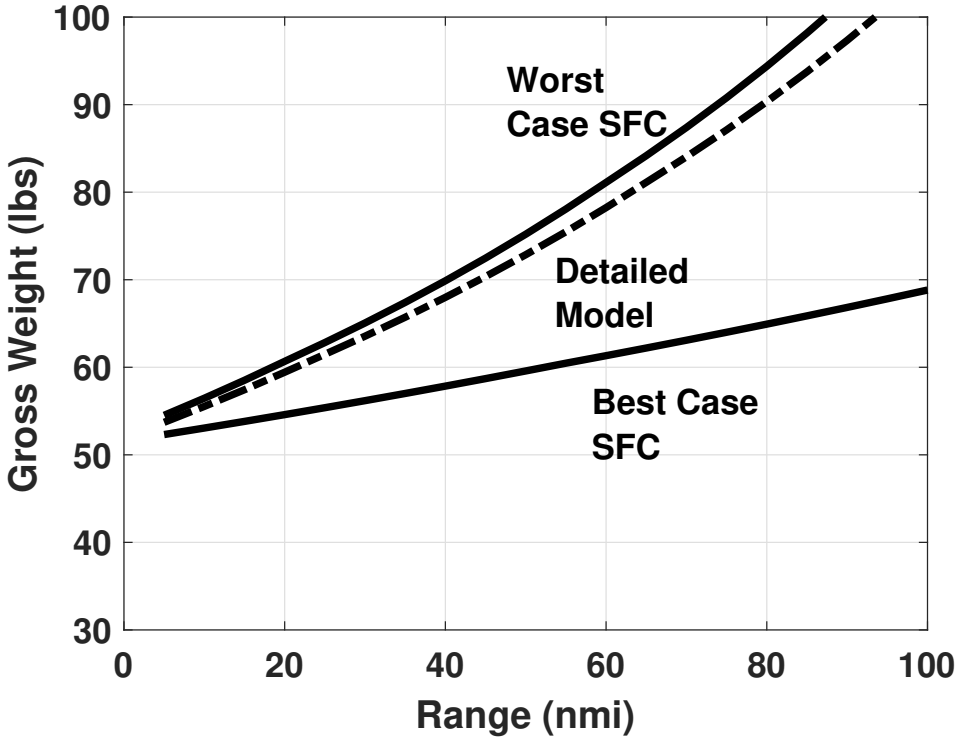


Figure 5.11: Cruise RPM = 40% NR.

also shown in Fig. 5.10 for 100% NR and Fig. 5.11 for 40% NR. The detailed model is clearly important for proper assessment of gross weight. Notably, if the cruise RPM is dropped to 40% NR, a 50 lb aircraft is not possible at all.

It is established that 40% NR, despite maximizing L/D, is not the optimal tip speed reduction. The aircraft is sized now by sweeping through cruise tip speed from 100% NR to 40% NR at a fixed range of 50 nmi. The gross weight is predicted for the three SFC cases as before. Figure 5.12 shows the gross weight versus cruise RPM. The weight is minimized until 70% NR with the detailed SFC model. These results also show the sensitivity to the engine model. But even when assuming a constant SFC, the tip speed reduction for minimum weight is still not 40% NR. This results from torque. As mentioned previously, as cruise RPM decreases, torque increases, driving up the electrical component weights. The key takeaway is that both isolated aerodynamic analysis and sizing analysis without a

detailed SFC model result in suboptimal design. The detailed SFC model is crucial to identify the minimum weight design.

The gross weight is predicted again for the same three cases now with the best tip speed reductions deduced from Fig. 5.12. These are shown in Fig. 5.13. The tip speed reduction for each of these three cases is different from one another; 55% NR for worst SFC, 60% NR for best SFC, and 70% for the detailed (i.e. correct) SFC. The predicted range for a 50 lb vehicle is about 37 nmi with the detailed SFC model. Otherwise, range falls anywhere between 20 nmi and 70 nmi, a massive gap that renders the conclusion meaningless.

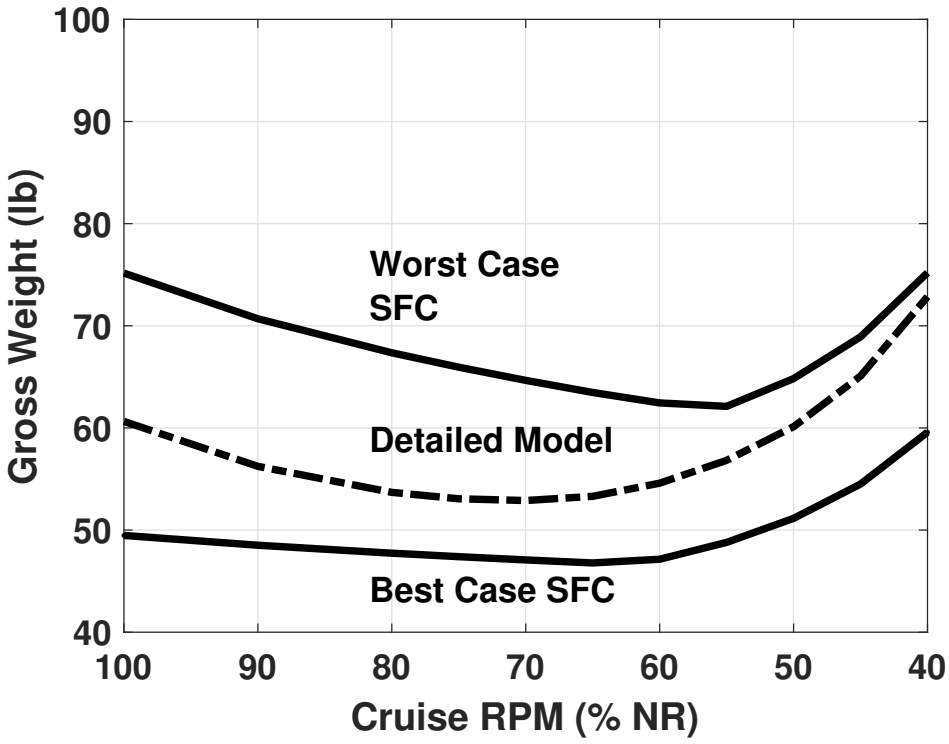


Figure 5.12: Gross weight versus tip speed reduction.

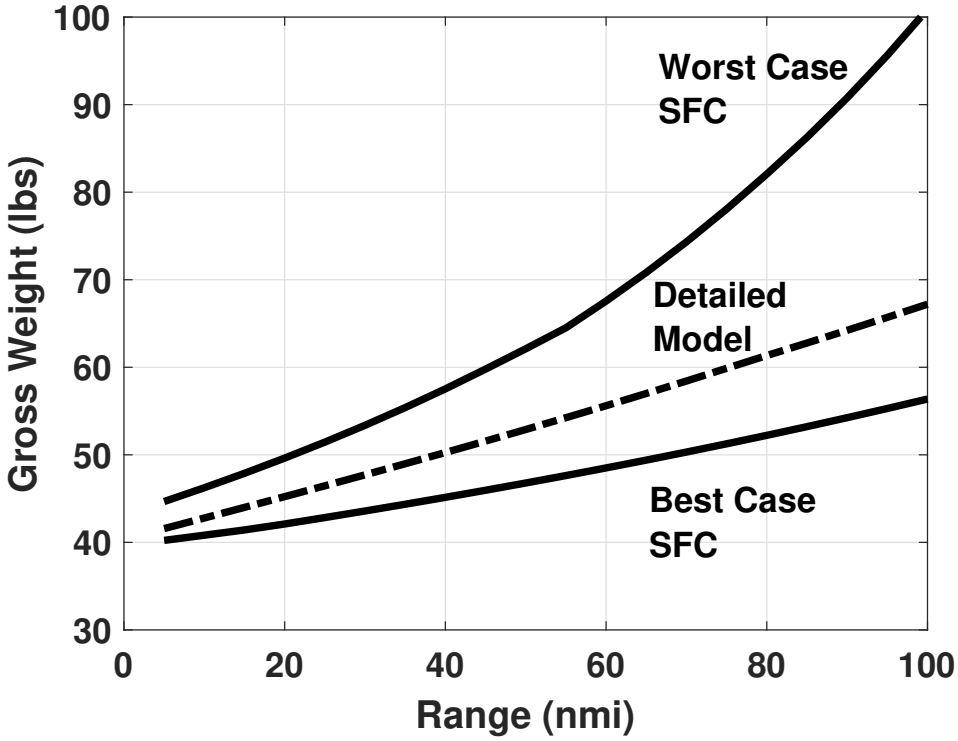


Figure 5.13: Weight versus range using best tip speed reduction.

5.6 Modes of RPM Reduction

So far it was assumed that the engine RPM was reduced proportional to rotor RPM, as if mechanically connected. This does not harness the true flexibility of the electric transmission. Are there more efficient modes of RPM reduction? Consider Fig. 5.14 where only one motor is shown for clarity. The rotor RPM and torque required will dictate the voltage and current drawn by the motor, respectively, which in turn will dictate the engine RPM and torque.

Consider three cases:

1. RPM Scaling: Engine RPM is proportional to the rotor RPM. This is the same case analyzed in the previous section.

2. Constant RPM: Engine RPM is fixed to the hover value.

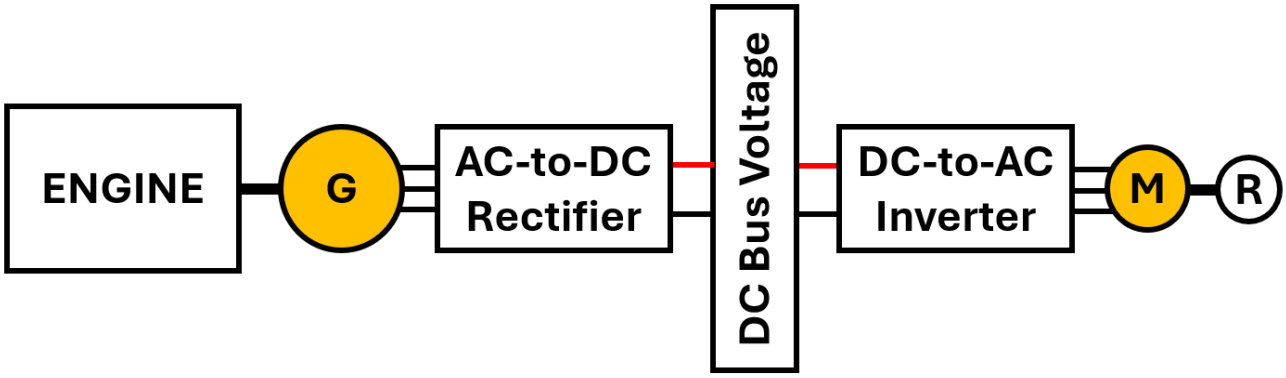


Figure 5.14: Simple schematic of power flow; G = generator, M = Motor, R = Rotor.

3. Minimum SFC: Engine RPM is independent of rotor RPM. The engine RPM is always selected to minimize SFC.

DC-to-AC inverters, also known as motor controllers, are capable of modifying the duty cycle of the control signal passed to the electric motors to reduce the mean voltage the motor receives, reducing RPM. Typically, they are designed to operate only as buck converters, not boost. The motor voltage could be made to exceed the bus voltage using a technique called field weakening. This is routine in ground vehicles. However, field weakening is meant to achieve higher speeds, not lower, as in our case. It reduces torque which is not what we need, so field weakening is neglected. A limit is set such that the bus voltage may not drop below the voltage the motors require.

The voltage of the signal from the controller controls the motor RPM, allowing the controller to adjust the rotor RPM independently of the engine as long as the voltage supply is greater than or equal to the voltage required of the motor. Of course, power is conserved through the controller so if the voltage is reduced through duty cycle, the current is increased. This is accomplished through a strategically sized combination of an inductor and a capacitor. When the signal is on, current flows to the load through the inductor generating a magnetic field and charging the capacitor. When the signal is off, the polarity of the inductor reverses and the magnetic field collapses, releasing the energy stored

in it as current while the stored charge in the capacitor ensures a constant voltage. In essence, the load is driven by the stored energy in the inductor and capacitor and not by the power source.

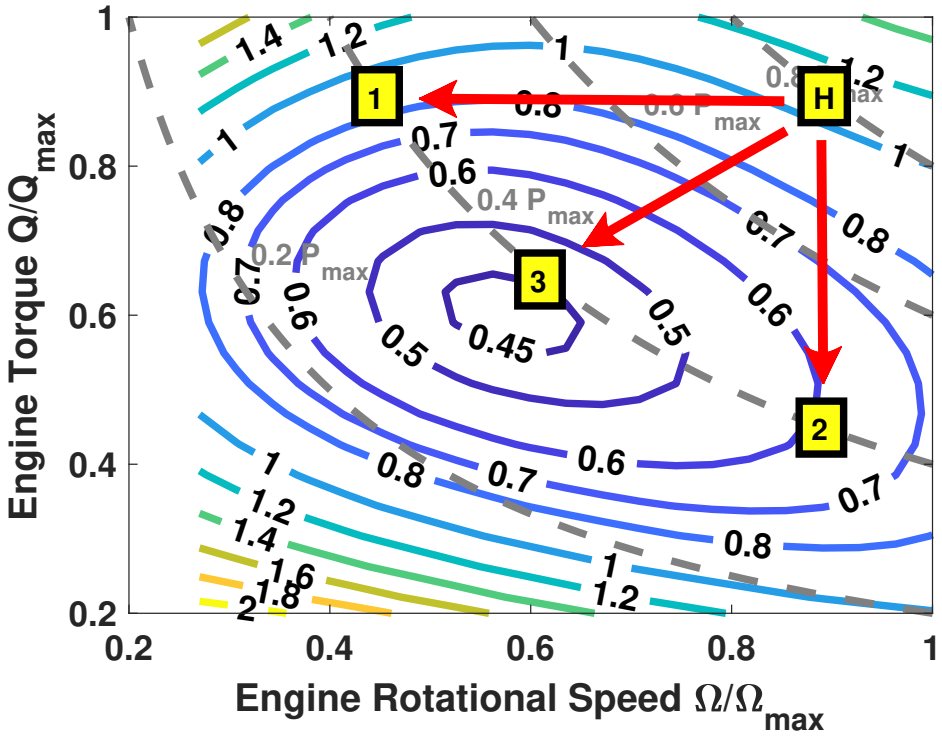


Figure 5.15: H: Hover; Case 1, 2, and 3, cruise conditions.

Consider an example illustrated in Fig. 5.15. For the sake of this illustration, consider the transmission efficiency to be 1. The engine is sized such that hover power is supplied at $0.9\,\Omega_{max}$ and $0.9\,Q_{max}$ resulting in an engine operating point at $0.81\,P_{max}$. Assume that the optimal cruise power for the rotors is half the hover power. To obtain this cruise power, say the rotor RPM is reduced by 50%. As RPM is directly related to voltage, the voltage is reduced by 50%. Since the engine power is directly proportional to the rotor power, the engine operating point in cruise must be somewhere along the constant power line at $0.4\,P_{max}$. In the case of RPM scaling, the engine RPM drops at the same rate as rotor RPM, resulting in half of the original engine RPM. In this case, the bus voltage is exactly what the rotor needs. Additionally, the torque required in cruise is equal to the torque in hover.

This constant torque operation falls out from this particular combination of power and RPM ratio and does not constrain the engine operating condition. In the case of a constant RPM, the bus voltage is much higher than the voltage the motor requires in cruise, thus the controller manages the rotor RPM and torque by reducing signal voltage and boosting the current. In the case of minimum engine SFC, the engine RPM is swept at the power required and the point of minimum SFC is determined. The resulting bus voltage is higher than the rotor requires so the controller, once again, reduces voltage and boosts current. In this case, the limit on RPM reduction of the engine equals the drop in rotor RPM. This is the limitation on bus voltage.

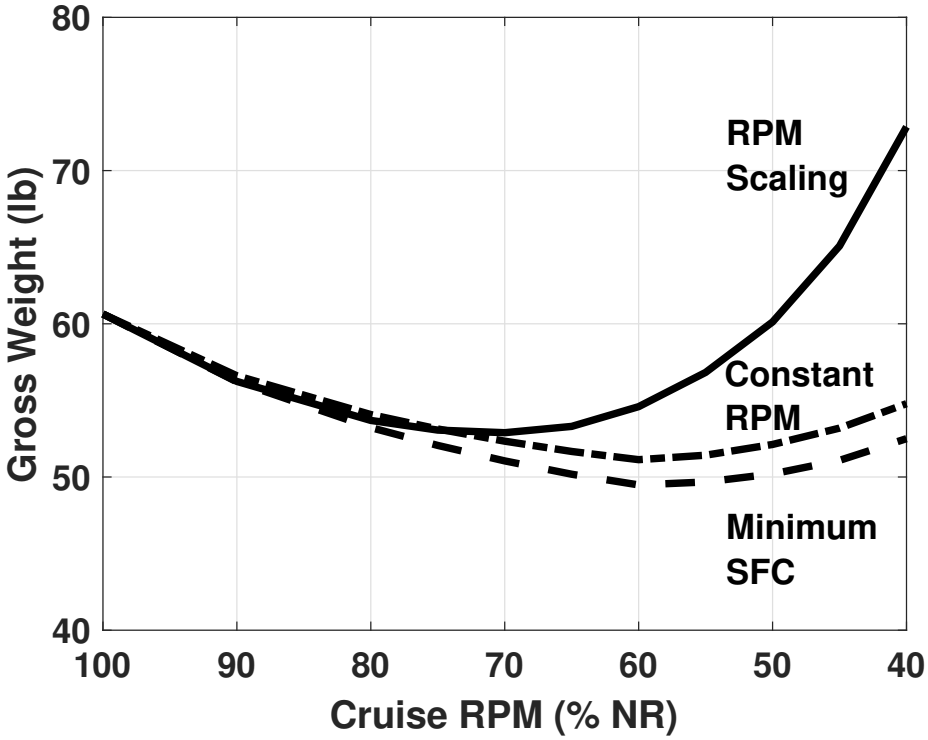


Figure 5.16: Impact of tip speed reduction on take-off weight.

To understand how each case impacts sizing we return to the design problem. Figure 5.16 shows the impact of tip speed on gross weight for a range of 50 nmi. All three cases use the detailed SFC model. The RPM scaling is the detailed SFC line of Fig. 5.12 earlier. While reducing the rotor tip

speed showed no benefit below 70% NR before, a benefit is seen for the other modes of engine RPM reduction down to 60% NR. Minimizing SFC is obviously the most effective way to minimize fuel burn and weight. This strategy achieves minimum fuel consumption and allows the motor controller to regulate voltage and current to the rotors appropriately. Operating at a constant engine RPM, which provides the simplest method of control, also displays a clear benefit with tip speed reduction. The voltage and current management come entirely from the motor controller. The best tip speed reduction for RPM scaling is 70% NR and the other cases are 60% NR.

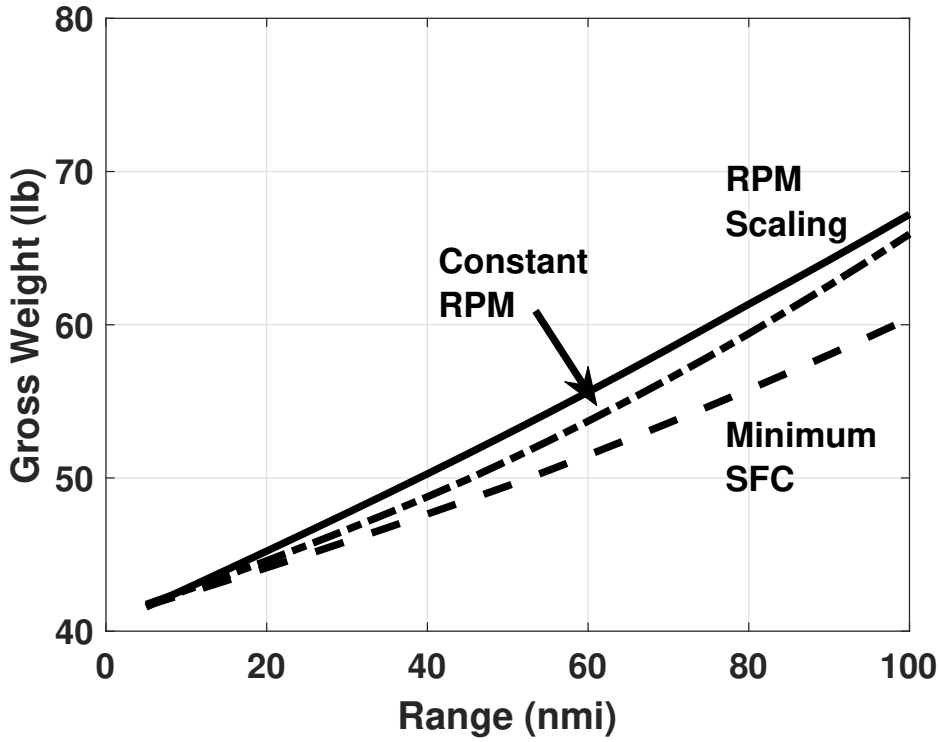


Figure 5.17: Sized vehicle take-off weight for different powertrain operating modes.

With the best tip speeds selected, the aircraft weight versus range for each case is shown in Fig. 5.17. The vehicle range now varies from 37 nmi to 53 nmi depending on how the engine is controlled. This is a smaller variation but important nevertheless. Managing the engine speed to operate at minimum SFC and using the motor controller to manage rotor speed achieves the highest

operational radius of 53 nmi for a 50 lb vehicle. Fixing the engine RPM greatly simplifies the control scheme but reduces range to around 45 nmi. Dropping the engine RPM at the same rate as the rotor RPM may simplify the control scheme but is the worst of all and results in the lowest range of around 37 nmi. Thus we conclude, the engine RPM should be independently controlled from the rotor RPM to minimize the net fuel consumption at the required power output. Then, the motor controllers are responsible for manipulating that power and supplying the correct voltage and current to the rotors. The empty weight fraction calculated is about 0.82 for all cases but fuel consumption makes the key difference. The $L/D \approx 4.5 - 5.0$. The three operating modes are summarized in Table 5.5.

Table 5.5: Summary of engine operating modes to reduce rotor tip speed in cruise.

Operating Mode	Constraints	Free Parameter(s)	Complexity	Range Difference (%)
RPM Scaling	Engine RPM follows rotor RPM	Rotor RPM	Baseline	0%
Constant RPM	Engine RPM fixed to hover	Rotor RPM	Less complex	+16%
Minimum SFC	Minimum bus voltage defined by baseline	Rotor RPM Engine RPM	More complex	+43%

5.7 Chapter Summary and Conclusions

This chapter brought the power and platform together to size a hybrid-electric aircraft. The answers to the key questions were found along with many other subtle but important conclusions.

A sizing analysis was developed for a quadrotor biplane tailsitter unmanned air vehicle. It was validated with XV-15 weights and verified with a NASA conceptual eVTOL. A 50 lb aircraft was sized and a sensitivity analysis conducted. Several methods of engine control to meet the rotor operating torque and speed combinations were detailed and compared to one another in complexity and value.

Based on this work, the following key conclusions are drawn.

1. The reduction in tip speed for cruise must be judiciously selected to balance rotor performance with engine performance. Maximizing aircraft L/D based on rotor aerodynamics alone will not lead to minimum gross weight.

2. A detailed SFC map as a function of torque and speed is needed for proper sizing of VTOL aircraft where rotor RPM is a key performance parameter.

3. Without an engine SFC map that captures the variation in speed and torque separately, optimal tip speed reduction in cruise - a key attribute and benefit of distributed propulsion - is predicted incorrectly during sizing. Aerodynamics alone suggest an optimal tip speed reduction of 40% NR whereas the true reduction to minimize gross weight is around 60%-70% NR.

4. Without a detailed SFC model, maximum range for a given gross weight is predicted incorrectly by sizing. For example, for a 50 lb aircraft, ranges from 20-70 nmi may be predicted using best-case and worst-case assumptions for engine SFC, whereas the correct range is 37 nmi. Thus, errors of 50-100$\%$ in range prediction may occur.

5. Reduction in rotor tip speed should not be carried out by motors alone. The engine should also be controlled independently to minimize the fuel consumed at the desired power output. Complexity is added to the control scheme, but significant operational gains can be attained.

6. The maximum range 50 lb aircraft is designed by operating the engine at minimum SFC for a desired power output. For this vehicle, the gross weight is very sensitive to increases in SFC, despite increases in L/D. The range of the 50 lb vehicle is extended by 43% relative to the baseline control configuration of matching the engine and rotor speed changes. Other options

are possible that trade complexity for capability but minimum weight is achieved by operating at minimum SFC at a desired power within bus voltage limitations.

Chapter 6: Summary and Conclusions

This research developed a fundamental understanding of a hybrid-electric powerplant for an unmanned rotorcraft powered by proprotors through model testing and comprehensive analysis. The key questions answered were by how much should the rotor tip speed be reduced in forward flight and by what mechanism? The correct answers were shown to be crucial to establish the payload, range, and gross weight of such aircraft. These answers could not be found without detailed engine-generator fuel consumption data, and without its inclusion in a detailed comprehensive analysis of such aircraft. This dissertation filled these gaps — in a small scale within the resources available.

In Chapter 2, a 3.43 kW 4-stroke piston engine was coupled to a generator and rectifier to acquire basic data on power generation and engine specific fuel consumption. The isolated engine, generator, and coupled engine-generator efficiencies were characterized.

Then, in Chapter 3, a powertrain efficiency model was synthesized and validated, and partly calibrated, from the data. The model predicted engine specific fuel consumption as a function of engine torque and speed in a non-dimensional form. Thus, the model was rubberized for quantifying variations in engine efficiency with operating torque and speed in a scale-invariant manner. The model captures sensitivities to the engine operating conditions.

In Chapter 4, an in-house comprehensive analysis University of Maryland Advanced Rotorcraft Code II (UMARC-II) was significantly expanded to support the analysis of unique design elements

of hybrid-electric aircraft. These refinements were validated with data from several wind tunnel test campaigns of the full-scale 26-ft diameter Boeing proprotor (M222), and the model-scale 4.75-ft diameter Maryland Tiltrotor Rig (MTR). UMARC-II was then used to understand rotor-wing dynamic and aerodynamic interactions, and was used to predict the power, L/D, and rotor torque and speed of a 50 lb quadrotor biplane. It was found that for a rotor mounted on a fixed wing generating lift, the oscillatory blade bending moments and the mean hub moments were amplified. The increase was proportional to how much lift the wing generated. Additionally, the wing aerodynamics were found to interact with the rotor aerodynamics in a way that accelerated the onset of stall at low speed for the quad biplane.

In Chapter 5, these quantities were coupled to the engine model through a rotorcraft sizing code. A rotorcraft sizing code was developed expressly to design electric and hybrid-electric VTOL. The aircraft was sized and a sensitivity analysis conducted to quantify the impact of engine specific fuel consumption assumptions. Once verified it was used to find the answer to the key question: by how much should the rotor tip speed be reduced? Next, several methods of engine speed control to meet the rotor operating torque and speed combinations were explored, compared to one another in complexity and value, and the best mechanism to reduce the rotor tip speed proposed. Thus, the key questions were answered.

6.1 Conclusions

Throughout this work, many new conclusions were drawn. They are all summarized here. The order is determined by appearance in the dissertation, not by importance, although the reader by now should be able to discern the most important ones.

1. Isolated engine specific fuel consumption and generator efficiencies are not adequate on their own; the coupled engine-generator efficiency is essential to accurately represent the behavior of the system and its impact on aircraft design.

2. The specific fuel consumption is a strong function of both voltage and current, not just power. At a desired power, there can be a large number of feasible engine operating conditions. The designer must understand what combinations of voltage and current result in the lowest fuel consumption. At least for the present engine, at a desired power it is more efficient to operate at high current (high torque) and moderate voltage (moderate engine speed).

3. An operating condition can always be found to achieve a minimum specific fuel consumption. For the current rig, that condition is 1 kW of output electrical power at 25 V and 40 A.

4. For permanent magnet generators, current may be considered a proxy for engine torque and voltage a proxy for engine speed but only as long as the impact on voltage output due to ohmic losses is well understood. The engine speed to voltage conversion of the generator should not be assumed as ideal, especially at high current.

5. A third order function in engine rotational speed can be used to approximate the pumping losses typical of a 4-stroke piston-engine. The model can then reliably predict the trends in the engine space.

6. A simplified aircraft model is not adequate for performance calculations of a multi-rotor prop driven rotorcraft. It can overpredict L/D by up to 40% and it will miss stall. Structural loads are crucial to such aircraft which also requires interaction of wake.

7. The refined rotor-wing model using comprehensive analysis is critical to accurately predicting

power required in forward flight. The model must include free wake, high fidelity airloads to the highest extent possible, and flexibility of the rotor and the wing through finite element models. A partial geometry — half wings and rotors — can be used before wing stall. For speeds approaching wing stall, the full geometry is needed.

8. When a rotor is mounted on a wing, wing aerodynamics are important to model for accurate blade and hub loads.

9. When a rotor is mounted on a wing, the tip vortices trailed from the rotor are strengthened if the direction of rotation is the same as the wing tip vortex. The vortices are weakened if the direction of rotation opposes the wing tip vortex. So the latter is desired to minimize wing induced power.

10. The reduction of tip speed is the crucial new knowledge. The reduction in tip speed in cruise must be judiciously selected to balance rotor performance with engine performance. Maximizing aircraft L/D based on rotor aeromechanics alone will lead to erroneous gross weight, range, and payload.

11. A detailed specific fuel consumption model as a function of torque and speed is needed for engine input, not the typical power-based engine charts.

12. Without an engine specific fuel consumption model that captures the variation in speed and torque separately, optimal tip speed reduction in cruise — a key attribute and benefit of distributed propulsion — is predicted incorrectly. Whereas aerodynamics alone suggest an optimal tip speed reduction to 40% of hover (nominal RPM (hover), NR), the correct reduction to minimize gross weight is much higher around 60%-70% NR.

13. Without a detailed specific fuel consumption model, maximum range for a given gross weight

is predicted incorrectly by sizing. For example, for a 50 lb aircraft, ranges from 20-70 nautical miles may be predicted using constant engine specific fuel consumption, whereas the correct range is 37 nautical miles. Thus, errors of 50-100$\%$ in range prediction may occur.

14. Reduction in rotor tip speed should not be carried out by motors alone. The engine should be controlled independently to minimize the fuel consumed at the desired power output. Based on the resulting bus voltage, the motors then control the rotors to achieve the desired tip speed reduction. Complexity is added to the control scheme, but significant operational gains are attained.

15. The maximum range is obtained by operating the engine always at minimum specific fuel consumption for a desired power output. For this vehicle, the gross weight is very sensitive to increases in specific fuel consumption, despite increases in L/D. The range of the 50 lb vehicle is extended by 43% through independent engine and rotor control relative to the baseline control of matching the engine and rotor speed changes. Other options are possible that trade complexity for capability but minimum weight is achieved by operating at minimum SFC at a desired power within bus voltage limitations.

6.2 Contributions of Presented Research

The overall contributions of this research are summarized below.

1. A hybrid-electric powerplant with a 4-stroke engine was assembled and tested at the University of Maryland. The facility continues to be used by students.

2. Experimental data was acquired across the engine operating range in a repeatable manner. This

kind of data was hard to find in open literature prior to this work.

3. A detailed, semi-empirical engine specific fuel consumption model was developed using the data and non-dimensionalized with respect to maximum torque and speed. Thus, it is scalable, and applicable to rotorcraft sizing.

4. The in-house comprehensive analysis University of Maryland Advanced Rotorcraft Code II (UMARC-II) was significantly expanded from a single rotor and wing to multiple rotors and multiple wings. All are coupled aerodynamically through free wake. The rotor and the wing are coupled structurally through multiblade coordinates of the flexible finite element degrees of freedom.

5. Validation of UMARC-II was significantly expanded to include in-house proprotor data recently acquired (reported in Ref. [39], Boeing M222 rotor structural loads including effect of wing, and XV-15 like, albeit in small scale, power and L/D data with full rotor-wing interference.

6. A rotorcraft design code was written and validated. It is tailored to VTOL with electric, hybrid-electric, and fuel cell powerplants. Other powerplant models can be easily incorporated.

7. The first key contribution to knowledge was the answer to the question: by how much should the rotor tip speed be reduced? Aerodynamics alone suggest an optimal tip speed reduction to 40% of hover. The correct reduction to minimize gross weight is much higher around 60%-70% of hover.

8. The second key contribution to knowledge was the answer to the question: by what mechanism of engine and rotor control should the rotor tip speed be reduced? Reduction in rotor tip speed

should not be carried out by the electric motors alone. The engine should be controlled independently to minimize the fuel consumed at the desired power output; then the rotors should be controlled based on the resulting bus voltage to achieve the desired tip speed reduction. Complexity is added to the control scheme, but significant operational gains are attained.

6.3 Future Work

Future work should prioritize the following:

1. Controlled and at will power sharing should be explored with batteries from engine shut off/all batteries to battery-charging/all engine operations. This work is already underway as part of a companion dissertation by John Schmidt.

2. Wind tunnel testing should be carried out to investigate the V-shaped loads data, whether the shift is real, and why it occurs.

3. Comprehensive wind tunnel testing of rotors mounted on booms and wings should be carried out to acquire much needed test data. It should include detailed azimuthal structural loads in the rotating frame.

4. UMARC-II should be refined to allow for dissimilar control of each rotor in collective and cyclics. This would enable true analysis of independent rotor control flight conditions.

5. Finally, flight testing of a multi-rotor, multi-wing aircraft should be undertaken. Collection of power required versus speed provide the only source of true L/D data. This was the original vision behind the project — that Maryland explore the engine and US Government and Industry scale-up and integrate on the platform. It is time for Maryland to fill that gap on its own.

Appendix

All weight equations in the rotorcraft sizing code. The weight groups with a '*' are developed in-house, otherwise they come from Ref. [37]. Note that some weights are calculated using imperial units and others metric. Simple conversions should be used to standardize units following the weight calculation.

A technology factor, χ, is included with most weight equations to account for progression in materials development. It is the designer's responsibility to assess the current state of technology and apply an appropriate weight correction.

Rotors: The rotor group consists of all blades, hubs, fairings, spinners, and support structures. The blade weight calculation accounts for all blades of all rotors. If the rotors are dissimilar, N_{Rotor} should be set to 1 and blade weight for each rotor calculated separately.

Rotor blades:

$$W_{blade} = \chi_{blade}\, N_{Rotor}\, 0.0024419\, f_{tilt}\, N_b^{0.53479}\, R^{1.74231}\, c^{0.77291}\, V_{tip}^{0.87562}\, \nu_\beta^{2.51048}$$

Rotor hub:

$$W_{hub} = \chi_{hub}\, N_{Rotor}\, 0.0061182\, N_b^{0.20373}\, R^{0.60406}\, V_{tip}^{0.52803}\, \nu_{hub}^{1.00218}\, (W_{blade}/N_{Rotor})^{0.87127}$$

Rotor Fairing/Spinner:

$$W_{spinner} = \chi_{spin}\, N_{Rotor}\, 7.386\, D_s^2$$

Rotor Support Structure:

$$W_{supt} = \chi_{supt}\, N_{Rotor}\, f_{supt}\, W_{MTO}$$

Table 1: Rotor parameters

Parameter	Definition	Typical Value	Units
N_{Rotor}	Number of rotors		
f_{tilt}		1.17940 for tilting rotors 1.0 otherwise	
N_b	Number of blades		
R	Rotor radius		ft
c	Mean blade chord		ft
V_{tip}	Rotor tip speed in hover		ft/s
ν_{beta}	Natural frequency (flap)		per rev
D_{spin}	Spinner diameter		ft
f_{fold}	blade fold weight (fraction of total blade weight)	0.04 for manual fold 0.28 for automatic fold	

Empennage: The empennage is the tail assembly of a helicopter consisting of a boom, vertical, and horizontal stabilizers.

Empennage (Tiltrotor or Tiltwing) Horizontal and Vertical Tail:

$$W_{ht} = \chi_{ht}\, S_{ht}\, (0.00395\, S_{ht}^{0.2}\, V_{dive} - 0.4885)$$

$$W_{vt} = \chi_{vt}\, S_{vt}\, (0.00395\, S_{vt}^{0.2}\, V_{dive} - 0.4885)$$

Empennage (Helicopter or Compound) Horizontal and Vertical Tail:

$$W_{ht} = \chi_{ht}\, 0.7176\, S_{ht}^{1.1881}\, AR_{ht}^{0.3173}$$

$$W_{vt} = \chi_{vt}\, 1.0460\, f_{tr}\, S_{vt}^{0.9441}\, AR_{vt}^{0.5332}$$

Table 2: Empennage parameters

Parameter	Definition	Typical Value	Units
S_{ht}	Planform area horizontal tail		ft^2
S_{vt}	Planform area vertical tail		ft^2
AR_{ht}	Aspect ratio horizontal tail		
AR_{vt}	Aspect ratio vertical tail		
V_{dive}	Dive velocity at sea level		kts
f_{tr}		1.16311 if tail rotor located on vertical tail 1.0 otherwise	

Fuselage: The fuselage weight calculation includes the weight of the main structure, fold or retraction mechanisms for the wing, rotor, and/or tail as well as marinization, pressurization, and crashworthiness structure.

$$W_{basic} = \chi_{basic}\, 25.41\, f_{LGloc}\, f_{LGret}\, f_{ramp}\, (W_{MTO}/1000)^{0.4879}\, (n_z\, W_{SD}/1000)^{0.2075}\, S_{body}^{0.1676}\, l_{fuse}^{0.1512}$$

$$W_{cw} = \chi_{cw}\, f_{cw}\, W_{basic}$$

Table 3: Fuselage parameters

Parameter	Definition	Typical Value	Units
W_{MTO}	Maximum takeoff weight		lb
W_{SD}	Structural design gross weight		lb
S_{body}	Fuselage wetted area		ft^2
l_{fuse}	Fuselage length		ft
n_z	Design ultimate load factor for W_{SD}		g
f_{LGloc}		1.1627 if landing gear on fuselage 1.0 otherwise	
f_{LGret}		1.1437 if landing gear is retractable 1.0 otherwise	
f_{ramp}		1.2749 if there is a cargo ramp 1.0 otherwise	
f_{cw}	Crashworthiness weight (fraction of fuselage weight)	0.06	

Booms*: A simple equation is used to approximate the boom length based on the rotor geometry of a quadrotor. It is assumed that the boom length is the hypotenuse of a right triangle with a side length of the rotor radius. For other configurations, the length estimate can be easily modified. A simple cross section analysis should be done to approximate the mass/length. Thus,

$$l_{boom} = \sqrt{2}\, R$$

$$W_{boom} = N_{Rotor}\, m_{boom}\, l_{boom}$$

Table 4: Boom parameters

Parameter	Definition	Typical Value	Units
N_{rotor}	Number of rotors		
R	Rotor radius		m
l_{boom}	Boom length		m
m_{boom}	Mass per length of boom		kg/m

Alighting: Alighting, or landing gear, consists of the basic structure, retraction, and crashworthiness.

$$W_{LG} = \chi_{LG}\, 0.4013\, W_{MTO}^{0.6662}\, N_{LG}^{0.536}\, WL^{0.1525}$$

$$W_{LGret} = \chi_{LGret}\, f_{LGret}\, W_{LG}$$

$$W_{LGcw} = \chi_{LGcw}\, f_{LGcw}\, (W_{LG} + W_{LGret})$$

Table 5: Alighting parameters

Parameter	Definition	Typical Value	Units
W_{MTO}	Maximum takeoff weight		lb
WL	Wing loading		lb/ft^2
N_{LG}	Number of landing gear assemblies		
f_{LGret}	Retraction weight (fraction basic weight)	0.08	
f_{LGcw}	Crashworthiness weight (fraction basic + retraction weight)	0.14	

Mission Fuel*: The fuel consumed is calculated separately for each mission segment based on the power required and engine operating state. The engine model, in Chapter 3, is used to find the SFC at the engine operating state or the SFC in each mission segment is assumed. Then,

$$W_{fuelseg} = SFC_{seg}\, P_{seg}\, t_{seg}$$

Table 6: Mission fuel parameters

Parameter	Definition	Typical Value	Units
SFC_{seg}	Engine SFC of mission segment		kg/kW-hr
P_{seg}	Engine power required of mission segment		kW
t_{seg}	Time of mission segment		hr

Drive System: The drive system includes gearboxes, rotor shafts, drive shafts, and rotor brakes. The first formula approximates the weight of the gearboxes and rotor shafts together. The drive shafts are the intermediate shafts that transmit power in within the drive system.

$$w_{gbrs} = 95.7634\, N_{Rotor}^{0.38553}\, P_{DSlim}^{0.78137}\, \Omega_E^{0.09899} / \Omega_R^{0.80686}$$

$$W_{gb} = \chi_{gb}\,(1 - f_{rs})\, w_{gbrs}$$

$$W_{rs} = \chi_{rs}\, f_{rs}\, w_{gbrs}$$

$$W_{ds} = \chi_{ds}\, 1.166\, Q_{DSlim}^{0.3828}\, x_{hub}^{1.0455}\, N_{ds}^{0.3909}\, (0.01\, f_P)^{0.2693}$$

$$W_{rb} = \chi_{rb}\, 0.000871\, W_{blade}\, (0.01\, V_{tip})^2$$

Table 7: Drive system parameters

Parameter	Definition	Typical Value	Units
N_{Rotor}	Number of rotors		
N_{ds}	Number of intermediate drive shafts		
x_{hub}	Length of drive shaft between rotors		ft
PDS_{lim}	Rated power of drive system		hp
QDS_{lim}	Rated torque of drive system		hp/RPM
Ω_E	Engine speed		RPM
Ω_R	Main rotor speed		RPM
f_{rs}	Rotor shaft weight (fraction of gearbox and rotor shaft weight)	0.13 range 0.06 – 0.2	
f_P	Second rotor rated power (fraction of drive system rated power)	60 for twin rotors 15 for SMR + tail (18 if 2-bladed)	%
W_{blade}	Weight of rotor blades		lb
V_{tip}	Main rotor tip speed		ft/s

Engine*: The formula for the weight of one engine is developed from a regression fit of commercially available data [26].

$$W_{one\,eng} = \begin{cases} 0.2860\,P^{1.3015} & P \leq 30\,\text{kW} \\ 1.1012\,P^{0.9785} & P > 30\,\text{kW} \end{cases}$$

$$W_{eng} = \chi_{eng}\,N_{eng}\,W_{one\,eng}$$

$$W_{exh} = \chi_{exh}\,N_{eng}\,(K_{0exh} + K_{1exh}\,P)$$

$$W_{acc} = \chi_{acc}\,2.0088\,f_{lub}\,(W_{eng}/N_{eng})^{0.5919}\,N_{eng}^{0.7858}$$

Table 8: Engine parameters

Parameter	Definition	Typical Value	Units
N_{eng}	Number of engines		
P	Maximum engine power		kW
K_{0exh}	Engine exhaust weight versus power constant		
K_{1exh}	Engine exhaust weight versus power constant		
f_{lub}		1.4799 if accessory weight includes lubrication 1.0 if lubrication is included in engine weight	

One Generator/Electric Motor*: The formula for the weight of one generator or motor is developed from a regression fit of commercially available data [26]. Cooling system weight is included in the model.

$$W_{gen} = \begin{cases} 0.2519\,Q^{0.5857} & Q \leq 13\,\text{N-m} \\ 0.1062\,Q^{1.0422} & Q > 13\,\text{N-m} \end{cases}$$

Table 9: Generator/Electric motor parameters

Parameter	Definition	Typical Value	Units
Q	Maximum motor torque		N-m

One Inverter*: The formula for the weight of one inverter is developed from a regression fit of commercially available data [26]. Cooling system weight is included in the model.

$$W_{Inv} = \begin{cases} 0.04972\, P^{0.7897} & \text{Air-cooled} \\ 0.46550\, P^{0.6188} & \text{Water-cooled} \end{cases}$$

Table 10: Inverter parameters

Parameter	Definition	Typical Value	Units
P	Maximum rated power of controller		kW

Battery: Similar to fuel, the energy required for each mission segment is calculated separately. The assumed energy density of the battery is then used to find the weight.

$$W_{batt} = E_{seg}/\rho_{seg}$$

Table 11: Battery parameters

Parameter	Definition	Typical Value	Units
E_{seg}	Energy required in mission segment		J (W-s)
ρ_{seg}	Battery energy density		J (W-s/kg)

Fixed Wing:

$$W_{wing} = 5.66411\, f_{LGloc} \left(\frac{W_{SD}}{1000\, \cos \Lambda_{wing}} \right)^{0.847} n_z^{0.39579}\, S_w^{0.21754}\, AR^{0.50016} \left(\frac{1 + \lambda_{wing}}{\tau_{wing}} \right)^{0.09359} (1 - b_{fold})^{-0.14356}\, N_{wing}$$

Table 12: Fixed wing parameters

Parameter	Definition	Typical Value	Units
N_{wing}	Number of fixed wings		
W_{SD}	Structural design gross weight		lb
S_w	Wing planform area		ft^2
AR	Wing aspect ratio		
Λ_{wing}	Wing sweep angle		deg
λ_{wing}	Wing taper ratio (tip chord/root chord)		
τ_{wing}	Wing airfoil thickness-chord ratio (t/c)		
n_z	Design ultimate load factor for W_{SD}		g
b_{fold}	Fraction wing span that folds	0 to 1	
f_{LGloc}		1.7247 if landing gear on wing 1.0 otherwise	

Tiltrotor/Tiltwing Wing: The weight of a tiltrotor wing is separated into two parts: the primary weight calculations and the intermediate calculations necessary. The primary driver of wing sizing is torsional stiffness The primary weight calculations follow.

$$W_{ext} = \chi_{ext}\, S_{ext}\, U_{ext}$$

$$W_{efold} = \chi_{efold}\, f_{efold}\, W_{ext}$$

$$W_{tip} = \text{Total weight at the wing tip}$$

The weight of the primary structures is found from thee weight of the torque box and wing spar.

$$W_{box} = A_{tb}\,\rho_{tb}\,b_w/e_{tb}$$

$$W_{spar} = C_t\,A_{sp}\,\rho_{sp}\,b_w/e_{sp}$$

$$w_{prim} = W_{box} + W_{spar}$$

$$W_{prim} = \chi_{prim}\,w_{prim} + W_{ext}$$

Next, the weight of the wing fairings, controls surfaces, fittings, and folding/tilting mechanisms are found.

$$W_{fair} = \chi_{fair}\,S_{fair}\,U_{fair}$$

$$W_{flap} = \chi_{flap}\,S_{flap}\,U_{flap}$$

$$w_{fit} = \chi_{fit}\,f_{fit}\,T_{cap}$$

$$W_{fold} = \chi_{fold}\,f_{fold}\,\left(W_{prim} + W_{fair} + W_{flap} + W_{fit} + W_{tip}\right) + W_{efold}$$

Table 13: Tiltrotor/Tiltwing wing parameters - primary

Parameter	Definition	Typical Value	Units
S_{ext}	Area of wing extension (b_{ext} times mean c_{ext}		ft^2
U_{ext}	Unit weight of wing extension		lb/ft^2
f_{efold}	Wing extension fold/tilt (fraction extension weight)		
W_{tip}	Weight at wing tip		lb
M_{tip}	Mass at wing tip		slug
f_{tip}	W_{tip}/W_{SD}		
W_{box}	Weight of torque box		lb
W_{spar}	Weight of wing spar		lb
A_{tb}	Cross-sectional area of torque box		ft^2
A_{sp}	Cross-sectional area of spar		ft^2
ρ_{tb}	Density of torque box material		$slug/ft^3$
ρ_{sp}	Density of torque spar material		$slug/ft^3$
b_w	Wing span		ft
C_t	Weight correction for spar taper (equivalent stiffness)		
e_{tb}	Structural efficiency factor of torque box		
e_{sp}	Structural efficiency factor of spars		
S_{fair}	Area of fairings, leading and trailing edge		ft^2
U_{fair}	Unit weight of fairings, leading and trailing edge		lb/ft^2
S_{flap}	Area of control surfaces		ft^2
U_{flap}	Units weight of control surfaces		lb/ft^2
f_{fit}	Wing fittings and brackets (fraction maximum thrust of one rotor)		
T_{cap}	Maximum thrust capability of one rotor		lb
f_{fold}	Wing fold/tilt (fraction total weight excluding fold, including weight on tips)		

Intermediate calculations follow to support the primary weight calculations. The required quantities are A_{tb}, A_{sp}, and additional spar cap material to account for jump takeoff. The following formulae are for wing section form factors that relate typical airfoil and torque box geometry to ideal shapes for

beam bending, chord bending, torsion, and spar cap vertical/horizontal bending.

$$F_B = 0.073\,\sin(2\,\pi\,(\tau_w - 0.151)/0.1365) + 0.14598\,\tau_w + 0.610\,\sin(2\,\pi\,(w_{tb} + 0.080)/2.1560)$$

$$- (0.4126 - 1.6309\,\tau_w)\,(w_{tb} - 0.131) + 0.0081$$

$$F_C = 0.640424\,w_{tb}^2 - 0.89717\,w_{tb} + 0.4615\,\tau_w + 0.655317$$

$$F_T = ((0.27 - \tau_w)/0.12)\,0.12739\,\left(-0.96 + \sqrt{3.32 + 94.6788\,w_{tb} - (w_{tb}/0.08344)^2}\right)$$

$$- 2.7545\,w_{tb}^2 + 5.1799\,w_{tb} - 0.2683$$

$$F_{VH} = 0.25\,\sin(5.236\,w_{tb}) + 0.325$$

The area of the torque box is calculated by,

$$GJ = (\nu_T\,\Omega)^2\,\frac{1}{2}\,(b_w - w_{attach})\,\frac{1}{2}\,M_{tip}\,r_{pylon}^2$$

$$A_{tb} = 4\,GJ/(G_{tb}\,F_T\,t_w^2)$$

The area of the spar is calculated by adding the areas for chordwise and beamwise bending.

$$EI_C = (\nu_C\,\Omega)^2\,\frac{1}{24}\,b_w^3\,\frac{1}{2}\,M_{tip}\,f_{mode}$$

$$EI_{Ctb} = E_{tb}\,F_C\,A_{tb}\,c_{tb}^2/4$$

$$EI_{Csp} = EI_C - EI_{Ctb}$$

$$A_{Csp} = EI_{Csp}/(E_{sp}\,c_{tb}^2/4)$$

$$EI_B = (\nu_B\,\Omega)^2\,\frac{1}{24}\,b_w^3\,\frac{1}{2}\,M_{tip}\,f_{mode}$$

$$EI_{Btb} = E_{tb}\,F_B\,A_{tb}\,t_w^2/4$$

$$EI_{VH} = E_{sp}\,F_{VH}\,A_{Csp}\,t_w^2/4$$

$$EI_{Bsp} = EI_B - EI_{Btb} - EI_{VH}$$

$$A_{Bsp} = EI_{Bsp}/(E_{sp}\,t_w^2/4)$$

EI_{Csp} and EI_{Bsp} are replaced with zero if negative (no additional spar material required). If this is the case, the torque box and spar cap material assumed are sufficient to carry the load.

$$EI_{sp} = EI_{VH} + EI_{Bsp}$$

$$A_{sp} = A_{Csp} + A_{Bsp}$$

From here, the wing structural weight can be calculated from the primary weight calculations.

The ultimate applied bending moment is used to determine the necessity of additional spar cap material. If ΔM is negative, it is replaced with zero (no additional material needed). The additional

material is added to the spar area and the weight is recalculated.

$$M_U = T_{cap}\, l_w \left(0.75\left(1 - f_{tip}\right) - 0.375\left(l_w/b_w\right)\left(W_{TRWing}/W_{SD}\right)\right)$$

$$M_{tb} = 2\, EI_{Btb}\, \epsilon_U / t_w$$

$$M_{sp} = 2\, C_m\, EI_{sp}\, \epsilon_U / t_w$$

$$\Delta M = M_U - \left(M_{tb} + M_{sp}\right)$$

$$\Delta A_{sp} = 2\, \Delta M / \left(\epsilon_U\, E_{sp}\, t_w\right)$$

$$\Delta W_{spar} = C_j\, \Delta A_{sp}\, \rho_{sp}\, b_w / e_{sp}$$

Table 14: Tiltrotor/Tiltwing wing parameters - intermediate calculations

Parameter	Definition	Typical Value	Units
τ_w	Wing airfoil thickness-chord ratio (t/c)		
w_{tb}	Torque box chord to wing chord ratio		
ν_B	First normal bending natural frequency		per rev
ν_C	First chordwise bending natural frequency		per rev
ν_T	First torsion natural frequency		per rev
f_{mode}	Mode shape correction for fuselage motion	1-f_{tip}	
c_{tb}	Distance between two caps for ideal chord stiffness		ft
E_{tb}	Torque box modulus		lb/ft^2
E_{sp}	Spar modulus		lb/ft^2
Ω	Rotor speed for wing weight design condition		rad/s
b_w	Wing span (length of torque box)		ft
w_{attach}	Width of wing structural attachments to body		ft
r_{pylon}	Pylon radius of gyration		ft
G_{tb}	Torque box shear modulus		lb/ft^2
t_w	Radius of ideal tube for torsion stiffness		ft
l_w	Wing length (span less fuselage width)		ft
ϵ_U	Ultimate strain allowable (minimum of spar and torque box)		
C_m	Strength correction for spar taper (equivalent stiffness)		
C_j	Weight correction for spar taper (equivalent strength)		
n_{jump}	Load factor at W_{SD} (jump takeoff)		

Nacelle & Air Induction: This group includes engine support structure, engine cowling, and pylon support structure.

$$W_{supt} = \chi_{supt}\, 0.0412\, (1 - f_{airind})\, (W_{eng}/N_{eng})^{1.1433}\, N_{eng}^{1.3762}$$

$$W_{cowl} = \chi_{cowl}\, 0.2315\, S_{nac}^{1.3476}$$

$$W_{pylon} = \chi_{pylon}\, f_{pylon}\, W_{MTO}$$

$$W_{AirInd} = \chi_{airind}\, 0.0412\, f_{airind}\, (W_{eng}/N_{eng})^{1.1433}\, N_{eng}^{1.3762}$$

Table 15: Nacelle & air induction parameters

Parameter	Definition	Typical Value	Units
N_{eng}	Number of engines		
W_{MTO}	Maximum takeoff weight		lb
W_{eng}	Total engine weight		lb
S_{nac}	Total wetted area of nacelles and pylons (less spinners)		ft^2
f_{airind}	Air induction weight (fraction nacelle + air induction)	0.3 range 0.1 – 0.6	
f_{pylon}	Pylon support structure weight (fraction W_{MTO})		

Flight Controls: Flight controls are broken into three categories: fixed wing controls, rotary wing controls, and if a tiltrotor, conversion controls. Tiltwing is not included. First for a fixed wing, controls are separated into non-boosted and boost mechanisms.

$$w = 0.91000\, W_{MTO}^{0.6}$$

$$W_{FWnb} = \chi_{FWnb} * f_{FWnb} * w$$

$$W_{FWmb} = \chi_{FWmb}\, (1 - f_{FWnb}) * w$$

Rotary wing flight controls consist of non-boosted, boost mechanism, and boosted weights, all AFDD82 models.

$$W_{RWnb} = \chi_{RWnb}\, 2.1785\, f_{nbsv}\, W_{MTO}^{0.3999}\, N_{Rotor}^{1.3855}$$

$$w_{fc} = 0.2873\, f_{mbsv}\, (N_{Rotor}\, N_b)^{0.6257}\, c^{1.3286}\, (0.01\, V_{tip})^{2.1129}\, f_{RWred}^{0.8942}$$

$$W_{RWmb} = \chi_{RWmb}\, (1 - f_{RWhyd})\, w_{fc}$$

$$W_{RWb} = \chi_{RWb}\, 0.02324\, f_{bsv}\, (N_{Rotor}\, N_b)^{1.0042}\, N_{Rotor}^{0.1155}\, c^{2.2296}\, (0.01\, V_{tip})^{3.1877}$$

Conversion flight controls include non-boosted tilt controls and boost mechanisms.

$$W_{CVmb} = \chi_{CVmb}\, f_{CVmb}\, W_{MTO}$$

$$W_{CVnb} = \chi_{CVnb}\, f_{CVnb}\, W_{CVmb}$$

Table 16: Flight controls parameters

Parameter	Definition	Typical Value	Units
W_{MTO}	Maximum takeoff weight		lb
f_{FWnb}	Fixed wing non-boosted controls (fraction of total fixed wing flight control weight)		
N_{Rotor}	Number of rotors		
N_b	Number of blades		
c	Mean blade chord		ft
V_{tip}	Rotor tip speed in hover		ft/s
f_{RWhyd}	Rotary wing hydraulics (fraction hydraulics + boost mechanisms)	0.4	
f_{RWred}	Redundancy factor for flight control hydraulics	1 – 3	
f_{nbsv}		1.8984 ballistically survivable 1.0 otherwise	
f_{mbsv}		1.3029 ballistically survivable 1.0 otherwise	
f_{bsv}		1.1171 ballistically survivable 1.0 otherwise	
f_{CVmb}	Conversion boost mechanisms (fraction W_{MTO})		
f_{CVnb}	Conversion non-boosted (fraction boost mechanisms weight)		

Hydraulics: This group includes weight of hydraulics for fixed wing flight controls, rotary wing flight controls, rotor tilting conversion controls, and associated equipment.

$$W_{FWhyd} = \chi_{FWhyd}\, f_{FWhyd}\, W_{FWmb}$$

$$W_{RWhyd} = \chi_{RWhyd}\, f_{RWhyd}\, w_{fc}$$

$$W_{CVhyd} = \chi_{CVhyd}\, f_{CVhyd}\, W_{CVmb}$$

Table 17: Hydraulics parameters

Parameter	Definition	Typical Value	Units
f_{FWhyd}	Fixed wing hydraulics weight (fraction boost mechanisms weight)		
f_{RWhyd}	Rotary wing hydraulics weight (fraction hydraulics + boost mechanisms weight)		
f_{CVhyd}	Conversion hydraulics weight (fraction boost mechanisms weight)		

Anti-Icing: The total weight of the anti-icing group is obtained from summing over all rotors, wings, and engines.

$$W_{DIelect} = \chi_{DIelect}\, \Sigma k_{elect}\, A_{blade}$$

$$W_{DIsys} = \chi_{DIsys}\, \left(\Sigma k_{rotor}\, A_{blade} + \Sigma k_{wing}\, l_{wing} + k_{air} \Sigma W_{eng}\right)$$

Table 18: Anti-icing parameters

Parameter	Definition	Typical Value	Units
A_{blade}	Rotor blade area		ft^2
l_{wing}	Wing length		ft
W_{eng}	Weight of all engines		lb
k_{rotor}	Rotor deice system weight factor		
k_{wing}	Wing deice system weight factor		
k_{elect}	Electrical system weight factor		
k_{air}	Engine air intake deice weight factor		

Fuel System: The fuel system weight consists of tanks, plumbing, and support structure.

$$W_{tank} = \chi_{tank}\, 0.4341\, C_{int}^{0.7717}\, N_{int}^{0.5897}\, f_{cw}\, f_{bt}^{1.9491}$$

$$W_{plumb} = \chi_{plumb}\, \left[K_{0plumb} + K_{1plumb}\, (0.01\, N_{plumb} + 0.06\, N_{eng})\, (F/N_{eng})^{0.866}\right]$$

Table 19: Fuel system parameters

Parameter	Definition	Typical Value	Units
N_{int}	Number of internal fuel tanks		
C_{int}	Internal fuel tank capacity		gallons
f_{bt}	Ballistic tolerance factor	1 – 2.5	
f_{cw}	Crashworthiness factor	1.3131 ballistically survivable 1.0 otherwise	
N_{plumb}	Total number of fuel tanks for plumbing (internal and auxilliary)		
N_{eng}	Number of engines		
K_{0plumb}	Plumbing weight constant	50 – 250	lb
K_{1plumb}	Plumbing weight constant crashworthiness/survivability factor	2	
F	Fuel flow rate		lb/hr

Bibliography

[1] F.H. Dean. *Curtiss X-Planes: Curtiss-Wright's VTOL Effort 1958-1965*. Schiffer Military History Book Series, Schiffer Publishing, Atglen, PA, 2001.

[2] J. M. Schuler, R. E. Smith, and J. V. Lebacqz. An experimental investigation of stol longitudinal flying qualities in the landing approach using the variable stability x-22a aircraft. In *Proceedings of 28th Annual National Forum of the American Helicopter Society*, Washington, D.C., May 17-19,1972.

[3] L. Joseph III and W. Hesse. Survey of significant technical problems unique to vstol encountered in the development of the xc-142a. *Journal of Aircraft*, 3(1):3–10, January 1966.

[4] Tiltrotor Project Office Staff coordinated by Martin Maisel. Tiltrotor research aircraft familiarization document. Technical report, NASA-TM–X-62407, 1975.

[5] I. Chopra. Small uas and delivery drones: Challenges and opportunities: The 38th alexander a. nikolsky honorary lecture. In *Vertical Flight Society 78th Annual Forum Technology Display*, Fort Worth, TX, May 10-12, 2022.

[6] E. Fisler. *Comprehensive Study and Fundamental Understanding of Lithium Sulfer Batteries for eVTOL*. PhD thesis, University of Maryland, 2022.

[7] E. Fisler and A Datta. Fabrication, testing, and comparative analysis of lithium sulfur and lithium-ion electrochemistries. In *Vertical Flight Society 78th Annual Forum Technology Display*, Fort Worth, TX, May 10-12, 2022.

[8] I. Husain. *Electric and Hybrid Vehicles: Design Fundamentals*. CRC Press, Taylor & Francis Group, 3 edition, 2021.

[9] C Mi and M. A. Masrur. *Hybrid Electric Vehicles: Principles and Applications with Practical Perspectives*. Wiley & Sons Ltd, 2 edition, 2018.

[10] D. Kim, T. Perry, and P. Ansell. A review of distributed electric propulsion concepts forair vehicle technology. In *AIAA/IEEE Electric Aircraft Symposium*, Cincinatti, OH, Jul 9-11, 2018.

[11] C. Friedrich and P. Robertson. Hybrid-electric propulsion for aircraft. *Journal of Aircraft*, 52(1):176–189, January 2015.

[12] D. Dehesa, S. Menon, S. Brown, and C. Hagen. Dynamic analysis of a series hybrid-electric powertrain for an unmanned aerial vehicle. *Journal of Propulsion and Power*, 38(1):84–96, January 2022.

[13] A. Sridharan, B. Govindarajan, and I. Chopra. A scalability study of the multirotor biplane tailsitter using conceptual sizing. *Journal of the American Helicopter Society*, 65(1):1–18, January 2020.

[14] B. Mills and A. Datta. Fundamental studies of variable-voltage hybrid-electric powertrains. *Journal of the American Helicopter Society*, 66(2):1–14, April 2021.

[15] M. Ricci, V. Varahamurthy, and R. Hicks. Power system characterization and flight testing of a $>$ 55 lb hybrid-electric multirotor. In *Vertical Flight Society Annual Forum 78*, Ft. Worth, TX, USA, May 10-12, 2022.

[16] W. Johnson. A history of rotorcraft comprehensive analyses. Technical report, NASA/TP-2012-216012, 2012.

[17] W. Johnson and A. Datta. Requirements for next generation comprehensive analysis of rotorcraft. In *AHS Specialist's Conference on Aeromechanics*, San Francisco, CA, Jan 23-25, 2008.

[18] W. Johnson and C. Silva. Nasa concept vehicles and the engineering of advanced air mobility aircraft. *The Aeronautical Journal*, 126:59–91, January 2022.

[19] D. Jayasundara and J. Baeder. Aerodynamic and aeroacoustic analysis of a quadrotor biplane tailsitter. *Journal of the American Helicopter Society*, 71(1):1–18, January 2026.

[20] D. Jayasundara, Y. Jung, and J. Baeder. Aeroacoustic and aerodynamic investigation of a wingtip-mounted tractor propeller. *Journal of the American Helicopter Society*, 68(1):1–16, January 2023.

[21] D. Jayasundara, P. Arias, and J. Baeder. Multi-fidelity investigation of noise control mechanisms for a quadrotor biplane tailsitter in forward flight. In *AIAA SCITECH FORUM*, Orlando, FL, Jan 8-12, 2024.

[22] S. Sadeghi and Parsa L. Multiobjective design optimization of five-phase halbach array permanent-magnet machine. *IEEE Transactions on Magnetics*, 47(6):1658–1666, January 2011.

[23] P. S. Kumar, B. Venkatesh, B. Rajeswari, V. L. Reddy, and S. P. Khan. Emission control by using water emulsified diesel in single cylinder diesel engine. *International Journal of Advances in Engineering Technology*, 5(2):263–273, Jan 2013.

[24] P. Hatte and Y. Bhalerao. Influence of ethanol-gasoline fuel fractions on variable compression ratio engine. *International Journal of Recent Technology and Engineering*, 8(3):2929–2936, September 2019.

[25] H. Cho Goering. Engine model for mapping bsfc contours. *Mathematical and Computer Modelling*, 11:514–518, 1988.

[26] B. Mills. *Fabrication and Fundamental Studies of a 4-kW, Variable-Voltage, Distributed Hybrid-Electric Powertrain for eVTOL Aircraft*. PhD thesis, University of Maryland, 2022.

[27] B. Mills and A. Datta. Simulation and characterization of variable-voltage hybrid-electric powertrains. In *Vertical Flight Society Annual Forum 76*, October 6-8, 2020.

[28] Lionel S. Marks, G. A. Goodenough, John B. Baker, E. A. Allcut, L. C. Lichty, C. N. Cross, G. B. Upton, P. H. Schweitzer, Edgar J. Kates, F. O. Ellenwood, and F. C. Evans. Discussion: Efficiencies of otto and diesel engines. *Transactions of the American Society of Mechanical Engineers*, 49-50(9):095505, December 2023.

[29] Wayne Johnson, Hyeonsoo Yeo, and Cecil Acree. Performance of advanced heavy-lift, high-speed rotorcraft configurations. In *AHS International Forum*, Seoul, Korea, Oct 15-17, 2007.

[30] W. Johnson, E. Solis, and C. Silva. Concept vehicles for vtol air taxi operations. In *TVF*, San Francisco, CA, Jan 16-19, 2018.

[31] S. Gul. *A Modern Aeromechanical Analysis of Hingeless Hub Tiltrotors With Model- And Full-Scale Wind Tunnel Validation*. PhD thesis, University of Maryland, 2022.

[32] A. Shastry and A. Datta. Predicting wake and structural loads in rpm controlled multirotor aircraft. In *Vertical Flight Society's Transformative Vertical Flight Technical Meeting*, San Jose, CA, Jan 21-23, 2020.

[33] J. P. Magee and H. R. Alexander. Wind tunnel tests of a full scale hingeless prop/rotor designed for the boeing model 222 tilt rotor aircraft. Technical report, NASA-CR–114664, Boeing Vertol Company, 1973.

[34] F. Tsai, J. Sutherland, A. Akinwale, A. Morin, S. Gul, and A. Datta. Development and whirl flutter test of the maryland tiltrotor rig. *Journal of the American Helicopter Society*, 69(1):1–45, January 2024.

[35] G. Srinivasan and J. Baeder. TURNS: A free-wake euler/navier-stokes numerical method forhelicopter rotors. *AIAA Journal*, 31(5):801–976, May 1993.

[36] M. Ramasamy, N. Gold, and M. Baghwat. Rotor hover performance and flowfield measurements with untwisted and highly-twisted blades. In *36th European Rotorcraft Forum*, Paris, France, Sep 7-9, 2010.

[37] W. Johnson. NDARC NASA design and analysis of rotorcraft. Technical report, NASA/TP–2009-215402, 2014.

[38] W. Johnson. NDARC - NASA design and analysis of rotorcraft validation and demonstration. In *AHS Aeromechanics Specialists' Conference*, San Francisco, CA, Jan 20-22, 2010.

[39] W. Ogle. Electromagnetic noise mitigation on an electric tiltrotor rig and hover performance testing. Master's thesis, University of Maryland, 2025.